



저작자표시-비영리-변경금지 2.0 대한민국

이용자는 아래의 조건을 따르는 경우에 한하여 자유롭게

- 이 저작물을 복제, 배포, 전송, 전시, 공연 및 방송할 수 있습니다.

다음과 같은 조건을 따라야 합니다:



저작자표시. 귀하는 원저작자를 표시하여야 합니다.



비영리. 귀하는 이 저작물을 영리 목적으로 이용할 수 없습니다.



변경금지. 귀하는 이 저작물을 개작, 변형 또는 가공할 수 없습니다.

- 귀하는, 이 저작물의 재이용이나 배포의 경우, 이 저작물에 적용된 이용허락조건을 명확하게 나타내어야 합니다.
- 저작권자로부터 별도의 허가를 받으면 이러한 조건들은 적용되지 않습니다.

저작권법에 따른 이용자의 권리는 위의 내용에 의하여 영향을 받지 않습니다.

이것은 [이용허락규약\(Legal Code\)](#)을 이해하기 쉽게 요약한 것입니다.

[Disclaimer](#)

공학박사학위논문

**Long-time Dynamic Simulation of  
Industrial-scale Multiphase  
Chemical Reactor Using  
Computational Fluid Dynamics**

전산유체역학을 이용한  
산업용 다상 화학 반응기  
장시간 모사

2020 년 8 월

서울대학교 대학원

화학생물공학부

김 민 준

## Abstract

# Long-time Dynamic Simulation of Industrial-scale Multiphase Chemical Reactor Using Computational Fluid Dynamics

Minjun Kim

School of Chemical & Biological Engineering  
The Graduate School of Seoul National University

Computational fluid dynamics (CFD) is widely used to conduct research on multiphase reactors with complex flows. However, because of the very large amount of computation load, most of the research is limited to simulating laboratory-scale reactors just for seconds. Therefore, this research develops methodologies for simulating industrial-scale multiphase reactors for a long time to overcome the limitations of CFD.

First, a methodology is developed to simulate industrial-scale multiphase reactors by combining CFD with widely used correlation. In the gas-liquid reactor, if population balance equation is introduced

into CFD to simulate the physical phenomena of bubble coalescence or breakage, long computational time and unclearness of kernel constants make it difficult to simulate the reactor. Therefore, the physical phenomena are considered with a small amount of computational load by combining CFD with widely used correlation equations. Finally, through a comparison between CFD models and experimental results, the CFD model is validated.

Second, a methodology is developed to simulate industrial-scale multiphase reactors more than an hour. The CFD-based compartmental model is used for a long-time dynamic simulation; the CFD-based compartmental model calculates flow information in millions of mesh and using this information chemical reactions or physical phenomena are calculated in hundreds of zones for more than 10 hours. At the conclusion, long-time dynamic simulations are compared with the experimental results, errors below 7 % shows the validity of the model.

Finally, a two-way coupled CFD-DQMOM approach is developed to overcome the limitations of the CFD-based compartment model. The CFD-based compartment model that performs long-time simulation using only the initial flow information obtained from CFD

cannot be used when the flow changes significantly due to chemical reactions or various physical phenomena. Therefore, to overcome the limitations of the CFD-based compartment model, the two-way coupled CFD-DQMOM approach that periodically updates the flow information is developed and applied to a fluidized bed reactor whose flow changes over time. With this approach, it is confirmed that the approach can obtain changes of particle size distribution over a long period of time that could not be achieved using only CFD.

**Keywords:** Industrial-scale reactor; CFD; Long-time simulation; Population balance equation; CFD-based compartmental model; Two-way coupled CFD-DQMOM approach

**Student Number:** 2015-21044

# Contents

Abstract .....	ii
Contents .....	v
List of Figures .....	9
List of Tables.....	15
CHAPTER 1. Introduction.....	16
1.1    Motivation .....	16
1.2    Target systems .....	21
1.3    Objectives .....	23
1.4    Outline of the thesis .....	24
CHAPTER 2. CFD simulation of a pilot-scale mineral carbonation reactor using CFD-lumped correlation model .....	26
2.1    Objective.....	26
2.2    Experimental setup.....	27
2.3    Model description .....	34
2.3.1    Numerical setup .....	34
2.3.2    Governing equations.....	42

2.4	Results and discussion.....	51
2.4.1	CFD model feasibility test .....	51
2.4.2	Hydrodynamic analysis in the CFD model.....	62
2.4.3	CFD model verification by comparing with actual pilot-plant .....	68
CHAPTER 3. Long-time CFD simulation of industrial-scale reactors using CFD-based compartmental model.....		
3.1	Objective.....	73
3.2	Experimental setup.....	74
3.3	Model description .....	79
3.3.1	Governing equations.....	79
3.3.2	Numerical setup .....	90
3.3.3	Zoning method .....	95
3.4	Results and discussion.....	97
3.4.1	Compartmental model for pilot-scale reactor (limitation of compartmental model) .....	97
3.4.2	CFD-based compartmental model for the pilot-scale reactor. ....	101

3.4.3	CFD-based compartmental model for the industrial-scale reactor. ....	110
3.4.4	CFD-based compartmental model for 2.5 and 10 times larger than the industrial-scale reactor.....	122
CHAPTER 4. Long-time dynamic simulation of fluidized bed reactor using two-way coupled CFD-DQMOM approach.....		
4.1	Objective.....	129
4.2	Modeling of gas-solid flows in fluidized bed reactor .....	129
4.2.1	Flow model .....	130
4.2.2	PBM.....	132
4.3	Reactor geometry and conditions.....	139
4.4	Methodology of the two-way coupled CFD-DQMOM.....	142
4.4.1	Extraction of flow information from CFD.....	142
4.4.2	Two-way coupled CFD-DQMOM simulation.....	144
4.5	Simulation setup.....	148
4.5.1	Two-way coupled CFD-DQMOM setup.....	150
4.5.2	CFD-QMOM simulation setup .....	151
4.6	Results and discussion.....	155

4.6.1	Two-way coupled CFD-DQMOM results .....	155
4.6.2	CFD-QMOM results.....	163
4.6.3	Two-way coupled CFD-DQMOM simulation for 6h..	167
CHAPTER 5. Concluding Remarks .....		170
5.1	Conclusion .....	170
5.2	Future work.....	172
5.2.1	Turbulence effect caused by physicochemical phenomena. ....	172
5.2.2	Number of bins that can be flexibly changed in DQMOM .....	173
5.2.3	Integration of kinetics and PBM .....	173
Bibliography.....		175
Nomenclature .....		182
Abstract in Korean (국문초록).....		186
APPENDIX:CFD-based compartmental model code.....		189

## List of Figures

Figure 2-1. Side views of Gas distributor and nozzle structures of type A & B.....	29
Figure 2-2. Side and top view of the reactor.....	30
Figure 2-3. Process flow diagram of the pilot-scale aqueous mineral carbonation process. ....	31
Figure 2-4. Gas holdup & amount of mass-transferred CO <sub>2</sub> (t/day) in 1 <sup>st</sup> reactor for 15 s. ....	39
Figure 2-5. Gas holdup in rotating and non-rotating conditions. ..	46
Figure 2-6. Gas distributor structure of Cases I & II.....	53
Figure 2-7. Gas holdup profiles in the three cases. ....	54
Figure 2-8. Gas holdup from the CFD model and Eqs. 2-32 & 2-33.....	55
Figure 2-9. Gas holdup profiles of the CFD model based on operating time of 0 - 15 s.....	64
Figure 2-10. CO <sub>2</sub> holdup profiles of the CFD model based on operating time of 0 - 15 s.....	65

Figure 2-11. Mass transfer rate profile of the CFD model at 15 s.	66
Figure 2-12. Bubble diameter profiles of the CFD model based on operating time of 0 - 15 s.	67
Figure 2-13. Comparison of the CO <sub>2</sub> removal efficiencies between the CFD model and the experiments.	70
Figure 2-14. Gas holdup profiles of the CFD model for Experiment III 1 <sup>st</sup> reactor based on an operating time of 0-15 s.	71
Figure 3-1. Side view and top view of the industrial-scale reactor and configuration of nozzle.	76
Figure 3-2. Systematic diagram for the CFD-based compartmental model.	85
Figure 3-3. Mesh test in pilot-scale (left) and industrial-scale (right) reactors.	92
Figure 3-4. CO <sub>2</sub> holdup profiles obtained from the CFD-hydrodynamics model (left), and side and top view (middle and right) of the divided pilot-scale reactor configuration.	96
Figure 3-5. CO <sub>2</sub> holdup profile of the CFD-based compartmental	

model in 20-zone model in Experiment P-1 of 1st reactor..	100
Figure 3-6. Side and top views of the 20-, 60-, 163-, and 324-zone models in the pilot-scale reactor. ....	102
Figure 3-7. Sum of CO <sub>2</sub> removal rate along the height in 20-, 60-, 163-, and 324-zone models in Experiment P-1 of 1st reactor. ....	105
Figure 3-8. CO <sub>2</sub> holdup profiles of the CFD-based compartmental model in 60-zone (left), 163-zone (middle), and 324-zone (right) models in Experiment P-1 of 1st reactor. ....	106
Figure 3-9. CO <sub>2</sub> holdup profiles of the CFD-based compartmental model with 324-zone (left) and CFD-absorption model (right) models in Experiment P-1 of 1st reactor. ....	107
Figure 3-10. CO <sub>2</sub> holdup profiles of the CFD-based compartmental model and CFD-absorption model in Experiments P-1 and P-2.....	108
Figure 3-11. Comparisons of the CO <sub>2</sub> removal efficiencies derived from experiments, CFD-based compartmental model, and CFD-absorption model in the pilot-scale process. ....	109

Figure 3-12. CO <sub>2</sub> holdup profiles of the CFD-based compartmental model in 119-zone (left), 179-zone (middle), and 291-zone (right) models in Experiment I-2 2nd reactor.....	111
Figure 3-13. Robustness test of zone numbers by comparison of model results with operation data in Experiment I-1.....	112
Figure 3-14. Side and top views of the 179-zone model in the industrial-scale reactor. ....	113
Figure 3-15. Model results compared with operation data from (a) Experiment I-1 and (b) Experiment I-2.....	115
Figure 3-16. Concentration changes of involved species during Experiment I-1.....	120
Figure 3-17. CO <sub>2</sub> holdup changes at each zone during the operation.....	121
Figure 3-18. Side and top views of Type A (gas inlet 17,500 Nm <sup>3</sup> /hr) and Type B (gas inlet 70,000 Nm <sup>3</sup> /hr) reactors. ...	125
Figure 3-19. Side and top views of the 181 compartments for Type A reactor. ....	126
Figure 3-20. Side and top views of the 164 compartments for	

Type B reactor. ....	127
Figure 3-21. Predicted dynamic behaviors of Type A and Type B reactors. ....	128
Figure 4-1. Configuration of FBR. ....	141
Figure 4-2. Zone configuration and particle volume fraction $(\alpha_{sp}^{(ij)})$ . ....	143
Figure 4-3. Systematic diagram for the two-way coupled CFD-DQMOM simulation. ....	146
Figure 4-4. $d_{32}$ (Sauter mean diameter) along height for the flows updating interval of 10, 15, and 60 s models. ....	147
Figure 4-5. $d_{32}$ along height for the number of nodes of 170,000 and 570,000 models. ....	149
Figure 4-6. $d_{32}$ along height for the 84, 228, and 348-zone models .....	153
Figure 4-7. Side view of 84, 228, and 348-zone model. ....	154
Figure 4-8. Particle volume fraction profiles for 60 s in the two-way coupled CFD-DQMOM model. ....	158

Figure 4-9. In initial and final-state, particle volume fraction profiles for each particle..... 159

Figure 4-10.  $d_{32}$  along height for  $s_1$ ,  $s_2$ , and  $s_3$  particles..... 160

Figure 4-11. Particle size distribution from 1st to 50th floor in initial and final-state..... 162

Figure 4-12. Particle volume fraction profiles of each particle for the two-way coupled CFD-DQMOM model (left) and CFD-QMOM model (right)..... 166

Figure 4-13. Particle volume fraction profiles for 6 h in the two-way coupled CFD-DQMOM model. .... 168

Figure 4-14. Particle size distribution from 1st to 50th floor in initial and final-state for 6 h simulation. .... 169

## List of Tables

Table 2-1. Three experiments conditions.....	33
Table 2-2. Mesh test results for gas holdup, interfacial area, and amount of mass transfer rate in Experiment II 1st reactor at 15 s. ....	35
Table 2-3. Interfacial area obtained from Eq. 2-34 and the CFD model.....	58
Table 2-4. Mass transfer coefficient from the CFD model and published data. ....	61
Table 3-1. Experimental conditions for the pilot-scale process ....	77
Table 3-2. Experimental conditions for industrial-scale process. .	78
Table 4-1. Final result of each particle mean diameter and ratio for the CFD-hydrodynamic, two-way coupled CFD-DQMOM, and CFD-QMOM models.....	165

## CHAPTER 1. Introduction

### 1.1 Motivation

Various multiphase reactors are used in chemical processes such as slurry reactor, fluidized bed reactor (FBR), and bubble column. However, due to the complex flow pattern of multiphase reactors, it is difficult to design the reactors characterizing flow pattern and mixing and to find the cause when troubles occur in process. Recently, as the computation power increases, computational fluid dynamics (CFD) has made a great progress and has been used to chemical processes. Strasser and Wonders [1] employed the CFD to investigate an industrial-scale slurry bubble column reactor. Using CFD, Park et al. [2] designed and optimized a carbonation reactor for solid suspension and Zimmermann and Taghipour [3] applied the CFD simulation for the FBR. Furthermore, Park et al. [4] integrated multi-objective Bayesian optimization with the CFD to optimize reactor structure and condition automatically.

### *CFD Simulation of multiphase reactor with PBM and its limitations*

The population balance model (PBM) has been widely used to account for particle interactions [5-8]. Among the methods to solve the PBM, the discretization population balance approach and classes methods are direct methods that discretize the internal coordinate, e.g., the particle length, into a finite series of bins. An acceptable accuracy can be obtained if a large number of bins are used. However, a tradeoff exists between the number of bins and the computational cost, and the methods become impractical for multiphase reactors owing to the excessive number of required bins [9]. As alternative methods to efficiently solve the PBM, the quadrature method of moments (QMOM) and a direct quadrature method of moments (DQMOM) have garnered attention because they both require only a few abscissas to compute particle size distributions [10, 11]. Recently, much effort has been expended into analyzing multiphase reactor through the integration of CFD and QMOM/DQMOM [8, 12, 13].

Yang and Xiao [14] and Bordel et al. [15] used CFD and PBM to study complex bubble size distributions in bubble columns with a diameter smaller than 15 cm. However, due to the large computational power required for the PBM, studies on large-scale reactors have

rarely been published [16-19]. For this reason, methodologies to simulate large-scale multiphase reactors with low computational cost has been required.

### ***Long-time CFD simulation***

In batch-reactor, several variables such as temperature, concentration, viscosity and pressure show dynamic changes for a long-time. However, studies on the long-time dynamic simulation have rarely been published. This is because the CFD simulation requires too much computational power to simulate the industrial-scale multiphase reactor longer than an hour.

### ***Economical CFD simulation through the CFD-based compartmental model***

Owing to the limitation of the CFD model that it requires enormous computational power, a compartmental model or network-of-zones model, which is a traditional method to predict hydrodynamics, has been studied as an alternative to CFD [20]. The compartmental models divide the reactor into dozens to hundreds of small zones, or compartments, until each zone can be approximated to have a homogeneous condition as in a continuous stirred-tank reactor [21].

Mass flow rates between the zones are estimated based on the rotational speed of the impeller, and the conditions of the zones over time are calculated from mass balance equations. Thus, the compartmental models are able to simulate the reactor dynamics with cheap computational cost considering both hydrodynamics and reactions. Vrabel et al. [22, 23] and Zahradnik et al. [24] employed the compartmental model for the analysis of large-scale gas–liquid fermentation reactors and bioreactor, respectively. However, the compartmental model, particularly for multiphase reactors, still has a limitation in that only the general tendencies, not detailed results, about the system are reliable [25]. For example, in gas-liquid stirred tank reactor, unlike the liquid flow rate between the zones, which can be well predicted from the impeller speed, the gas flow rate is complicated to estimate because it is affected by not only impeller rotational force but also buoyance force and a complex gas sparger configuration. If a reactor is a bubble column, even the liquid flow rate cannot be accurately predicted. In addition, there is no method or correlation to predict hydrodynamics information in the FBR such as impeller speed in stirred tank reactor.

To overcome this difficulty of predicting hydrodynamic information in compartmental models, attempts have been made to combine CFD and compartmental models. This combined model is referred to as the CFD-based compartmental model [26, 27]. In this combined model, instead of estimating the mass flow rates between the zones based on simple correlations, they are calculated from the CFD model, which converges in a few seconds of physical time, without considering any chemical reaction. The next steps to simulate chemical reactions are same as in the compartmental model. Because the hydrodynamic information that must be calculated in millions of meshes converges in a few seconds and the reaction can be calculated in hundreds of zones, not in millions of zones, in the CFD-based compartmental model, the economical CFD simulation can be carried out using this model. Bezzo et al. [28] first used this model for modeling a bioreactor. Subsequently, other applications of the model followed; such as in the ozone process and  $\text{CO}_2$  and  $\text{Ca}(\text{OH})_2$  precipitation reactor [29, 30]. However, the CFD-based compartmental model has rarely been used to simulate a reactor for a long-time and only has been used to reduce computational time by calculating CFD-PBM-kinetics separately in each numerical tool.

## *Limitation and improvement of the CFD-based compartmental model*

The CFD-based compartmental model has not been applied to the reactor with dynamic internal flow change such as the FBR. It is difficult to use this model in the FBR owing to challenges arising from changes in the flow due to particle aggregation and breakage. Moreover, it is inappropriate to use initial flows from CFD in PBM calculation for long-time behaviors because the phenomena render the particles larger or smaller and the varying particle sizes change the flow. To use the CFD-based compartmental model in the FBR, it is essential to update the flow information periodically in a computationally amenable fashion.

In conclusion, there are still many limitations to using CFD for simulating multiphase reactor. Therefore, a development of new CFD methodology to scale-up and to simulate for a long-time has been required.

## **1.2 Target systems**

### *Mineral carbonation reactor*

As global warming has become a worldwide issue, carbon capture,

utilization, and storage (CCUS) technologies are attracting increasing attention because these methods can remove CO<sub>2</sub>, the major contributor to global warming. Among the CCUS technologies, mineral carbonation is commercially available and cost-effective owing to a direct reaction of CO<sub>2</sub> in the flue gas with the Ca(OH)<sub>2</sub> solution from the waste mineral system and without the need for complex separation units [31-34]. For the successful establishment of the technology, pilot- and industrial-scale mineral carbonation plants were built in Incheon, South Korea. These plants have a series of two identical reactors; one 2.2 m in diameter and 6.0 m in height and the other 4.0 m in diameter and 4.0 m in height [2, 35].

### ***Fluidized bed reactor***

An FBR is widely used to produce polyolefins owing to their superior transfer characteristics and simple configuration [11, 36, 37]. In the FBR, a particle is suspended and behaves as though it is a fluid by a high-velocity fluid passing through. Despite several advantages of the FBR, complex flows between a particle and fluid render their operation difficult. Consequently, analyzing the internal flow dynamics of the FBR is a main issue, and a computationally feasible solution is still being sought [11, 37, 38].

### 1.3 Objectives

The objective of this thesis is to propose new CFD simulation methodology for long-time dynamic simulation of industrial-scale multiphase reactor.

First, the methodology of steady-state simulation for large-scale multiphase reactor is proposed. In multiphase reactor, particle interactions such as particle breakage and coalescence must be considered. The PBM is the most widely used but an enormous computation power required to calculate PBM makes it impossible to simulate large-scale reactor. As a results, a CFD-lumped correlation model is introduced to reduce the computational cost. In this model, the particle interactions are considered by lumped correlation, which was derived from the one-dimensional bubble number density and interfacial area transport equations. Using the model, large-scale multiphase reactor simulation can be implemented with economical computational cost. Next, the author put forward methodology for long-time dynamic simulation of large-scale multiphase reactor. The CFD-based compartmental model is applied to simulate a target

industrial-scale mineral carbonation reactor. For the simulation, first, the CFD simulation of the reactor is carried out to deriving the hydrodynamic information during a short-time. After that, using the information, the kinetics are calculated in hundreds of zones for a long-time, 8 h. Through the simulation, dynamic changes of several variables such as temperature and concentrations can be obtained over time. Finally, two-way coupled CFD-DQMOM approach is proposed. In this approach, the hydrodynamic information is updated periodically to reflect flow change by several physical phenomena or chemical reactions. Because the CFD-based compartmental model cannot reflect flow change over time, it is inappropriate to use the model to the FBR or bioreactor which have dynamic flow change by chemical reactions or physical phenomena. As a result, the approach is applied to the FBR and the 6 h dynamic simulation results are derived

#### **1.4 Outline of the thesis**

In CHAPTER 2, modeling and validation of a pilot-scale mineral carbonation reactor is carried out using CFD. The CFD-lumped correlation model is used to solve the problem efficiently and the results are compared to the real-plant data for the model validation. In

CHAPTER 3, modeling of pilot- and industrial-scale mineral carbonation reactors is performed using CFD. To simulate dynamic variables data over long-time, the CFD-based compartmental model is used. Validation of the model is performed and after that, the model is applied to larger reactors. CHAPTER 4 presents the two-way coupled CFD-DQMOM approach to make up for the limitation of the CFD-based compartmental model. This approach is used to simulate the FBR. Finally, in CHAPTER 5, the conclusion and the suggestion for the future works are given.

## **CHAPTER 2. CFD simulation of a pilot-scale mineral carbonation reactor using CFD-lumped correlation model<sup>#</sup>**

### **2.1 Objective**

In this chapter, CFD modelling for the pilot-scale mineral carbonation reactor is conducted. To reduce a computational cost, CFD-lumped correlation model is employed. Where bubble breakage and coalescence are considered by lumped correlation, Hibiki and Ishii [39] correlation, which is derived from one-dimensional bubble number density and interfacial area transport equations, and hydrodynamics and interphase mass transfer are considered by CFD. To determine the suitability of the CFD-lumped correlation model, a two-step verification proceeds. First, for gas holdup, interfacial area,

---

<sup>#</sup> This chapter cites the author's published journal article: M. Kim, J. Na, S. Park, J.-H. Park, and C. Han, "Modeling and validation of a pilot-scale aqueous mineral carbonation reactor for carbon capture using computational fluid dynamics," *Chemical Engineering Science*, vol. 177, pp. 301-312, 2018 [35].

and mass transfer coefficient, validations are carried out since these are important parameters for representing hydrodynamics of a reactor. By comparing the CFD results with experimental data and widely used empirical correlation in literatures, the model qualification is performed. Second, using the verified hydrodynamics parameters, the CO<sub>2</sub> removal efficiency is derived with the CFD model and a comparison of the CO<sub>2</sub> removal efficiency from the CFD model and from the pilot-plant data shows the validity of the CFD model.

## **2.2 Experimental setup**

The pilot-scale reactor has a diameter of 2.2 m and a height of 6 m. The high performance gas distributor has totally nine nozzles. Two types of nozzles can be seen in Figure 2-1. Upper part three nozzles are type A and lower part six nozzle are type B. Although type A nozzle is more longer than type B, it is operated similar to type B since only lower part of nozzle, 420 mm, has holes which blow out gas. The nozzles have a lot of hole whose diameter is 5 mm. Tiny impeller with a diameter of 15 cm is installed to prevent the sedimentation of solid at a height of 1.2 m on the side wall, and operated at a speed of 150 rpm. The reactor and gas distributor are shown in Figure 2-2. The pilot-plant consists of a series of two reactors with exactly same

geometry. In the process, flue gas with a volumetric flow rate of 3 500 Nm<sup>3</sup>/h containing 8 - 10 vol.% of CO<sub>2</sub>, flows into first reactor containing a Ca(OH)<sub>2</sub> mixed solution and the effluent gas enters the second reactor to capture the remaining CO<sub>2</sub> after pressurization. Meanwhile, Ca(OH)<sub>2</sub> mixed solution composed of Ca(OH)<sub>2</sub>, NaOH, and water, counter-currently flows into second reactor, and remaining Ca(OH)<sub>2</sub> enters to first reactor after the Ca(OH)<sub>2</sub> and CaCO<sub>3</sub> mixture is separated into Ca(OH)<sub>2</sub> and CaCO<sub>3</sub> (See Figure 2-3).

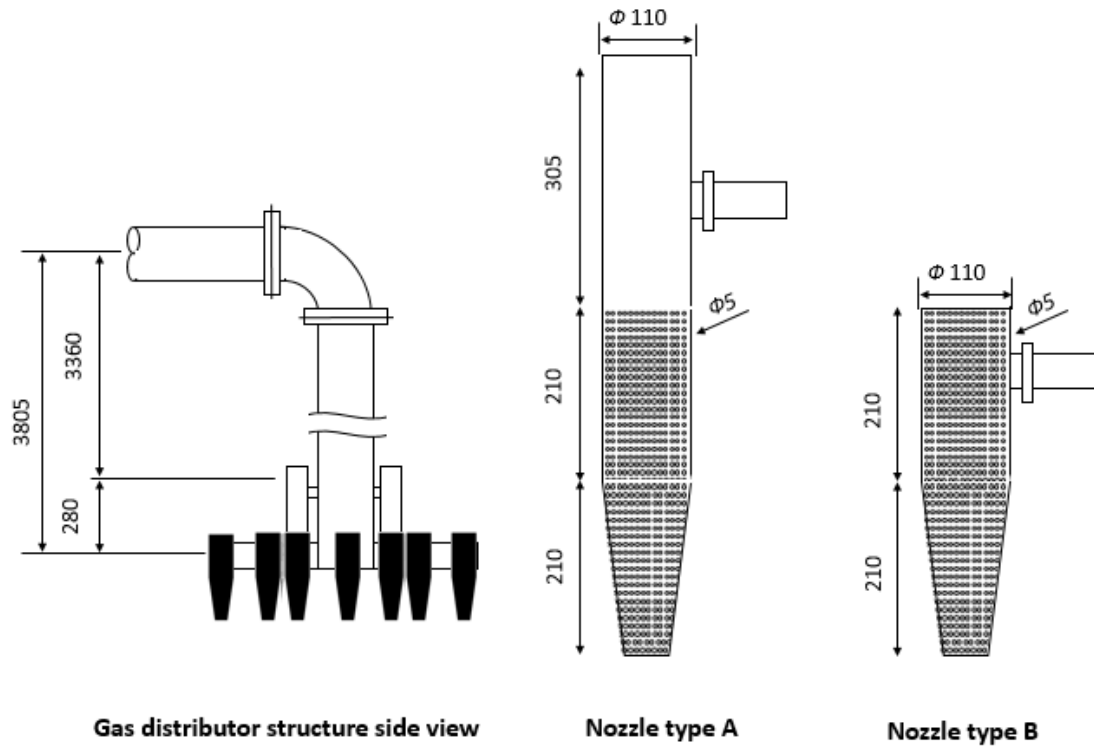
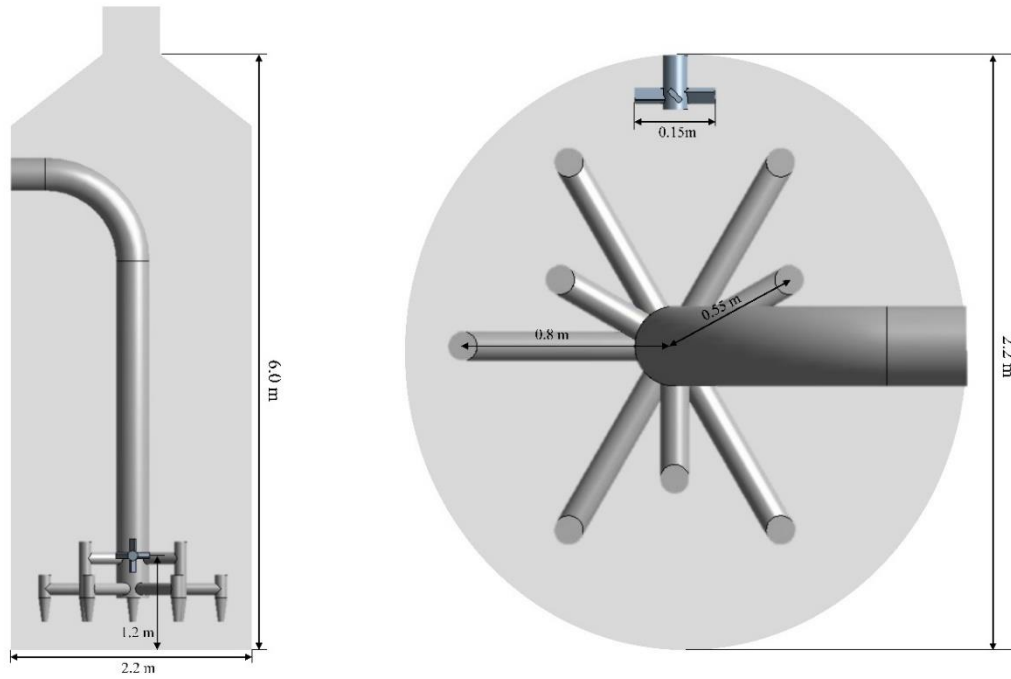
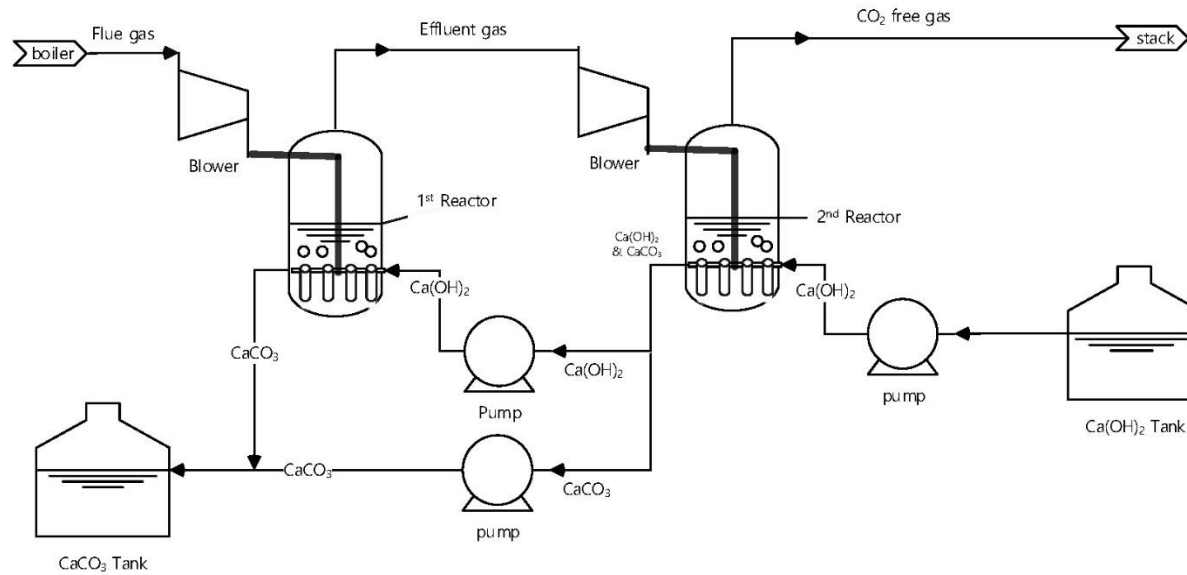


Figure 2-1. Side views of Gas distributor and nozzle structures of type A & B.



**Figure 2-2. Side and top view of the reactor.**



**Figure 2-3. Process flow diagram of the pilot-scale aqueous mineral carbonation process.**

In this study, three experiments were carried out (Table 2-1). In each experiment, two reactor conditions were set equal for solution concentration and temperature, but not for initial solution height of each reactor. The CO<sub>2</sub> concentrations at the entrance and exit were measured by CO<sub>2</sub> analyzer, DETA 1600-S IV.

The CO<sub>2</sub> removal efficiency was calculated according to the following definition:

The CO<sub>2</sub> *removal efficiency* =

$$\frac{\text{amount of the CO}_2 \text{ mass transferred from gas to liquid}}{\text{total amount of the CO}_2 \text{ flows into the reactor}}$$

Eq . 2-1

**Table 2-1. Three experiments conditions.**

	<b>Experiment I</b>	<b>Experiment II</b>	<b>Experiment III</b>
<b>Ca(OH)<sub>2</sub> (wt%)</b>	20	20	20
<b>NaOH (wt%)</b>	0.5	0	0.5
<b>Temperature (°C)</b>	35	70	35
<b>1<sup>st</sup> reactor solution height (m)</b>	2	2	1
<b>2<sup>nd</sup> reactor solution height (m)</b>	2	2	2

## **2.3 Model description**

### **2.3.1 Numerical setup**

The numerical simulations were carried out with the commercial software ANSYS CFX 16.2. As a geometry and mesh generator DesignModeler and AnsysMeshing were used, respectively. In order to reduce the computational cost, the geometry of the reactor was set up to height of 4.0 m, although that of the pilot-scale reactor is 6.0 m. Since  $\text{Ca}(\text{OH})_2$  mixed solution only filled up to 2.0 m, it was sufficient to simulate only 4.0 m of the reactor. The number of computational nodes was 265 439 and minimum orthogonal quality was 0.22 indicating the mesh was acceptable. Additionally, mesh test was carried out in order to make sure invariable results by the change of the number of nodes. Table 2-2 shows the mesh test results.

**Table 2-2. Mesh test results for gas holdup, interfacial area, and amount of mass transfer rate in Experiment II 1st reactor at 15 s.**

<b># of nodes</b>	<b>Gas holdup</b>	<b>Interfacial area (m<sup>-1</sup>)</b>	<b>Amount of Mass transfer (ton)</b>
<b>144 348</b>	0.3249	289.6	11.47
<b>265 439</b>	0.3261	290.8	11.81
<b>425 923</b>	0.3214	286.5	11.36

Density of solution was calculated with the following equation:

$$\rho_m = \frac{100}{\left(\frac{c_w}{\rho_s}\right) + \left[\frac{100-c_w}{\rho_l}\right]} \quad \text{Eq. 2-2}$$

Viscosity of solution was obtained through modified Einstein equation [40]:

$$\mu_m = \mu_l(1 + 2.5\phi + 14.1\phi^2) \quad \text{Eq. 2-3}$$

The viscosities of the solutions in Experiment I & III and II were calculated as 1.44 and 0.8256 mPa · s, respectively.

It is reported that the surface tension of a supersaturated Ca(OH)<sub>2</sub> solution is only 2% lower than that of pure water [41]. Thus, we assumed that the surface tensions of the solutions were 2 % lower than that of pure water in the same temperature. Consequently, surface tensions of solutions in Experiment I & III and II were calculated as 0.0671 N/m and 0.0631 N/m, respectively

In the CFD model, the presence of solids was taken into account by the change of physical properties of solids, such as viscosity and surface tension. According to Koide et al. [42], at high gas flow rates, the solid particle effects diminished to a negligible level and consequently, the correlation of Akita and Yoshida [43], which was

derived without solid particle, was adequate for g-l-s three-phase system. Ying et al. [44] said effect of adding solid particles was high in transition regime, but low in a heterogeneous flow. Since the particles effects could be ignored under our experimental conditions of a heterogeneous flow regime with a large  $u_g$  of 0.322 m/s, a two-phase (g-l) model with modified physical properties was used instead of the three-phase model [45].

For the gas phase, the turbulence viscosity was set to zero because of the diluteness of phase, whereas for the liquid phase, a standard  $k-\epsilon$  model was used. At the reactor wall and the impeller, free-slip and no-slip condition were used as boundary conditions of the gas and liquid, respectively. For the three experiments, the gas mass flow rate was set to 1.28 kg/s, 3 500 Nm<sup>3</sup>/hr, with 10 vol.% of CO<sub>2</sub> and the rest of N<sub>2</sub>. Outlet condition was set to degassing condition in which only gas could be discharged. An impeller with a 4-pitched blade was simulated using multiple reference frame (MRF) model and the speed was set to 150 rpm. Since the direction of gravity vector and the axis of the impeller was different from z to x-axis, steady state model could not be employed. Consequently, a transient model was used. To increase convergence of the model, the CFD simulation was first

carried out with timestep of  $10^{-6}$  s for  $10^{-3}$  s, and then CFD simulation was carried out with timestep of  $10^{-3}$  s for 1 s applying the precedent result as an initial condition. Finally, setting the previous result to the initial condition, the CFD simulation was carried out with timestep of 0.01 s until the CFD model converged, which occurred after less than 15 s. In Figure 2-4, the gas holdup and the amount of mass-transferred  $\text{CO}_2$  were plotted over the time, and it was confirmed that the CFD model converged less than 15 s.

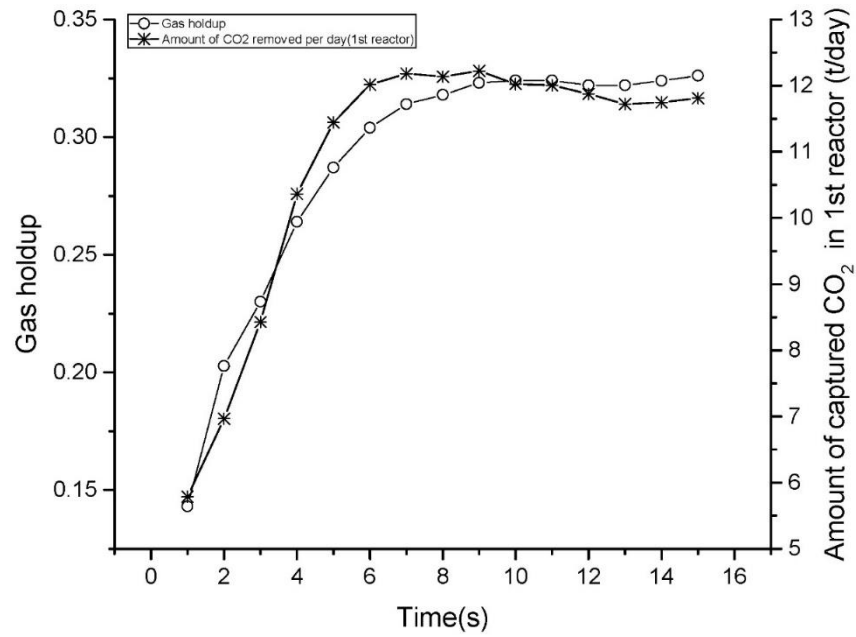


Figure 2-4. Gas holdup & amount of mass-transferred CO<sub>2</sub> (t/day) in 1<sup>st</sup> reactor for 15 s.

In order to obtain the amount of mass-transferred CO<sub>2</sub> and the interfacial area in the CFD model, zones with a gas volume fraction less than 0.8 were found in ANSYS CFD-Post. After that, the bulk interphase mass transfer rate of the volume -averaged CO<sub>2</sub> solution and the interfacial area (Eq. 2-26)) were calculated in the zones, and multiplied by the volume of the zones. The reason for excluding zones with a gas volume fraction of greater than 0.8 was to correct the limitation of Eqs. 2-16 & 2-19, which are inappropriate to use on high gas volume fraction. The zones had relatively large mass transfer rate, because high gas volume fraction made large interfacial area and small bubble diameter (See Eq. 2-16), and small bubble diameter made large mass transfer coefficient (See Eq. 2-19). However, if the gas volume fraction is too high, this high gas volume fraction makes a smaller interfacial area and a bigger bubble diameter. Considering that the volume of the zones only accounted for 0.3% of the total mixture volume and that the amount of mass-transferred CO<sub>2</sub> in the zones accounted for only 3% of the total amount, the above correction was acceptable.

For the purpose of obtaining the CO<sub>2</sub> removal efficiency of the CFD model, when the flue gas flowed into the process, the average

amount of mass-transferred CO<sub>2</sub> in the first reactor was calculated through an averaging the amount after converged, i.e., 10 s; this value was used to determine the state of effluent gas. Subsequently, setting the input condition to state of the effluent gas, the average amount of mass-transferred CO<sub>2</sub> in the second reactor was calculated. Finally, the CO<sub>2</sub> removal efficiencies were obtained from Eq. 2-1.

In ANSYS CFX 16.2, the hybrid finite-element and finite-volume approach was used to discretize Navier-Stokes equations. Using the finite-volume approach, global conservation was satisfied by the enforcing local conservation over control volumes. On the other hand, the finite-element approach was used to simulate the variations of the solution for each element. A ‘high resolution’ was selected as the advection scheme which is second-order accurate and bounded, and a ‘second order backward Euler’ was selected as the transient scheme. For the turbulence numeric option, a high resolution option was employed. The convergence control loops were in a range of 1-5. The convergence target set of  $10^{-4}$  for the root mean square (RMS) was achieved.

### 2.3.2 Governing equations

As a g-l two-phase model, a Eulerian-Eulerian (E-E) approach was employed in which the ensemble-averaging of the local instantaneous equations for a single-phase flow was used to obtain the equation for the two-fluid model without tracking all the bubbles individually. The mass and momentum conservation equation with the interphase mass transfer is written below:

$$\frac{\partial(\alpha_k \rho_k)}{\partial t} + \nabla \cdot (\alpha_k \rho_k \mathbf{u}_k) = -\dot{m}_{k \rightarrow l} \quad \text{Eq. 2-4}$$

$$\frac{\partial(\alpha_k \rho_k \mathbf{u}_k)}{\partial t} + \nabla \cdot (\alpha_k \rho_k \mathbf{u}_k \mathbf{u}_k) = \nabla \cdot (\alpha_k \mu_{eff} (\nabla \mathbf{u}_k + (\nabla \mathbf{u}_k)^T)) - \alpha_k \nabla p_k + \mathbf{M}_k - \dot{m}_{k \rightarrow l} \mathbf{u}_k \quad \text{Eq. 2-5}$$

Where k refers to the phase, and  $\mathbf{M}$  is inter-phase momentum exchange between one phase and all the other phases, respectively.  $\dot{m}_{k \rightarrow l}$  is mass transfer rate from phase k to l.

Because we considered only the gas and solution phases and the solution phase is liquid phase with modified physical properties for taking into account of solids,  $\mathbf{M}_m$  and  $\mathbf{M}_g$  can be described by the following expression:

$$\mathbf{M}_m = -\mathbf{M}_g = \mathbf{M}_{m,D} + \mathbf{M}_{m,L} + \mathbf{M}_{m,VM} \quad \text{Eq. 2-6}$$

$$\mathbf{M}_{m,D} = \frac{3}{4} \alpha_g \rho_m \frac{C_D}{d_B} |\mathbf{u}_g - \mathbf{u}_m| (\mathbf{u}_g - \mathbf{u}_m) \quad \text{Eq. 2-7}$$

$$\mathbf{M}_{m,L} = \alpha_g \rho_m C_L (\mathbf{u}_g - \mathbf{u}_m) \times \nabla \times \mathbf{u}_m \quad \text{Eq. 2-8}$$

$$\mathbf{M}_{m,VM} = \alpha_g \rho_m C_{VM} \left( \frac{D_g \mathbf{u}_g}{Dt} - \frac{D_m \mathbf{u}_m}{Dt} \right) \quad \text{Eq. 2-9}$$

Where the right hand terms represent the drag, lift, and virtual mass force, and  $C_D$ ,  $C_L$ , and  $C_{VM}$  are the coefficients of these force. Since a high gas volume fraction causes numerical problems, special measurements were taken for the drag, lift, and virtual mass force coefficients [46, 47].  $C_D$ ,  $C_L$ , and  $C_{VM}$  were set to 0.44, 0.5, and 0.25 for the condition of  $\alpha_g < 0.45$  and 0.05, 0, and 0 of  $\alpha_g > 0.45$ . It should be noted that there is a boundary between the solution and the gas cap. In the solution region,  $\alpha_g$  is less than 0.45. In the gas cap region,  $\alpha_g$  is greater than 0.45 and is about 0.98. If  $C_D$  of 0.44 was used in the gas cap region instead of 0.05, gas ( $\alpha_g \approx 0.98$ ) would have lifted the solution indefinitely to the outlet, leading to numerical problems [46, 47]. This is why there is a large discrepancy in the values of the coefficients at  $\alpha_g$  of 0.45.

$\mu_{eff}$  is effective viscosity, and was obtained from the following equation:

$$\mu_{eff} = \mu_m + \mu_{t,m} \quad \text{Eq. 2-10}$$

The turbulence viscosity of the solution was calculated as follows:

$$\mu_{t,m} = \rho_m C_\mu \frac{k_m^2}{\epsilon_m} \quad \text{Eq. 2-11}$$

The turbulence kinetic energy ( $k_m$ ) and energy dissipation rate ( $\epsilon_m$ ) of the solution were obtained from a standard  $k - \epsilon$  model. The governing equations are written below:

$$\begin{aligned} \frac{\partial}{\partial t} (\rho_m \alpha_m k_m) + \nabla \cdot \left( \alpha_m (\rho_m \mathbf{u}_m k_m - \left( \mu_m + \frac{\mu_{t,m}}{\sigma_k} \right) \nabla k_m) \right) \\ = \alpha_m (P_m - \rho_m \epsilon_m) \end{aligned} \quad \text{Eq. 2-12}$$

$$\begin{aligned} \frac{\partial}{\partial t} (\rho_m \alpha_m \epsilon_m) + \nabla \cdot \left( \alpha_m \rho_m \mathbf{u}_m \epsilon_m - \left( \mu_m + \frac{\mu_{t,m}}{\sigma_\epsilon} \right) \nabla \epsilon_m \right) = \\ \alpha_m \frac{\epsilon_m}{k_m} (C_{1\epsilon} P_m - C_{2\epsilon} \rho_m \epsilon_m) \end{aligned} \quad \text{Eq. 2-13}$$

Where the constants of the standard  $k-\epsilon$  model parameters  $C_\mu$ ,  $C_{1\epsilon}$ ,  $C_{2\epsilon}$ ,  $\sigma_k$ , and  $\sigma_\epsilon$  are 0.09, 1.44, 1.92, 1.0 and 1.3, respectively. The term  $P_m$ , the turbulence production due to buoyancy and viscous forces, is described by:

$$P_m = \mu_{t,m} \nabla \mathbf{u}_m \cdot (\nabla \mathbf{u}_m + \nabla \mathbf{u}_m^T) - \frac{2}{3} \cdot \nabla \mathbf{u}_m (3\mu_{t,m} \nabla \cdot \mathbf{u}_m + \rho_m k_m)$$

Eq. 2-14

The mass transfer rate of the CO<sub>2</sub> per unit volume from a gas to a solution phase was defined as:

$$\dot{m}_{g \rightarrow m} = k_L a E \rho_m (Y_{gm,e}^{CO_2} - Y_m^{CO_2}) \quad \text{Eq. 2-15}$$

Where  $k_L$ ,  $a$ ,  $E$ ,  $Y_{gm,e}^{CO_2}$ , and  $Y_m^{CO_2}$  are the overall mass transfer coefficient for the CO<sub>2</sub>, interfacial area per unit volume, the enhancement factor due to the chemical reaction, the mass fraction of CO<sub>2</sub>(aq) in the liquid phase, and mass fraction of CO<sub>2</sub>(g) in the liquid phase, which was assumed zero.

The interfacial area was calculated from the following Hibiki and Ishii [39] correlation:

$$a = \frac{3.02g^{0.174}}{D^{0.335}v_m^{0.239}} \left( \frac{\sigma_m}{\rho_m - \rho_g} \right)^{-0.174} \alpha_g \epsilon_m^{0.0796} \quad \text{Eq. 2-16}$$

Due to the negligible impeller effect of the pilot-scale reactor, Eq. 2-16 used in bubble column was employed. By comparing results of rotating and non-rotating model that had a geometry of impeller but not rotate, it was confirmed that the effect of tiny impeller on the hydrodynamics was trivial (Figure 2-5), and consequently the pilot-scale reactor was assumed to be a bubble column.

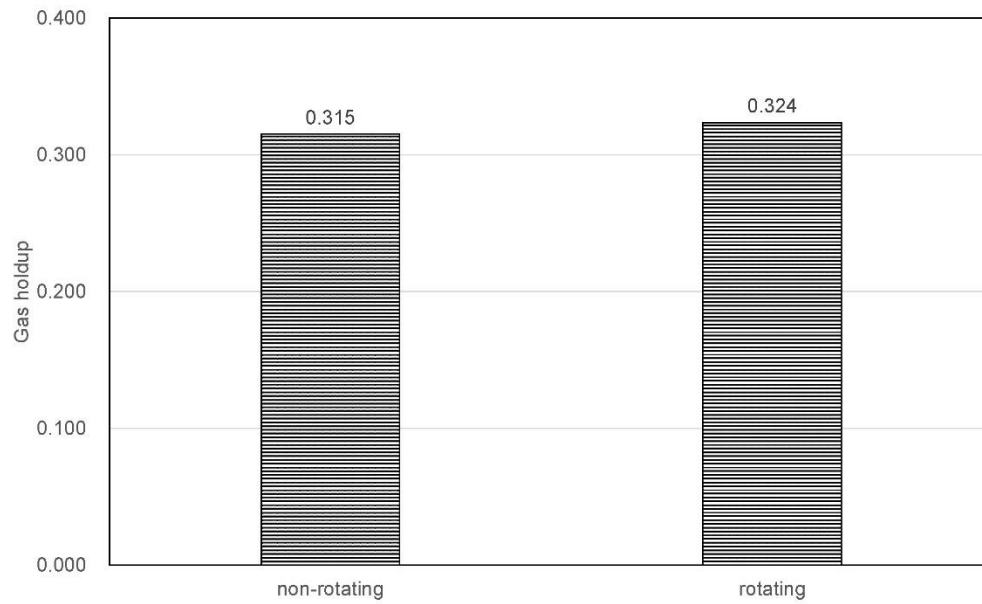


**Figure 2-5. Gas holdup in rotating and non-rotating conditions.**

On the other hand, Eq. 2-16 was first derived from the one-dimensional bubble number density and interfacial area transport equations which take account of the bubble breakage and coalescence, wall nucleation, and developing flow. The one-dimensional bubble number density and interfacial area transport equations are described by [48-50]:

$$\frac{\partial n}{\partial t} + \frac{d}{dz}(nv_p) = (\phi_B - \phi_C) + (\phi_{PN} - \phi_{PC}) \quad \text{Eq. 2-17}$$

$$\begin{aligned} \frac{\partial a}{\partial t} + \frac{d}{dz}(av_i) &= \frac{1}{3\psi} \left(\frac{\alpha_g}{a}\right)^2 \{(\phi_B - \phi_C) + (\phi_{PN} - \phi_{PC})\} + \\ &\left(\frac{2a}{3\alpha_g}\right) \left\{ \frac{\partial \alpha_g}{\partial t} + \frac{d}{dz}(\alpha_g v_i) \right\} \end{aligned} \quad \text{Eq. 2-18}$$

Where  $\phi_B$ ,  $\phi_{PN}$ ,  $\phi_C$ , and  $\phi_{PC}$  are the increase rate of the bubble number density by the bubble breakage, the bubble nucleation, the decrease rate of the bubble number density by bubble coalescence, and bubble collapse, respectively. Subsequently, the theoretical equation was modified by extensive data sets taken in the bubble columns to be applicable to different conditions. The reason this correlation was used is to reduce the computational cost. In the CFD-lumped correlation model, the bubble breakage and coalescence phenomena were considered by using this correlation instead of taken

into account all in CFD.

In the experimental conditions, the bubble lost spherical shape due to the high superficial velocity, i.e.,  $Re$  was larger than critical  $Re$ , which is the criteria for losing the spherical shape. Accordingly, in order to consider the influence of the deformation, the mass transfer coefficient for non-spherical bubbles was calculated by the Sherwood relation described by Brauer [51]:

$$Sh = \frac{k_L d_B}{D_{CO_2}} = 2 + 0.015 Re^{0.89} Sc^{0.7} \quad \text{Eq. 2-19}$$

The equation for obtaining  $D_{CO_2}$  was suggested by Ratcliff and Holdcroft [52]:

$$\frac{D_{CO_2}}{D_{CO_2}^w} = 1 - 1.29 \times 10^{-4} [OH^-] \quad \text{Eq. 2-20}$$

The Versteeg and Van Swaaij [53] equation for the diffusivity of  $CO_2(g)$  in pure water is written below:

$$D_{CO_2}^w = 2.35 \times 10^{-6} e^{\frac{2119}{T}} \quad \text{Eq. 2-21}$$

The bubble diameters were described by below equation:

$$a = \frac{6\alpha_g}{d_B} \quad \text{Eq. 2-22}$$

Using the Henry's law,  $Y_{gm,e}^{CO_2}$  was obtained as follows:

$$Y_{\text{gm,e}}^{\text{CO}_2} = H^{\text{CO}_2} Y_g^{\text{CO}_2} \frac{\rho_g}{\rho_m} \quad \text{Eq. 2-23}$$

Where  $H^{\text{CO}_2}$ , and  $Y_g^{\text{CO}_2}$  are the solubility coefficient of  $\text{CO}_2(\text{g})$  in an aqueous electrolytic solution, and the mass traction of  $\text{CO}_2(\text{g})$  in the gas phase, respectively. In order to calculate  $H^{\text{CO}_2}$ , the Weisenberger and Schumpe [54] equation was used:

$$\log\left(\frac{H_w^{\text{CO}_2}}{H^{\text{CO}_2}}\right) = \sum(h_i + h_g)c_i \quad \text{Eq. 2-24}$$

Where  $H_w^{\text{CO}_2}$ ,  $h_i$ ,  $h_g$ , and  $c_i$  are the solubility coefficient of  $\text{CO}_2(\text{g})$  in pure water, the ion-specific parameter, the gas-specific parameter, and the concentration of ion I, respectively.  $H_w^{\text{CO}_2}$  was taken from equation of Versteeg and Van Swaaij [53]:

$$H_w^{\text{CO}_2} = 3.59 \times 10^{-7} RT e^{\frac{2044}{T}} \quad \text{Eq. 2-25}$$

Under basic conditions of a  $\text{Ca}(\text{OH})_2$  mixed solution with a pH higher than 10, the enhancement factor, which is important to take into account of the chemical absorption of  $\text{CO}_2$  by  $\text{OH}^-$ , was calculated as following the Westerterp et al. [55] equation:

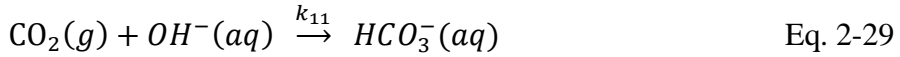
$$E = \begin{cases} -\frac{Ha^2}{2(E_\infty - 1)} + \sqrt{\frac{Ha^4}{4(E_\infty - 1)^2} + \frac{E_\infty Ha^2}{E_\infty - 1}} + 1, & E_\infty > 1 \\ 1, & E_\infty \leq 1 \end{cases} \quad \text{Eq. 2-26}$$

Where

$$E_{\infty} = \left( 1 + \frac{[OH^{-}]D_{OH^{-}}}{2D_{CO_2}H^{CO_2}[CO_2(g)]} \right) \times \sqrt{\frac{D_{CO_2}}{D_{OH^{-}}}} \quad \text{Eq. 2-27}$$

$$Ha = \frac{\sqrt{k_{11}D_{CO_2}[OH^{-}]}}{k_L} \quad \text{Eq. 2-28}$$

and  $[OH^{-}]$ ,  $D_{OH^{-}}$ ,  $[CO_2(g)]$ , and  $k_{11}$  are concentration of  $OH^{-}$ , the diffusivity of  $OH^{-}$  in the solution, the concentration of  $CO_2(g)$ , and the forward reaction rate constant of below chemical absorption reaction of  $CO_2(g)$ :



$k_{11}$  was calculated via the relation of Pohorecki and Moniuk [56] :

$$\log\left(\frac{k_{11}}{k_{11}^{\infty}}\right) = 0.22I - 0.016I^2 \quad \text{Eq. 2-30}$$

Where  $I$  is the ionic strength, and the reaction rate constant at a dilute solution,  $k_{11}^{\infty}$ , was given by:

$$\log(k_{11}^{\infty}) = 11.895 - \frac{2382}{T} \quad \text{Eq. 2-31}$$

On the other hand, the  $D_{OH^{-}}$  value at 298 K,  $5.3 \cdot 10^{-9} \text{ m}^2/\text{s}$ , was used for  $D_{OH^{-}}$  at 308 and 343 K because the value of  $D_{OH^{-}}$  in a range of  $10^{-4}$  to  $10^{-11}$  does not change the value of  $E$ .

## **2.4 Results and discussion**

### **2.4.1 CFD model feasibility test**

In this part, the CFD model results of the pilot-scale reactor were compared with the experimental data and the empirical correlations in the literatures for the gas holdup, the interfacial area, and the mass transfer coefficient; these hydrodynamics parameters are vital to obtain the mass transfer rate in 2.4.2.

#### **2.4.1.1 Gas holdup ( $\alpha_g$ )**

The gas holdup is one of the most important parameters for a reactor, and a reliable CFD model should be able to predict its value with considerable accuracy. Therefore, in order to ensure the feasibility of CFD model, simulations were carried out for three cases in Experiment II for first reactor conditions at the same superficial velocity: Case I column diameter 60 cm, Case II column diameter 2.2 m with low performance gas distributor, Case III the pilot-scale reactor, i.e., column diameter 2.2 m with high performance gas distributor. Case I and II have the same gas distributor structure with a diameter of 20 cm and height of 5 cm, and inlet condition was that gas could be blow out evenly through all over the side face (See Figure

2-6). By comparing the CFD results with two widely accepted empirical correlations, Eq. 2-32 and Eq. 2-33 (Hikita et al. [57]), the CFD model verifications were conducted.

$$\frac{\alpha_g}{(1-\alpha_g)^4} = 0.25 \left( \frac{gD^2 \rho_m}{\sigma_m} \right)^{\frac{1}{8}} \left( \frac{gD^3}{v_m^2} \right)^{\frac{1}{12}} \left( \frac{U_g}{\sqrt{gD}} \right) \quad \text{Eq. 2-32}$$

$$\alpha_g = 0.505 U_G^{0.47} \left( \frac{0.072}{\sigma_m} \right)^{\frac{2}{3}} \left( \frac{0.0001}{\mu_m} \right)^{0.05} \quad \text{Eq. 2-33}$$

Although Eqs. 2-32 & 2-33 were derived in a laboratory-scale bubble column and require only information for the physical properties and reactor diameter without considering the reactor or gas distributor structure, those could be employed in the pilot-scale reactor because Kataoka et al. [58] compared experimental results for a large bubble column with Eq. 2-32 and showed the acceptability of Eq. 2-32 with errors in the confidence interval.

Figure 2-7 shows the gas holdup profiles of the three cases and Figure 2-8 shows a comparison of the gas holdup from the CFD model and from Eqs. 2-32 & 2-33.

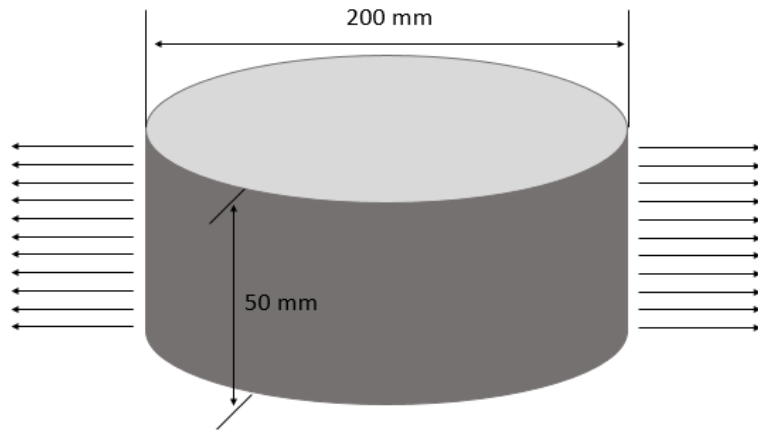


**Figure 2-6. Gas distributor structure of Cases I & II.**

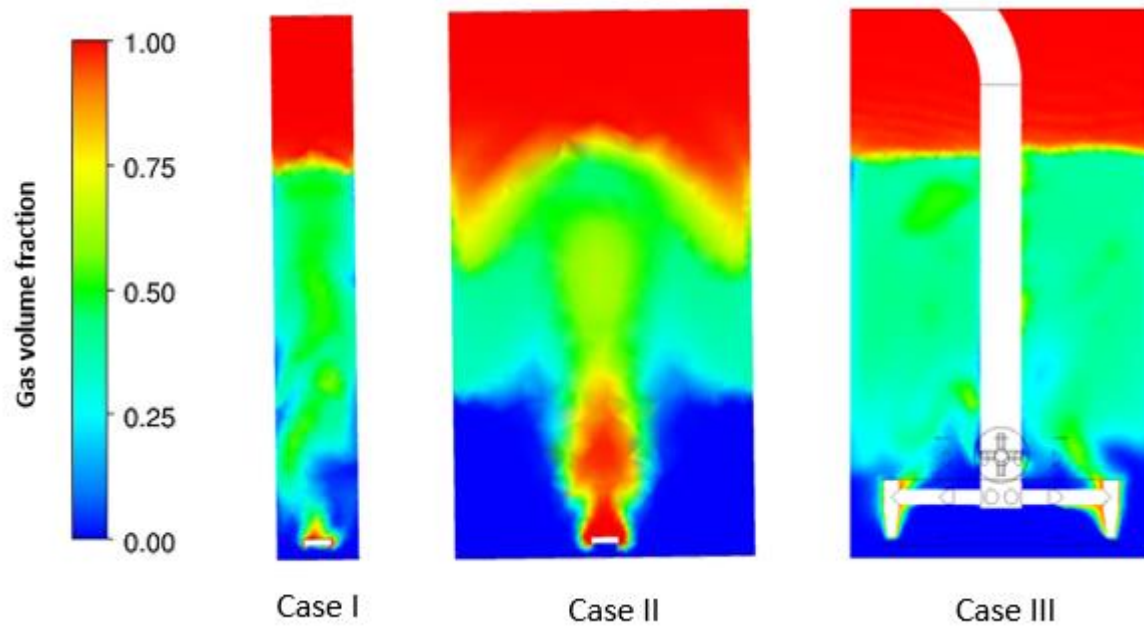


**Figure 2-7. Gas holdup profiles in the three cases.**

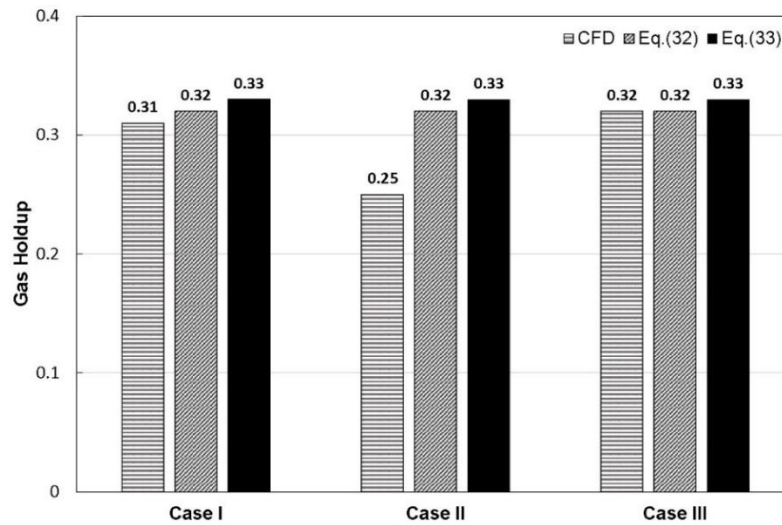


**Figure 2-8. Gas holdup from the CFD model and Eqs. 2-32 & 2-33.**

In Case I and III, the CFD model showed a good agreement with Eqs. 2-32 & 2-33 in errors below 7%, and the gas holdup profiles showed even distribution of the gas in each case. Meanwhile, despite of large differences of the column diameter and gas distributor, Eqs. 2-32 & 2-33 predicted the same gas holdup for all the cases (See Figure 2-8; 0.32 for Eq. 2-32 and 0.33 for Eq. 2-33). The reason was due to the Akita and Yoshida [59] recommendation: when the column diameter is larger than 0.6 m, use the value at 0.6 m. Notable point was that the CFD model also showed similar amount of gas holdup in Case I and III representing the relevance of the recommendation by Akita and Yoshida [59].

In Case II, however, the CFD model resulted in a considerable difference in the values derived from Eqs. 2-32 & 2-33. This was presumably due to the fact that the gas distributor in Case II was not enough to distribute the gas evenly and Eqs. 2-32 & 2-33 could not take the performance of the gas distributor into consideration (See Fig 7, Case II). The effect of the gas distributor on the gas holdup was revealed in the CFD results; the better the distribution of the gas, the higher the gas holdup was. As a result, in case the gas distributor performance is not sufficient to distribute the gas evenly, special

measurements are required to use Eqs. 2-32 & 2-33.

In sum, the CFD models not only predicted the gas holdup well but also took into account of the reactor and gas distributor structure, though Eqs. 2-32 & 2-33 did not.

#### **2.4.1.2 Interfacial area ( $a$ )**

The interfacial area varies drastically according to the bubble breakage and coalescence phenomena. These phenomena were considered by using Eq. 2-16 to reduced computational cost in the CFD model, whereas previous studies used the PBM. Therefore, the CFD model needed verification for the interfacial area. For the verification, the CFD results were compared with experimental result of Kataoka et al. [58] . According to the experimental result, the interfacial area of a large bubble column was one-third of the value predicted by Eq. 2-34, which is most widely used but was derived in a laboratory-scale bubble column. The Table 2-3 shows the interfacial area obtained from the CFD model and Eq. 2-34 in Experiment II first reactor conditions; the CFD result agreed well with experimental result showing almost one-third of the value predicted from Eq. 2-34,

$$a = \frac{1}{3D} \left( \frac{gD^2\rho_m}{\sigma_m} \right)^{0.5} \left( \frac{gD^3}{v_m^2} \right)^{0.1} \alpha_g^{1.13} \quad \text{Eq. 2-34}$$

**Table 2-3. Interfacial area obtained from Eq. 2-34 and the CFD model.**

<b>Interfacial area (m<sup>-1</sup>)</b>	
<b>Eq. 2-34</b>	775.0
<b>CFD model</b>	288.5

The cause of the considerable difference could be found on a drawback of Eq. 2-34. First, it is only available when the gas holdup is less than 0.3, whereas the experimental condition was above 0.3. Second, it was derived without consideration of the reactor structure and gas distributor. As shown in Figure 2-7, the gas distributor significantly affects hydrodynamics.

In conclusion, though Eq. 2-34 had limitations to use in a large bubble column with complex structure and high gas holdup, the CFD model took all of factors into account.

#### ***2.4.1.3 Overall mass transfer coefficient ( $k_L$ )***

For the mass transfer coefficient, the validation proceeded by comparing the CFD model with the experimental results of Sada et al. [60] which carried out at the laboratory-scale with almost the same conditions as in Experiment I: 35 °C, Ca(OH)<sub>2</sub> 20 wt%, and a small amount of NaOH.

Table 2-4 shows considerable difference between the CFD model and the results of Sada et al. [60]. However, this result coincided with those of Kataoka et al. [58] for an experiment implemented in a large bubble column. According to Kataoka et al. [58], the mass transfer

coefficient obtained from a large bubble column was 30 - 40 % higher than that from a laboratory-scale. As shown in Table 2-4, the CFD model had almost 30 – 40 % higher value than Sada et al. [60] agreeing with the results of Kataoka et al. [58]. Though additional validation is required, the feasibility of the CFD model on the mass transfer coefficient was demonstrated.

**Table 2-4. Mass transfer coefficient from the CFD model and published data.**

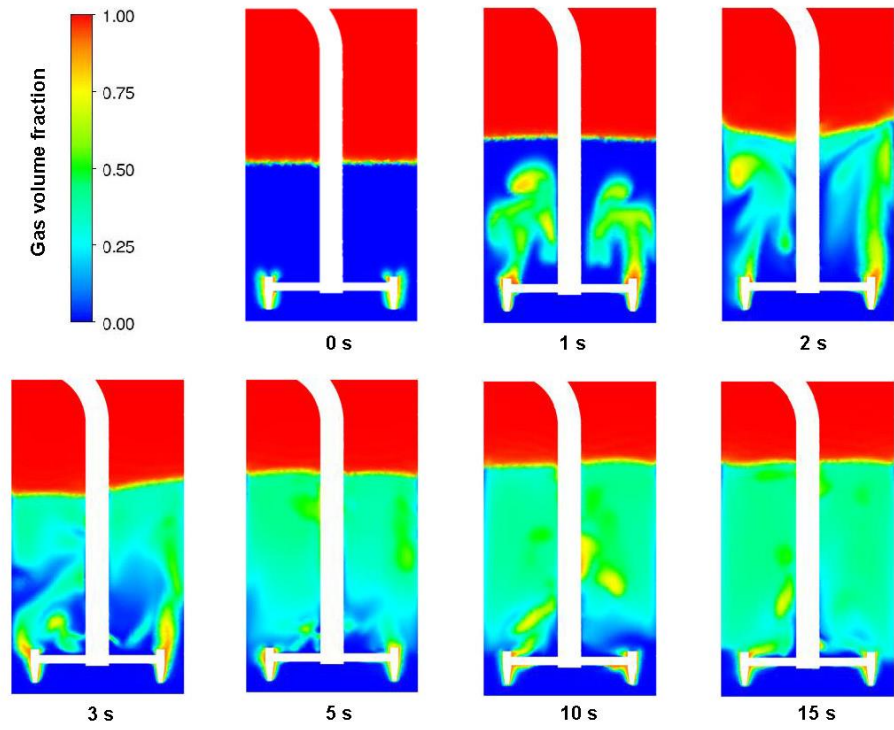
<b>Mass Transfer Coefficient (m/s)</b>	
CFD	$3.8 \times 10^{-4}$
Sada et al.	$2.6 \times 10^{-4}$
Sada et al. * 1.35	$3.5 \times 10^{-4}$
<b>Error(%)</b>	<b>8.26</b>

## 2.4.2 Hydrodynamic analysis in the CFD model

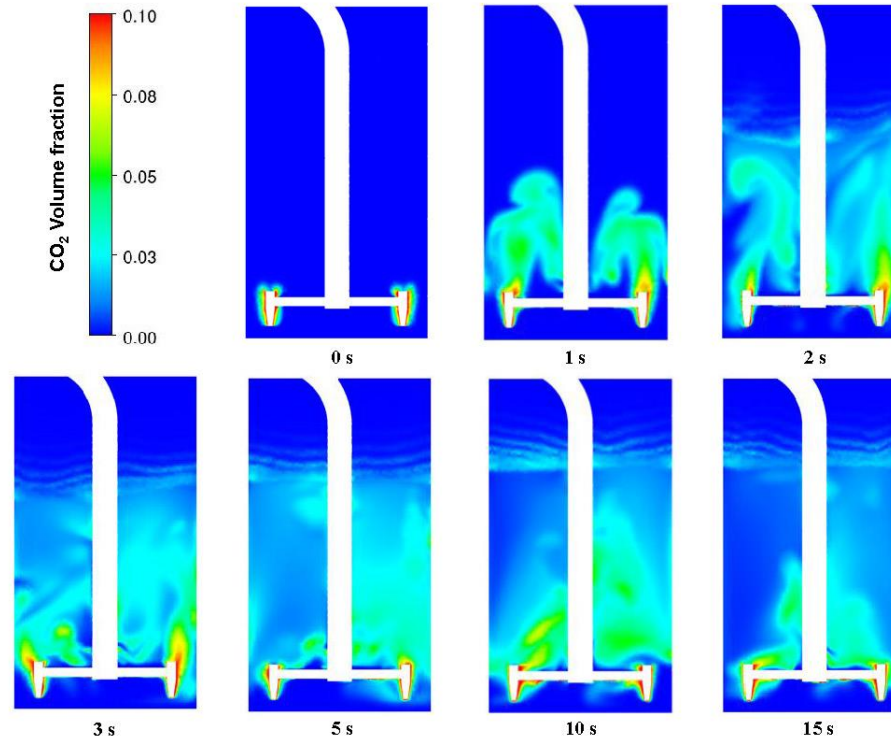
In this part, the CFD model results for gas holdup, CO<sub>2</sub> holdup, mass transfer rate, and bubble diameter are analyzed.

Figure 2-9 showed the gas holdup, CO<sub>2</sub> and N<sub>2</sub> holdup, profiles in Experiment II. At first, the solution occupied the height up to 2 m, and N<sub>2</sub> occupied the rest. Subsequently, the gas with 10 vol.% CO<sub>2</sub> flowed into the reactor. As mentioned that the gas holdup converged before 15 s in 2.3.1, the gas holdup profiles fluctuated dynamically first but remained almost unchanged after 10 s (See solution height in Figure 2-9). Figure 2-10 shows the CO<sub>2</sub> holdup profiles to see decreasing CO<sub>2</sub> volume fraction by mass transfer. Similar to the results shown in Figure 2-9, CO<sub>2</sub> holdup profiles converged before 10 s. Notable point was that CO<sub>2</sub> volume fraction at the bottom part was higher than at the top, indicating that the CO<sub>2</sub> was mass transferred over time. The gas volume fraction at the bottom was lower than at the top. For further details of the mass transfer rate, Figure 2-11 shows the mass transfer rate profile, and it was confirmed that the mass transfer rate was faster at the bottom part due to the higher CO<sub>2</sub> volume fraction. Figure 2-12 shows the bubble diameter profiles. The bubble diameter around nozzles was almost 5 mm, which is the diameter of the nozzle holes.

As the bubbles rose, they became larger and finally grew up to about 6.5 mm and converged. From Figure 2-12, it is confirmed that the CFD model could provide reasonable results on the bubble diameter.



**Figure 2-9. Gas holdup profiles of the CFD model based on operating time of 0 - 15 s.**



**Figure 2-10. CO<sub>2</sub> holdup profiles of the CFD model based on operating time of 0 - 15 s.**

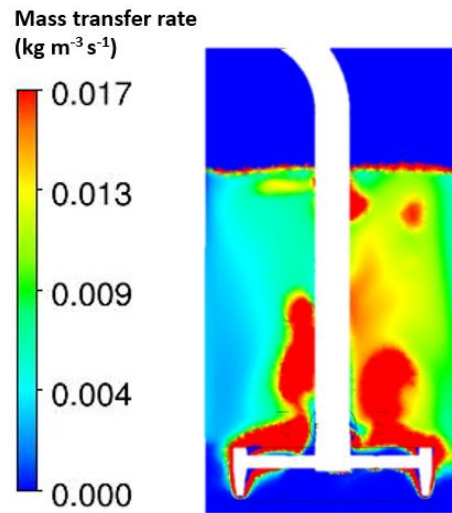


**Figure 2-11. Mass transfer rate profile of the CFD model at 15 s.**

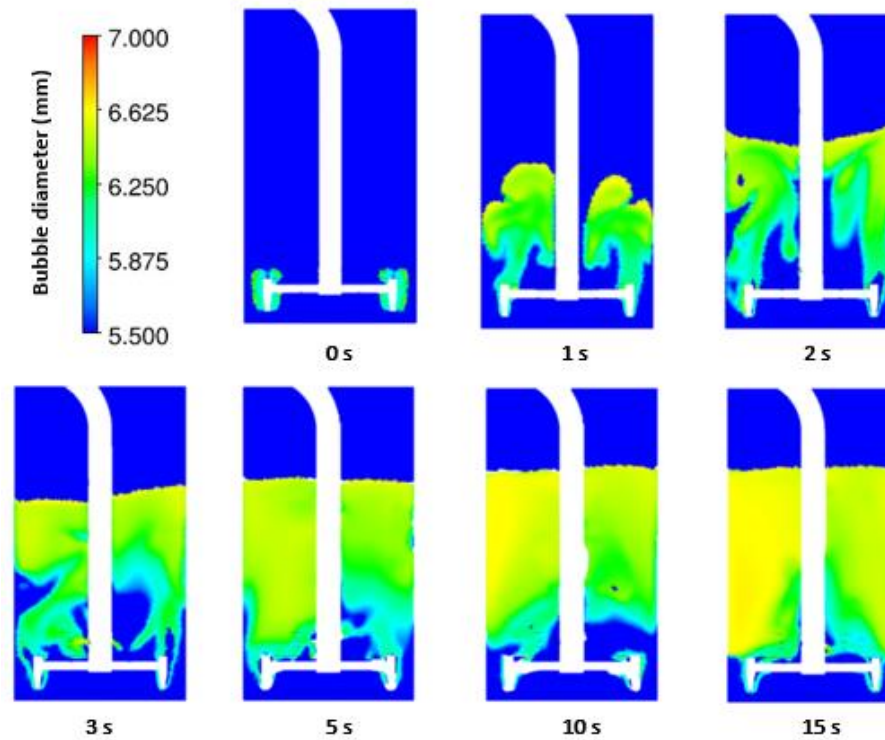


Figure 2-12. Bubble diameter profiles of the CFD model based on operating time of 0 - 15 s.

### **2.4.3 CFD model verification by comparing with actual pilot-plant**

Finally, in this section, the CO<sub>2</sub> removal efficiencies of the CFD model were calculated from the validated hydrodynamics parameters in 2.4.1, followed by a comparison with the pilot-plant data.

During operation of the pilot-plant, it was observed that the CO<sub>2</sub> removal efficiency varied within a small range. In Experiment I and II, the measured CO<sub>2</sub> removal efficiencies were 82 – 89 % and 90 – 97 %, respectively. There were two causes of errors. First, the flue gas was supplied by a near facility of waste disposal, hence the flowrate and CO<sub>2</sub> vol.% changed in a certain range. As a results, the varying flow gas conditions made the errors. Second, as shown in Figures 2-4 & 2-9, a fast flowrate affected the flow dynamics a lot and consequently, the hydrodynamics could not converge but fluctuated within an acceptable range; 3 500 Nm<sup>3</sup>/h is about 1 Nm<sup>3</sup>/s, whereas the solution volume was about 9 m<sup>3</sup>.

In Figure 2-13, the CO<sub>2</sub> removal efficiencies of the pilot-plant and the CFD model are compared. In the experiments, all errors were below 8 %. Considering that the CO<sub>2</sub> removal efficiencies of the pilot-plant fluctuated, it was concluded the CFD model showed acceptable

results. On the other hand, the reason the error was higher in Experiment III is attributed to the solution height of the first reactor. As shown in Figure 2-14, the flow fluctuated more actively in the 1-m solution height case than the 2-m height case, resulting in the observed error which cannot be simulated through only lumped correlation. Consequently, it is required to find new methodology that can consider turbulence effect in future work.

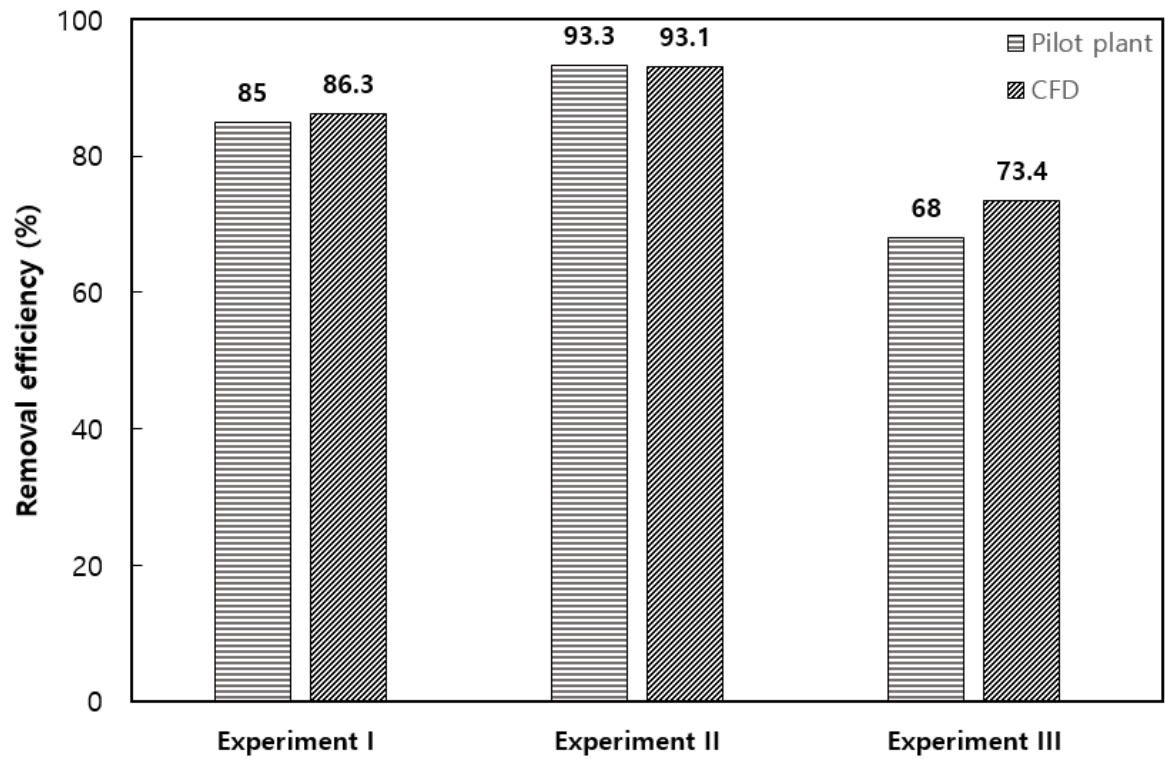


**Figure 2-13. Comparison of the CO<sub>2</sub> removal efficiencies between the CFD model and the experiments.**

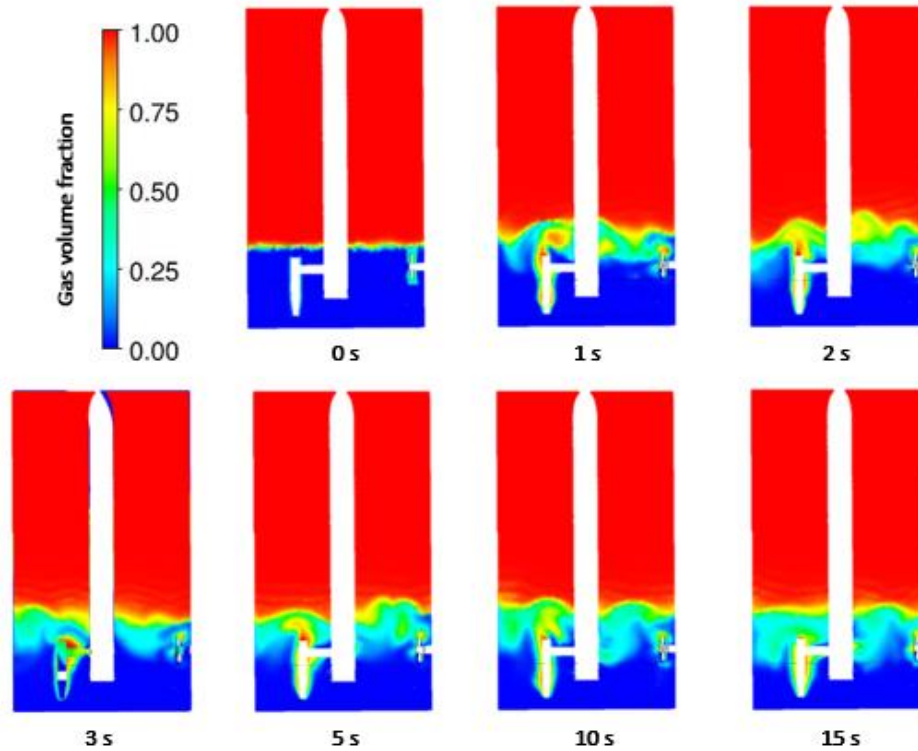


Figure 2-14. Gas holdup profiles of the CFD model for Experiment III 1<sup>st</sup> reactor based on an operating time of 0-15 s.

Although there were only three points available from the experiments, they were sufficient to cover the whole range of operating conditions. A temperature increase from 35°C to 70°C brought in a four-fold increase in  $k_{11}$  and E and in a decrease in the solution viscosity of 40%. Also, the addition of 0.5 wt% NaOH increased E by three times. Moreover, the solution height difference had a significant impact on the hydrodynamics. In other words, there were respectable differences of T, pH, and the solution height between the experiments and the differences made dramatic changes for the mass transfer parameters and hydrodynamics. In spite of this, reliable results were obtained.

## **CHAPTER 3. Long-time CFD simulation of industrial-scale reactors using CFD-based compartmental model<sup>#</sup>**

### **3.1 Objective**

In this chapter, to simulate pilot- and industrial-scale mineral carbonation reactors, the CFD-based compartmental model is used [61]. In this model, the CFD model calculates the hydrodynamics information, and using this information, the chemical reactions are calculated through the mass balance equations, in MATLAB. For the verification of this model, the model results are compared with the experimental results of pilot-scale and industrial-scale plant, respectively. Furthermore, this model is used to analysis the scaled-up reactors 2.5 and 10 times larger than an industrial-scale reactor.

---

<sup>#</sup> This chapter cites the author's published journal article: M. Kim, S. Park, D. Lee, S. Lim, M. Park, and J. M. Lee, "Modeling long-time behaviors of industrial multiphase reactors for CO<sub>2</sub> capture using CFD-based compartmental model," *Chemical Engineering Journal*, p. 125034, 2020 [61].

## 3.2 Experimental setup

Experiments were conducted at the pilot- and the industrial-scale plant. In section 2.2, the detail process flow diagram and the reactor configuration were given for the pilot-scale plant. The reactor configuration of the industrial-scale plant reactor is shown in Figure 3-1, and the process flow diagram of the industrial-scale plant is same as that for the pilot-scale plant.

The industrial-scale reactor is 4 m in diameter and 4 m in height. And shown in Figure 3-1, the sparger has a complex design with a lot of nozzles whose hole size is 8 mm. There are three pitched blade impellers, whose diameter is 2 m, at the middle of reactor. The impeller rotational speed was 30 rpm in all experiments.

In the industrial-scale process, the flue gas with a volumetric flow rate of 5000-7000 Nm<sup>3</sup>/h containing approximately 15 vol.% of CO<sub>2</sub> flows into the first reactor containing a Ca(OH)<sub>2</sub> solution. The effluent gas from the first reactor enters the second reactor to capture the remaining CO<sub>2</sub> after pressurization. The Ca(OH)<sub>2</sub> solution is filled in both the reactors until the reactions are complete and product mixtures

are drawn out. The other detail conditions for the process are given in Tables 3-1 and 2.

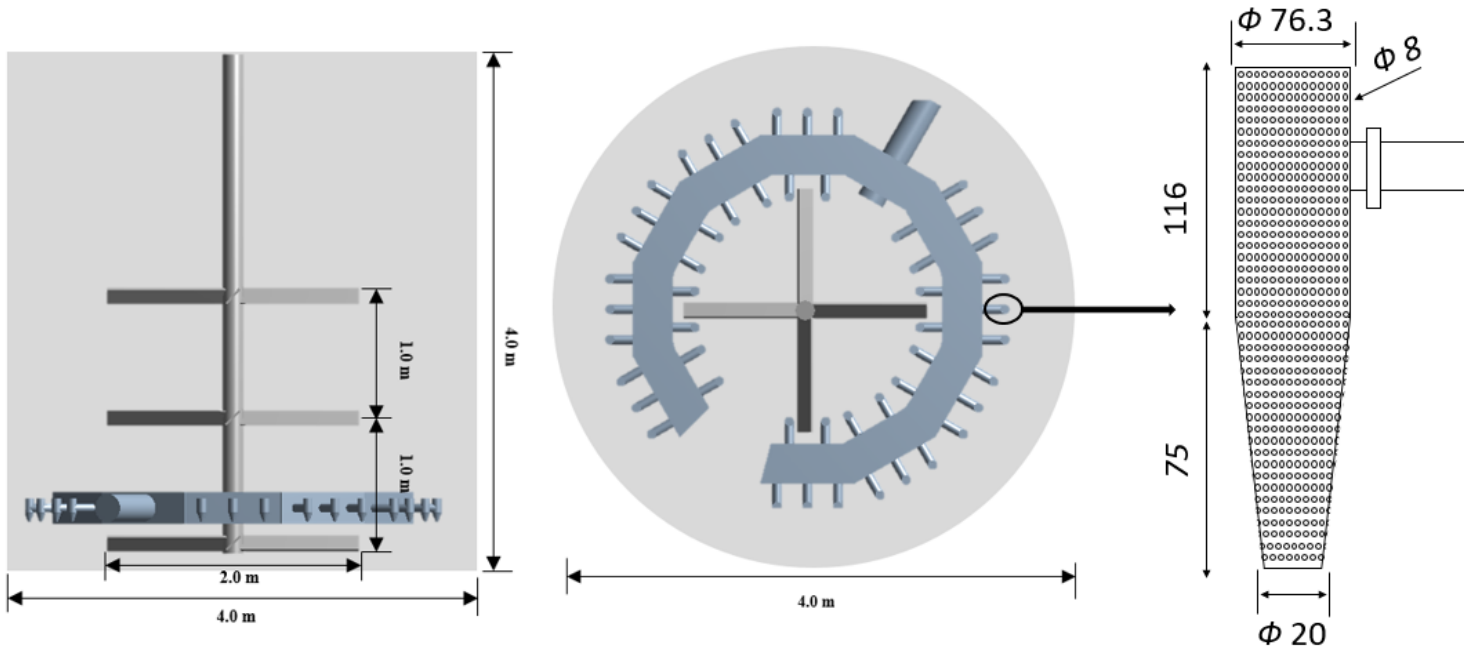


**Figure 3-1. Side view and top view of the industrial-scale reactor and configuration of nozzle.**

**Table 3-1. Experimental conditions for the pilot-scale process**

<b>Reactor</b>	<b>Experiment P-1</b>		<b>Experiment P-2</b>	
	<b>1st</b>	<b>2nd</b>	<b>1st</b>	<b>2nd</b>
<b>Inlet flow rate (Nm<sup>3</sup>/h)</b>	3500		3500	
<b>CO<sub>2</sub> (vol%)</b>	10		10	
<b>Reactor temperature(°C)</b>	35	35	70	70
<b>Initial solution height(m)</b>	2	2	2	2
<b>NaOH (wt%)</b>	0.5	0.5	0	0
<b>Ca(OH)<sub>2</sub> (wt%)</b>	20	20	20	20

**Table 3-2. Experimental conditions for industrial-scale process.**

Reactor	Experiment I-1		Experiment I-2			
	Day 1		Day 1		Day 2	
	Single	1st	2nd	1st	2nd	
<b>Inlet flowrate (Nm<sup>3</sup>/h)</b>	6027	6748			6748	
<b>CO<sub>2</sub> (vol%)</b>	15.33	15.56			15.56	
<b>Inlet gas temperature (°C)</b>	47.44	54			52	
<b>Initial solution mass (ton)</b>	30					
<b>Initial solution height (m)</b>		1.34	1.88		1.34	1.88
<b>Ca(OH)<sub>2</sub> (initial wt%)</b>	15	20	20			
<b>Initial temperature (°C)</b>	42	35	35		20	20

### 3.3 Model description

The proposed model consists of two sections; the flow model based on CFD and kinetic model based on DAEs.

#### 3.3.1 Governing equations

##### 3.3.1.1 Flow model

The three-phase system with gas, liquid, and solid was modeled with a gas–liquid two-phase model, where the physical properties of the liquid were modified to reflect the presence of solids. This is because the effect of presence of solid particles is reported to decrease to a negligible level at high gas flow rates [62]. It is also shown that the effect of solid particles becomes significant in a transition regime but trivial in a heterogeneous flow [44]. Hence, we ignored the presence of solids and adopted a gas-liquid two-phase model with modified physical properties [45]. In Eulerian-Eulerian approach, mass and momentum conservation equation with the interphase mass transfer is as follows:

$$\frac{\partial(\alpha_k \rho_k)}{\partial t} + \nabla \cdot (\alpha_k \rho_k \mathbf{u}_k) = -\dot{m}_{k \rightarrow l} \quad \text{Eq. 3-1}$$

$$\frac{\partial(\alpha_k \rho_k \mathbf{u}_k)}{\partial t} + \nabla \cdot (\alpha_k \rho_k \mathbf{u}_k \mathbf{u}_k) = \nabla \cdot (\alpha_k \mu_{eff} (\nabla \mathbf{u}_k + (\nabla \mathbf{u}_k)^T)) -$$

$$\alpha_k \nabla p_k + \mathbf{M}_k - \dot{m}_{k \rightarrow l} \mathbf{u}_k \quad \text{Eq. 3-2}$$

where  $\alpha$ ,  $\rho$ ,  $\mathbf{u}$ ,  $\mu_{\text{eff}}$ , and  $p$  are volume fraction, density, velocity, effective viscosity, and pressure, respectively, and  $k$  denotes the phase.  $\mathbf{M}_k$  is the interphase momentum exchange between the  $k$ -phase and all the other phases, and  $\dot{m}_{k \rightarrow l}$  refers to the mass transfer rate from phase  $k$  to  $l$ .

In regard to the interphase momentum exchange, only the gas ( $k=g$ ) and solution phase ( $k=m$ ) were considered since the solid were taken into account by modifying the physical properties of the liquid phase. Consequently,  $\mathbf{M}_m$  and  $\mathbf{M}_g$  were described as follow:

$$\mathbf{M}_m = -\mathbf{M}_g = \mathbf{M}_{m,D} + \mathbf{M}_{m,L} + \mathbf{M}_{m,VM} \quad \text{Eq. 3-3}$$

$$\mathbf{M}_{m,D} = \frac{3}{4} \alpha_g \rho_m \frac{C_D}{d_B} |\mathbf{u}_g - \mathbf{u}_m| (\mathbf{u}_g - \mathbf{u}_m) \quad \text{Eq. 3-4}$$

$$\mathbf{M}_{m,L} = \alpha_g \rho_m C_L (\mathbf{u}_g - \mathbf{u}_m) \times \nabla \times \mathbf{u}_m \quad \text{Eq. 3-5}$$

$$\mathbf{M}_{m,VM} = \alpha_g \rho_m C_{VM} \left( \frac{D_g \mathbf{u}_g}{Dt} - \frac{D_m \mathbf{u}_m}{Dt} \right) \quad \text{Eq. 3-6}$$

Where the subscripts D, L, and VM refer to drag, lift, and virtual mass force, respectively. The drag coefficient ( $C_D$ ), lift coefficient ( $C_L$ ), and virtual mass force coefficient ( $C_{VM}$ ) were set to 0.44, 0.5, and 0.25 in case of  $\alpha_g < 0.45$  and 0.05, 0, and 0 of  $\alpha_g > 0.45$ , respectively.

$\mu_{eff}$  is the effective viscosity, and defined as:

$$\mu_{eff} = \mu_m + \mu_{t,m} \quad \text{Eq. 3-7}$$

where  $\mu_m$  is the viscosity and  $\mu_{t,m}$  is the turbulence viscosity of the solution, which is calculated as

$$\mu_{t,m} = \rho_m C_\mu \frac{k_m^2}{\epsilon_m} \quad \text{Eq. 3-8}$$

A standard  $k - \epsilon$  model was used to obtain the turbulence kinetic energy ( $k_m$ ) and the energy dissipation rate ( $\epsilon_m$ ) of the solution. The governing equations are written below:

$$\begin{aligned} \frac{\partial}{\partial t} (\rho_m \alpha_m k_m) + \nabla \cdot \left( \alpha_m (\rho_m \mathbf{u}_m k_m - \left( \mu_m + \frac{\mu_{t,m}}{\sigma_k} \right) \nabla k_m) \right) = \\ \alpha_m (P_m - \rho_m \epsilon_m) \end{aligned} \quad \text{Eq.3-9}$$

$$\begin{aligned} \frac{\partial}{\partial t} (\rho_m \alpha_m \epsilon_m) + \nabla \cdot \left( \alpha_m \rho_m \mathbf{u}_m \epsilon_m - \left( \mu_m + \frac{\mu_{t,m}}{\sigma_\epsilon} \right) \nabla \epsilon_m \right) = \\ \alpha_m \frac{\epsilon_m}{k_m} (C_{1\epsilon} P_m - C_{2\epsilon} \rho_m \epsilon_m) \end{aligned} \quad \text{Eq. 3-10}$$

where the constants of the parameters  $C_\mu$ ,  $C_{1\epsilon}$ ,  $C_{2\epsilon}$ ,  $\sigma_k$ , and  $\sigma_\epsilon$  are 0.09, 1.44, 1.92, 1.0 and 1.3, respectively.  $P_m$  is the turbulence production due to buoyancy and viscous forces, and is described by:

$$P_m = \mu_{t,m} \nabla \mathbf{u}_m \cdot (\nabla \mathbf{u}_m + \nabla \mathbf{u}_m^T) - \frac{2}{3} \cdot \nabla \mathbf{u}_m (3\mu_{t,m} \nabla \cdot \mathbf{u}_m + \rho_m k_m)$$

Eq. 3-11

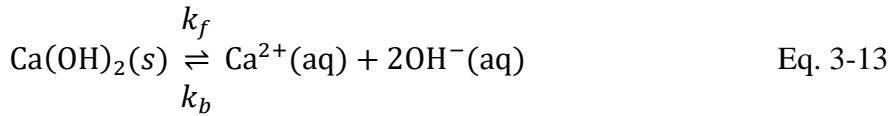
### 3.3.1.2 Kinetic model

The mineral carbonation consists of several reactions:

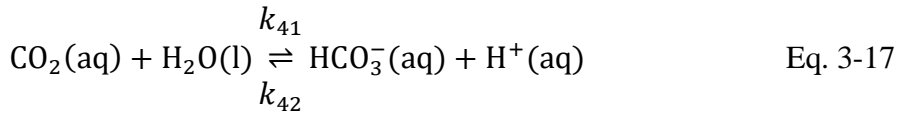
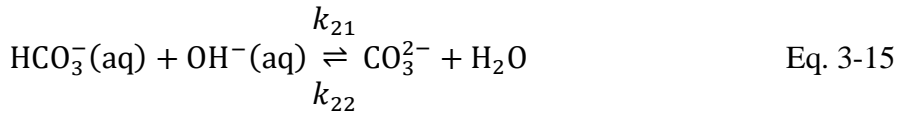
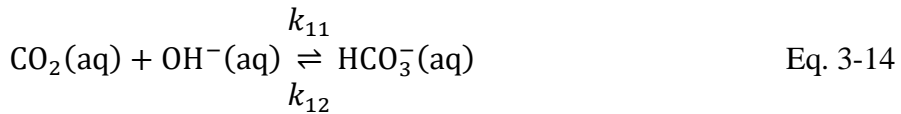
#### *Mass transfer of CO<sub>2</sub>(g)*



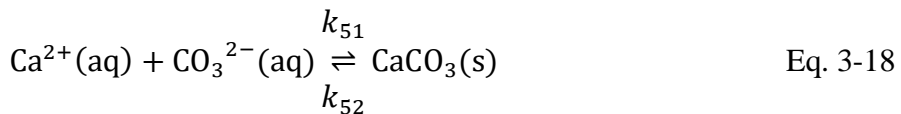
#### *Dissolution of Ca(OH)<sub>2</sub>*

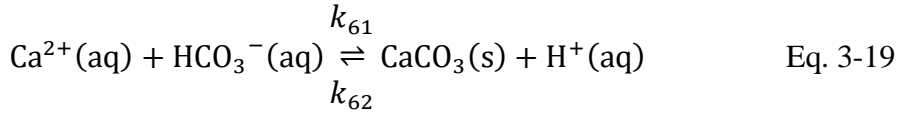


#### *Ionic reactions*



#### *Precipitation of CaCO<sub>3</sub>*





The pilot- and industrial-scale reactors are too large to assume homogeneous distributions of reactants, particularly of the CO<sub>2</sub> gas. Therefore, the reactor volume was divided into hundreds of zones and a mass balance equation for each zone with respect to CO<sub>2</sub>(g) was set. In all zones, the concentrations of the solids and ions were assumed to have the same values in all zones because the solid and ion particles are small enough to make Stokes flow with circulating liquid streams.

Since the volume fraction of N<sub>2</sub> in the inlet gas was about 85-90 %, the hydrodynamics between the entire gas and solution did not change much even if CO<sub>2</sub> was removed from chemical reactions. This was validated by a comparison of the hydrodynamics between the CFD-absorption model and the CFD-hydrodynamics model.

The connections between zones are depicted in Figure 3-2. The exact mass balance equation at zone *i* can be written as

$$\frac{dm_{\text{CO}_2(g)}^i}{dt} = \sum_{j \neq i}^N F_{j,i} \frac{m_{\text{CO}_2(g)}^j}{m_{\text{CO}_2(g)}^j(0)} - F_{i,i} \frac{m_{\text{CO}_2(g)}^i}{m_{\text{CO}_2(g)}^i(0)} - \dot{m}_{g \rightarrow l}^i \quad \text{Eq. 3-20}$$

where  $m_{\text{CO}_2(g)}^i$  is the mass of CO<sub>2</sub> gas in zone *i*,  $m_{\text{CO}_2(g)}^i(0)$  is the

initial value of  $m_{\text{CO}_2(g)}^i$ ,  $N$  is the total number of zones,  $\dot{m}_{g \rightarrow l}^i$  is the  $\text{CO}_2$  mass transfer rate from the gas phase to the liquid phase, and  $F_{i,j}$  and  $F_{i,i}$  are from the transition rate matrix defined as

$$\begin{bmatrix} F_{1,1} & F_{1,2} & \cdots & F_{1,N} \\ \vdots & \vdots & \ddots & \vdots \\ F_{N,1} & F_{N,2} & \cdots & F_{N,N} \\ F_{inlet,1} & F_{inlet,2} & \cdots & F_{inlet,N} \end{bmatrix}. \quad \text{Eq. 3-21}$$

The transition rate matrix consists of  $F_{i,j}$ , which is the  $\text{CO}_2$  mass flowrate from zone  $i$  to zone  $j$ .  $F_{i,i}$  is the  $\text{CO}_2$  mass outflow from zone  $i$ , and  $F_{inlet,i}$  is the inlet mass flow rate from the sparger to zone  $i$ . All the components in the transition matrix besides  $F_{i,i}$  (diagonal components) were imported from the CFD-hydrodynamics model. However,  $F_{i,i}$  was directly adopt in the CFD result; to ensure mass conservation,  $F_{i,i}$  was fixed to  $-\sum_{j \neq i}^N F_{i,j}$  at each zone because even a slight violation of the mass conservation can cause a convergence problem in subsequent steps.

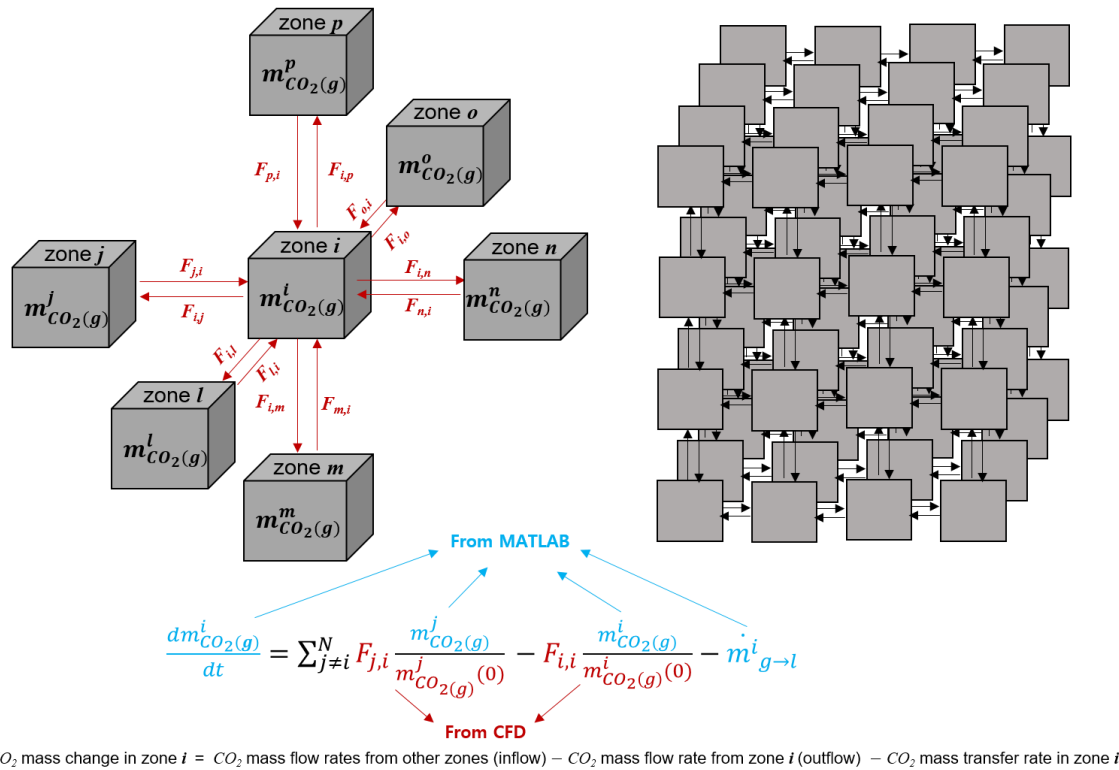


**Figure 3-2. Systematic diagram for the CFD-based compartmental model.**

In Eq. 3-20,  $F_{j,i}$  and  $F_{i,i}$  were multiplied by  $\frac{m_{CO_2}^j}{m_{CO_2}^j(0)}$  and  $\frac{m_{CO_2}^i}{m_{CO_2}^i(0)}$ , respectively. Because the CFD-hydrodynamics model did not include the reactions, the transition rate matrix could not represent the mass flowrate at any given time; it rather simply provided the initial flow rates. Therefore, the CO<sub>2</sub> mass flow rate from  $j$  to  $i$  at time  $t$ ,  $F_{j,i}(t)$ , was calculated with the constraint of  $F_{j,i}(t):F_{j,i}(0) = m_{CO_2}^j(t):m_{CO_2}^j(0)$  to update the flow rates at every time step.

The CO<sub>2</sub> mass transfer rate,  $\dot{m}_{g \rightarrow l}^i$ , in Eq. 3-20 is described as:

$$\dot{m}_{g \rightarrow l}^i = k_L a E \left( H^{CO_2} \frac{m_{CO_2}^i(g)}{MW_{CO_2} \cdot V_{gas}^i} - [CO_2(aq)] \right) \cdot MW_{CO_2} \quad \text{Eq. 3-22}$$

where  $k_L$  is the overall CO<sub>2</sub> mass transfer coefficient,  $a$  is the interfacial area per unit volume,  $E$  is the enhancement factor to consider chemical mass transfer,  $H^{CO_2}$  is Henry's constant for the electrolyte solution,  $MW_{CO_2}$  is the molecular weight of CO<sub>2</sub>,  $V_{gas}^i$  is the volume of gas at zone  $i$  obtained from CFD result, and  $[CO_2(aq)]$  is the molar concentration of CO<sub>2</sub>(aq). The experimental or physical correlations in Section 2.3.2 are used to obtain the values for  $k_L$ ,  $a$ ,  $E$ , and  $H^{CO_2}$ . Because some of these correlations include the Reynolds number and slip velocity is required to calculate the Reynolds number,

the average solution velocity  $u$ ,  $w$ ,  $v$  and  $\text{CO}_2$  velocity  $u$ ,  $w$ ,  $v$  in each zone were obtained from the CFD-hydrodynamics model.

To represent the entire homogeneous reactor space, a mass balance equation for each of them was developed for the rest of the chemical species involved in the system. Because there are no inlet and outlet streams for the liquid and solid, these equations did not include any flow rate terms.

$$\frac{d[\text{CO}_2(\text{aq})]}{dt} = -k_{11}[\text{CO}_2(\text{aq})][\text{OH}^-] + k_{12}[\text{HCO}_3^-] - k_{41}[\text{CO}_2(\text{aq})] + k_{42}[\text{HCO}_3^-][\text{H}^+] + \frac{1}{MW_{\text{CO}_2} \cdot V_{\text{liq}}} \sum_{i=1}^N \dot{m}_{g \rightarrow l}^i \quad \text{Eq. 3-23}$$

$$\begin{aligned} \frac{d[\text{HCO}_3^-]}{dt} = & k_{11}[\text{CO}_2(\text{aq})][\text{OH}^-] - k_{12}[\text{HCO}_3^-] - k_{21}[\text{HCO}_3^-][\text{OH}^-] + \\ & k_{22}[\text{CO}_3^{2-}] + k_{41}[\text{CO}_2(\text{aq})] - k_{42}[\text{HCO}_3^-][\text{H}^+] - \\ & k_{61}[\text{Ca}^{2+}][\text{HCO}_3^-] + k_{62}[\text{H}^+] \end{aligned} \quad \text{Eq. 3-24}$$

$$\frac{d[\text{CO}_3^{2-}]}{dt} = k_{21}[\text{HCO}_3^-][\text{OH}^-] - k_{22}[\text{CO}_3^{2-}] - k_{51}[\text{Ca}^{2+}][\text{CO}_3^{2-}] + k_{52}$$

Eq. 3-25

$$\begin{aligned} \frac{d[\text{OH}^-]}{dt} = & -k_{11}[\text{CO}_2(\text{aq})][\text{OH}^-] + k_{12}[\text{HCO}_3^-] - \\ & k_{21}[\text{HCO}_3^-][\text{OH}^-] + k_{22}[\text{CO}_3^{2-}] - k_{31}[\text{OH}^-][\text{H}^+] + 2A_s(k_f - \\ & k_b[\text{Ca}^{2+}]f^2[\text{OH}^-]^2f^4) \end{aligned} \quad \text{Eq. 3-26}$$

$$\frac{d[H^+]}{dt} = -k_{31}[OH^-][H^+] + k_{32} - k_{42}[HCO_3^-][H^+] + k_{41}[CO_2(aq)] + k_{61}[Ca^{2+}][HCO_3^-] - k_{62}[H^+] \quad \text{Eq. 3-27}$$

$$\frac{d[Ca^{2+}]}{dt} = -k_{51}[Ca^{2+}][CO_3^{2-}] + k_{52} - k_{61}[Ca^{2+}][HCO_3^-] + k_{62}[H^+] + A_s(k_f - k_b[Ca^{2+}]f^2[OH^-]^2f^4) \quad \text{Eq. 3-28}$$

$$\frac{d[CaCO_3]}{dt} = k_{51}[Ca^{2+}][CO_3^{2-}] - k_{52} + k_{61}[Ca^{2+}][HCO_3^-] - k_{62}[H^+] \quad \text{Eq. 3-29}$$

In Eq. 3-23,  $V_{liq}$  is the liquid volume of the reactor. In Eqs. 3-26 and 3-28,  $A_s$  and  $f$  are the total surface area of  $Ca(OH)_2$  and activity coefficient of the solution, respectively. The term  $A_s$  was devised to decrease with the consumption of  $Ca(OH)_2$ . The correlations or values for all the rate constants were obtained from the literature and applied in the model.

It is important to predict the temperature with a low error because several rate constants and terms in the mass transfer rate are functions of the temperature. A heat balance equation for the reactor follows as:

$$\frac{dT_{reactor}}{dt} = \frac{H_{in} - H_{out} - H_{water\ evaporation} + H_{reaction}}{C_{reactants}} \quad \text{Eq. 3-30}$$

where  $T_{reactor}$  is the reactor temperature,  $H_{in}$  and  $H_{out}$  are the inlet and outlet enthalpies, respectively,  $H_{water\ evaporation}$  is the latent

heat by the water vaporization due to the temperature difference between the inlet and outlet,  $H_{reaction}$  is the heat of the net chemical reactions, and  $C_{reactants}$  is the sum of the heat capacities of all the reactants; these variables can be expressed as:

$$H_{in} = \sum_{X=N_2,CO_2,H_2O} n_{X,inlet} \cdot H_{m,X}(T_{inlet\ gas}) \quad \text{Eq. 3-31}$$

$$H_{out} = \sum_{X=N_2,CO_2,H_2O} n_{X,outlet} \cdot H_{m,X}(T_{reactor}) \quad \text{Eq. 3-32}$$

$$H_{water\ evaporation} = (n_{H_2O,outlet} - n_{H_2O,inlet}) \cdot$$

$$\Delta H_{m,water\ evaporation} \quad \text{Eq. 3-33}$$

$$C_{reactants} = m_{H_2O} \cdot c_{H_2O} + m_{Ca(OH)_2} \cdot c_{Ca(OH)_2} + m_{CaCO_3} \cdot c_{CaCO_3}$$

Eq. 3-34

where  $n_X$ ,  $H_{m,X}(T)$  denote the moles of  $X$  in the stream, and the molar enthalpy of  $X$  at temperature  $T$ , respectively, and  $\Delta H_{m,water\ evaporation}$  is the molar latent heat of water, 40.66 kJ/mol, and  $H_{reaction}$  is  $\Delta H_{m,reaction} \cdot \frac{d[CaCO_3]}{dt} \cdot V_{liq}$ ;  $\Delta H_{m,reaction}$  is the heat of the net reaction of Eq. 3-12 to 3-19 with a value of 113.1 kJ/mol.

To calculate  $C_{reactants}$ , three equations were used as:

$$m_{H_2O} = \frac{V_{liq}}{\rho_{H_2O}} \quad \text{Eq. 3-35}$$

$$m_{\text{Ca(OH)}_2} = m_{\text{Ca(OH)}_2, \text{initial}} - ([\text{Ca}^{2+}] + [\text{CaCO}_3]) \cdot V_{liq} \cdot$$

$$MW_{\text{Ca(OH)}_2} \quad \text{Eq. 3-36}$$

$$m_{\text{CaCO}_3} = V_{liq} [\text{CaCO}_3] \quad \text{Eq. 3-37}$$

For the heat capacities,  $c_{\text{H}_2\text{O}}$  and  $c_{\text{CaCO}_3}$  were set to 4.18 and 0.8343 J/g/K, respectively. Unlike the heat capacity of  $\text{CaCO}_3$  and water where constant values were used, a correlation was derived for the heat capacity of  $\text{Ca(OH)}_2$  because of its temperature-dependency. An 8th order polynomial model was used to substitute temperature-solid Cp tabular data from Aspen plus's ELEC-NRTL model. When calculating  $H_{in}$  and  $H_{out}$ ,  $n_{\text{N}_2, \text{inlet}}$  and  $n_{\text{CO}_2, \text{inlet}}$  were determined from the experimental setup. The quantities of water in the inlet and outlet streams were determined according to the maximum moisture content allowed for air at a given temperature,  $\theta_{w, \text{max}}(T)$ :  $n_{\text{H}_2\text{O}} = (n_{\text{N}_2} + n_{\text{CO}_2}) \cdot \theta_{w, \text{max}}(T)$ . For  $H_{m, X}(T)$  and  $\theta_{w, \text{max}}(T)$ , we regressed the data table of the ideal gas properties.

### 3.3.2 Numerical setup

The numerical simulations were carried out using the ANSYS CFX 18.2 (Ansys., USA). The geometry and meshing were generated with

the DesignModular and AnsysMeshing modules. The simulations were performed in a platform of Intel Xeon E5-2690 (24 cores) with 128 GB of RAM. Navier-Stokes equations were discretized by using the hybrid finite volume and finite element approach in ANSYS CFX 18.2. Tetrahedral meshes were used for each of the reactors. As the number of computational nodes increased, only the gas holdup changed within 1-6 % (See Figure 3-3). For this reason, 265,439 and 704,442 were used as the number of computational nodes for the pilot- and industrial-scale reactors, respectively.

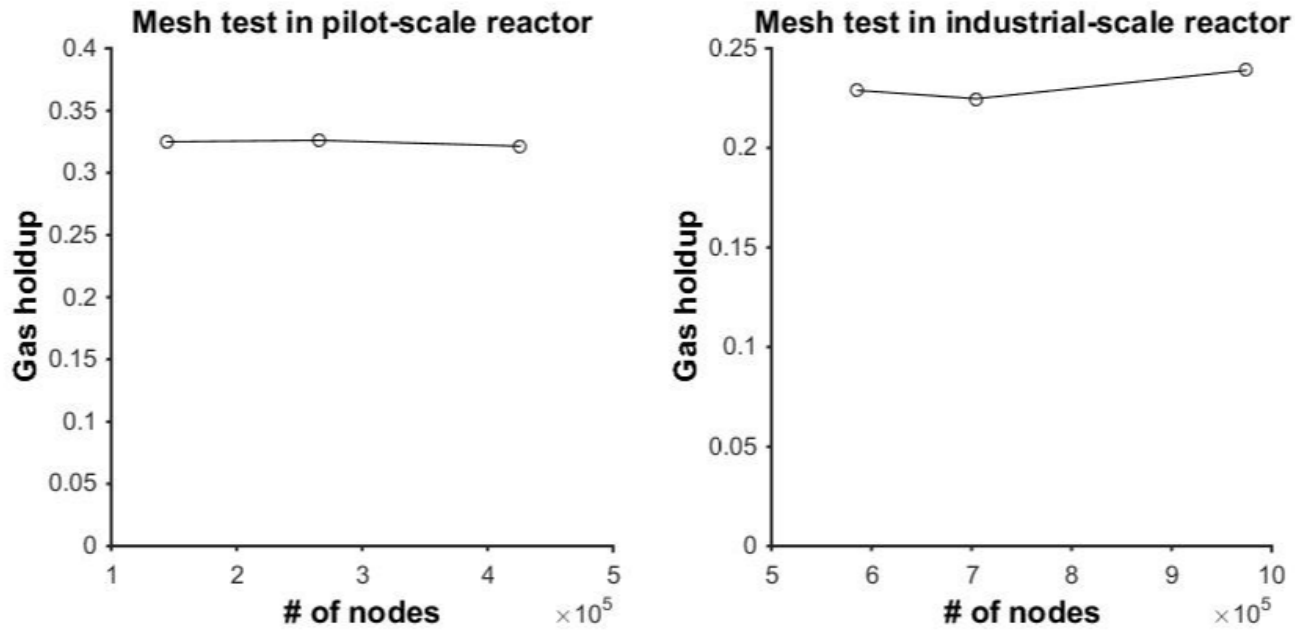


Figure 3-3. Mesh test in pilot-scale (left) and industrial-scale (right) reactors.

For the wall boundary condition, free-slip and no-slip conditions were selected for the gas and solution phases, respectively. The outlet condition was set as the de-gassing condition, under which only the gas can be discharged. For the inlet condition, to prevent the computational cost from increasing by simulating the full geometry of the sparger, the holes in the nozzles were ignored and a uniform inlet condition was given at the nozzle surface. All the impellers were 4-pitched blade types and their rotations were simulated using a multiple reference frame (MRF) method.

A high resolution was selected for the advection scheme. In the steady-state model, a high resolution was used for the turbulence numerics, and the convergence criterion of  $10^{-3}$  with 1500 iterations and 0.01 s physical timescale was used. The mass flow rate and CO<sub>2</sub> volume fraction from the steady-state CFD model were used in the CFD-based compartment model. The robust convergence criterion such as  $10^{-4}$  was not used because this CFD result is only for the initial conditions. Based on our analysis, the final results were independent of 10–20% fluctuations in these initial values. For the CFD-absorption model, which was used as a reference to compare the CFD-based compartmental model, the second-order backward Euler was used for

the transient scheme. The convergence loops were within a range of 1–5, and the convergence criterion of  $10^{-4}$  with a timestep of 0.01 s for 15 s was set.

While obtaining the CO<sub>2</sub> mass transfer rates from the CFD-absorption model and the CFD-based compartmental model, the gas cap region was not considered because it was assumed that the CO<sub>2</sub> mass transfer can be accomplished in the region where the aqueous solution and gas coexist. In the CFD-absorption model, this is the region where the gas holdup is less than 0.8. However, in the CFD-based compartmental model, the zones near the liquid surface contain both the regions with the gas holdup less and larger than 0.8 because the compartments cannot accurately separate the curved surface of the liquid. The solution was that the reactor first was divided into a number of angled zones, and then the zones located near the surface in the CFD simulation were reset to only include the cells whose gas holdup is less than 0.8.

For the kinetic model, MATLAB with Sundials IDAS solver was used. Particularly, dense linear solver with the relative tolerance  $10^{-7}$  and zero-crossing root algorithm were employed.

### 3.3.3 Zoning method

The reactor was manually divided into zones after the hydrodynamics results were obtained. First the CFD-hydrodynamics model without dividing the zones was obtained, and then well-mixed zones were identified and grouped together. Although an automatic zoning method has been studied, a manual dividing method was used in this study because there is no conclusive proof that automatic zoning is better than the manual one [63, 64].

As shown in Figure 3-4 (left), the CO<sub>2</sub> holdup profile varies along the radial and angle at the same height for the pilot-scale reactor. Consequently, the reactor was divided along the height, angle, and radial direction until the number of zones could no longer affect the results (see Figure 3-4 (middle and right)).

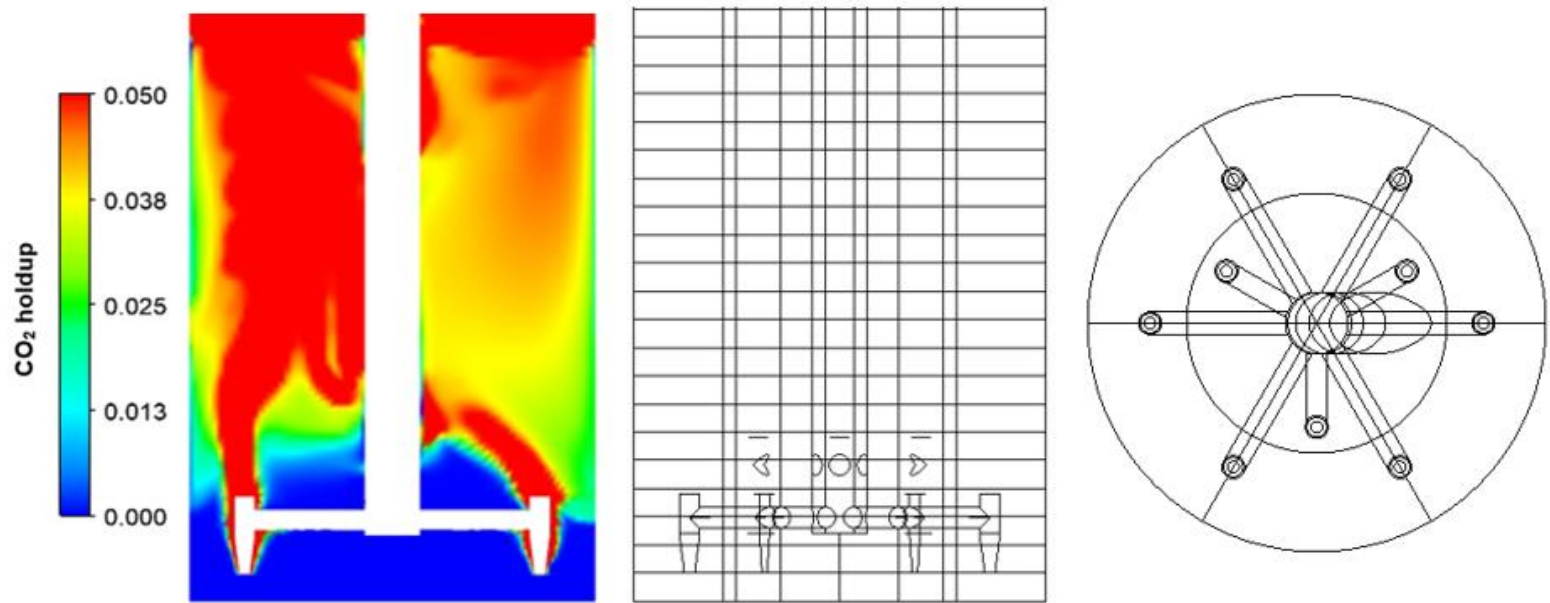


**Figure 3-4. CO<sub>2</sub> holdup profiles obtained from the CFD-hydrodynamics model (left), and side and top view (middle and right) of the divided pilot-scale reactor configuration.**

## **3.4 Results and discussion**

### **3.4.1 Compartmental model for pilot-scale reactor (limitation of compartmental model)**

In this section, a comparison between the CFD-based compartmental model and the compartmental model is presented, and the importance of the flow of information such as the initial CO<sub>2</sub> holdup and relative velocity are highlighted. First, the pilot-scale reactor was simulated using the compartmental model for the Experiment P-1 1st reactor condition. The reactor volume was divided into 20 zones in the direction of height, i.e., vertically. It was not divided in the horizontal direction because there is a limitation to predict the mass flow rate of CO<sub>2</sub> in the horizontal direction considering the impeller power, buoyancy force, and complex sparger configuration. However, the initial CO<sub>2</sub> holdup was assumed to range from 0.02 to 0.05 and the relative velocity between the gas and solution phases to obtain the Reynolds number was assumed to be 0.3–3 m/s. Because the compartmental model cannot predict initial values at all, we set the ranges based on the information from the CFD-hydrodynamics model (the average initial CO<sub>2</sub> holdup of 0.032 and average relative velocity of 0.5 m/s).

The amount of mass-transferred CO<sub>2</sub> was 7.9–13.5 ton/day as the initial CO<sub>2</sub> holdup varied; the error was caused by the enhancement factor ranged from 1.43 to 8.64 as the relative velocity varied. The results confirmed that flow information such as the initial CO<sub>2</sub> holdup and relative velocity, which can be obtained from CFD, are important factors for accurate simulations.

The initial CO<sub>2</sub> holdup, relative velocity of each zones, and the mass flow rate of CO<sub>2</sub> between zones obtained from the CFD-hydrodynamics model were used in the CFD-based compartmental model with 20 zones. With these values, the amount of mass-transferred CO<sub>2</sub> was calculated to be 12.7 tonnes/day. The CO<sub>2</sub> holdup profile of the model is shown in Figure 3-5; only the aqueous solution region is shown because there is no CO<sub>2</sub> mass transfer in the gas cap region. Compared with Figure 3-9 (right), where the CO<sub>2</sub> holdup was obtained using the CFD-absorption model, it was confirmed that the 20-zone model can show similar results for the vertical direction, though insufficient results for the horizontal direction. As a result, the potential of the proposed modeling approach and the need to increase the number of zones, particularly in the horizontal direction, were identified. To sum up, the compartmental model can be used to obtain

only the qualitative information on the effect of  $pH$ , temperature, and other process variables. The CFD-hydrodynamics model is essential to obtain the initial  $CO_2$  holdup, relative velocity of each zones, and mass flow rate of  $CO_2$  between zones. The use of the CFD-hydrodynamics model becomes important if the horizontal direction zones are considered. This is because the compartmental model has a limitation on the prediction of the mass flow rate of  $CO_2$  considering the impeller power, buoyance force, and complex sparger configuration.

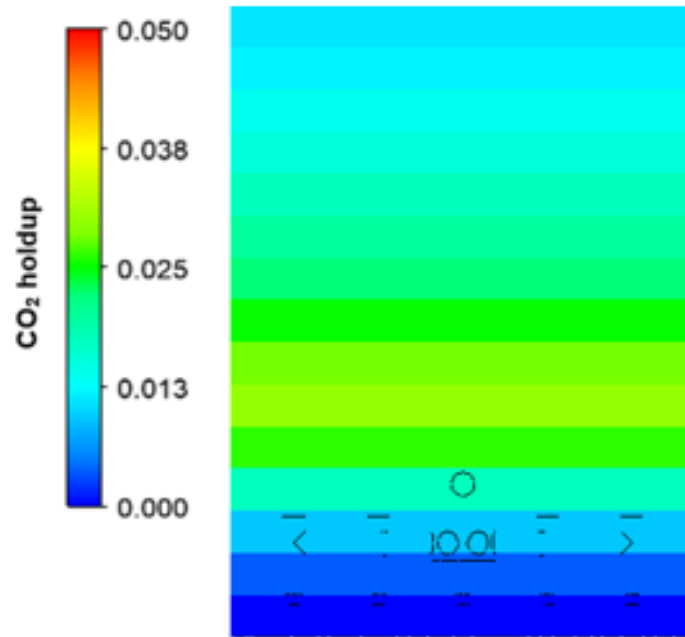


**Figure 3-5. CO<sub>2</sub> holdup profile of the CFD-based compartmental model in 20-zone model in Experiment P-1 of 1st reactor.**

### 3.4.2 CFD-based compartmental model for the pilot-scale reactor.

Because enough information about the operational changes during the experiments were not secured, it was assumed that temperature and pH conditions had constant values in the model; according to the literature, the reactor showed a steady behavior except for the initial and end stages. For the calculation of mass-transferred CO<sub>2</sub>, we solved Eq. 3-22, which is regarded as the rate-determining step in abundance of Ca(OH)<sub>2</sub>.

In order to determine the appropriate number of zones, the number of zones was increased until the CFD-based compartmental model gave the results with acceptable accuracy in terms of CO<sub>2</sub> holdup profiles and the sum of CO<sub>2</sub> removal rate along height, i.e.,  $\int_{H_{ith\ floor}}^{H_{(i+1)th\ floor}} (CO_2\ removal\ rate) * dH$ . The reactor was divided along the height, angle, and radial directions, and finally the 20 (20×1×1)-, 60 (15×2×2)-, 163 (27×1×6+1)-, 324 (27×2×6)-zone models were designed (See Figure 3-6). In the 163-zone model, an extra one-zone was made when the top part of the reactor with gas pipeline was divided along the angular direction. In the 20-zone model, the reactor was divided only along the height.

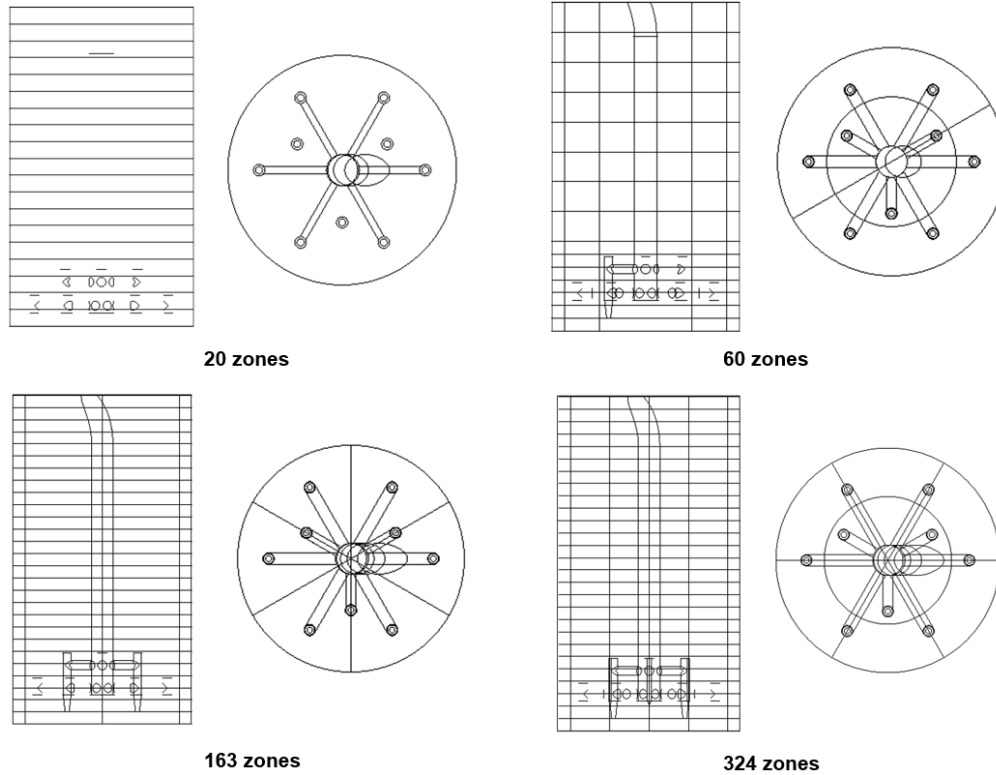


**Figure 3-6. Side and top views of the 20-, 60-, 163-, and 324-zone models in the pilot-scale reactor.**

As shown in Figure 3-7, there were significant errors in the 20- and 60-zone model. The reason why the two model have large error can be explained through the CO<sub>2</sub> holdup profiles in Figures 3-5 and 8 (left). Because 20-zone model was only divided along the height, 20-zone model cannot give asymmetrical results along the angular and radial directions, making erroneous results in all sections. In the 60-zone model, although the reactor was divided along the angular and radial direction, CO<sub>2</sub> holdup profiles shown in Figures 3-5 and 9 (left) have a big difference due to lack of the number of zones. On the other hand, if the number of zones is larger than 163, the increasing number of zones does not further improve the prediction performance along the height (See Figure 3-7). However, in Figures 3- 8 & 9, the 324-zone model shows more similar CO<sub>2</sub> holdup profile for the comparison with the CFD-absorption model than the 163-zone model. In conclusion, the 324-zone model was chosen for further analysis because it provides more detailed results along the angular and radial direction although the 163-zone model shows reliable results along the height. The CO<sub>2</sub> holdup profile of the CFD-absorption model was discretized from the original continuous profile for comparison. Figure 3-10 shows how the CO<sub>2</sub> holdup profiles change after solving

the ordinary differential equation from the CFD-hydrodynamics model as well as the profiles from the CFD-absorption model in Experiments P-1 and P-2. When the CFD-based compartmental model was compared with the CFD-absorption model, similar CO<sub>2</sub> holdup profiles were observed for all the cases. In Figure 3-11, the CO<sub>2</sub> removal efficiencies of the experiments, the CFD-based compartmental model, and the CFD-absorption model are compared. The errors of the CFD-based compartmental model results are less than 7% when compared with the experiments and the CFD-absorption model.

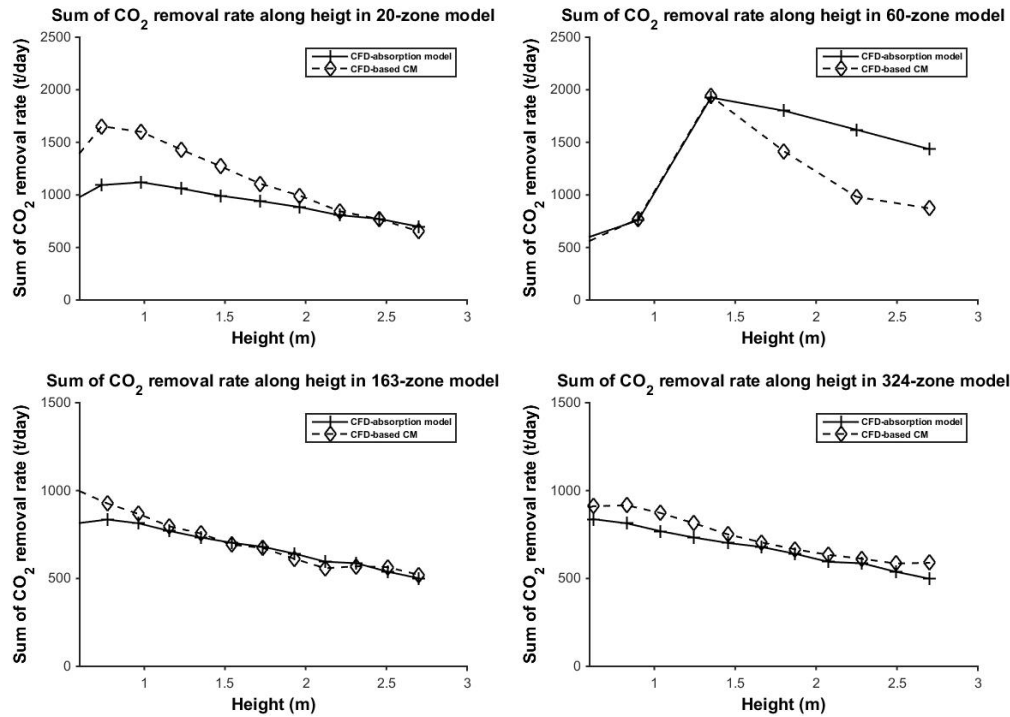


**Figure 3-7. Sum of CO<sub>2</sub> removal rate along the height in 20-, 60-, 163-, and 324-zone models in Experiment P-1 of 1st reactor.**

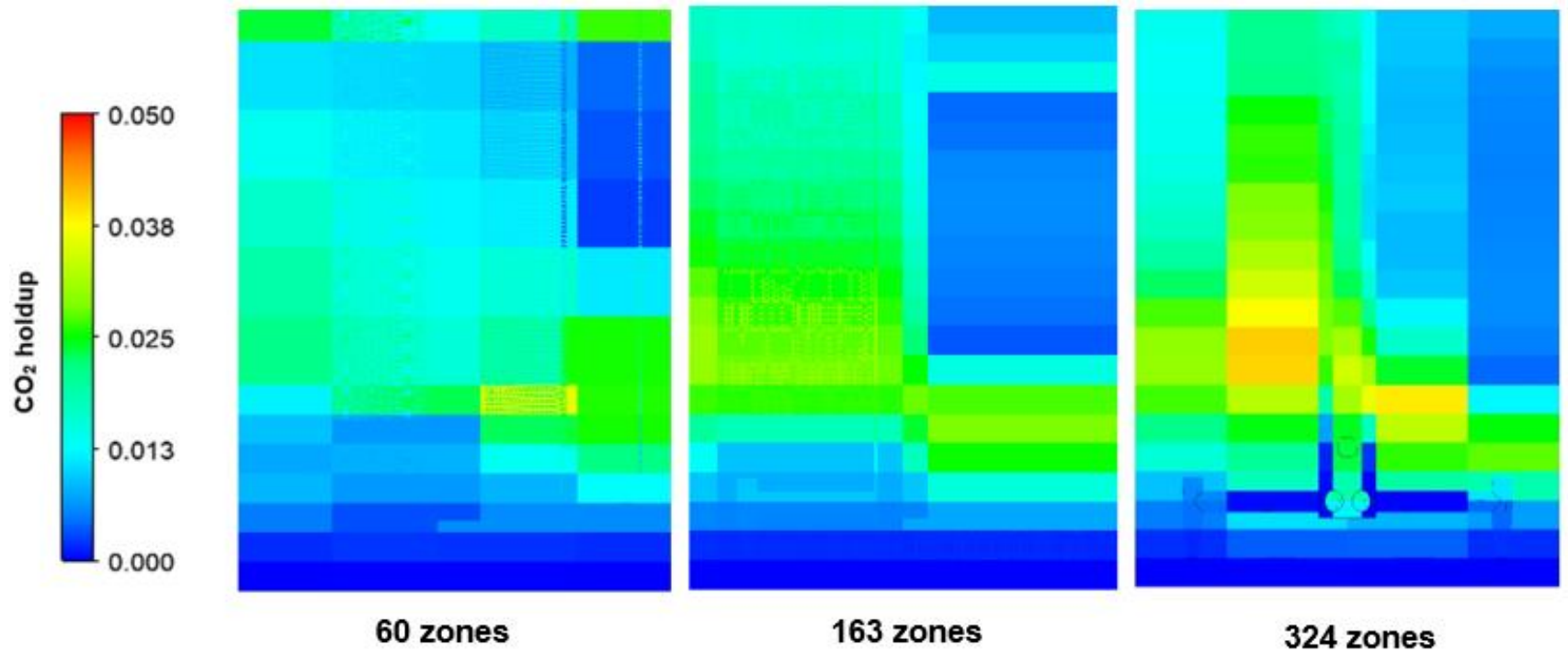


**Figure 3-8. CO<sub>2</sub> holdup profiles of the CFD-based compartmental model in 60-zone (left), 163-zone (middle), and 324-zone (right) models in Experiment P-1 of 1st reactor.**

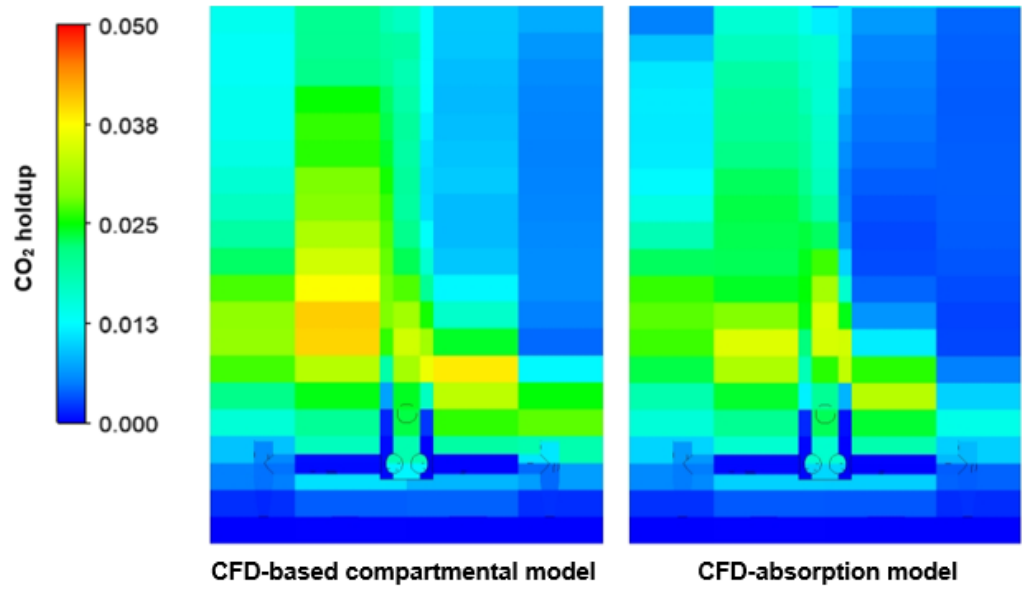


**Figure 3-9. CO<sub>2</sub> holdup profiles of the CFD-based compartmental model with 324-zone (left) and CFD-absorption model (right) models in Experiment P-1 of 1st reactor.**

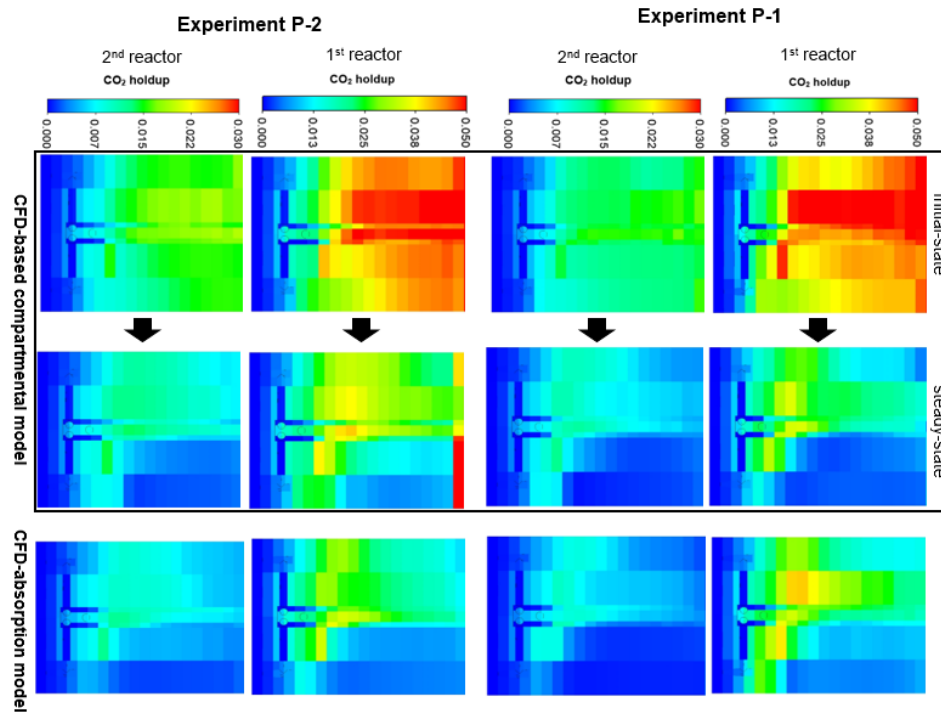


**Figure 3-10. CO<sub>2</sub> holdup profiles of the CFD-based compartmental model and CFD-absorption model in Experiments P-1 and P-2.**

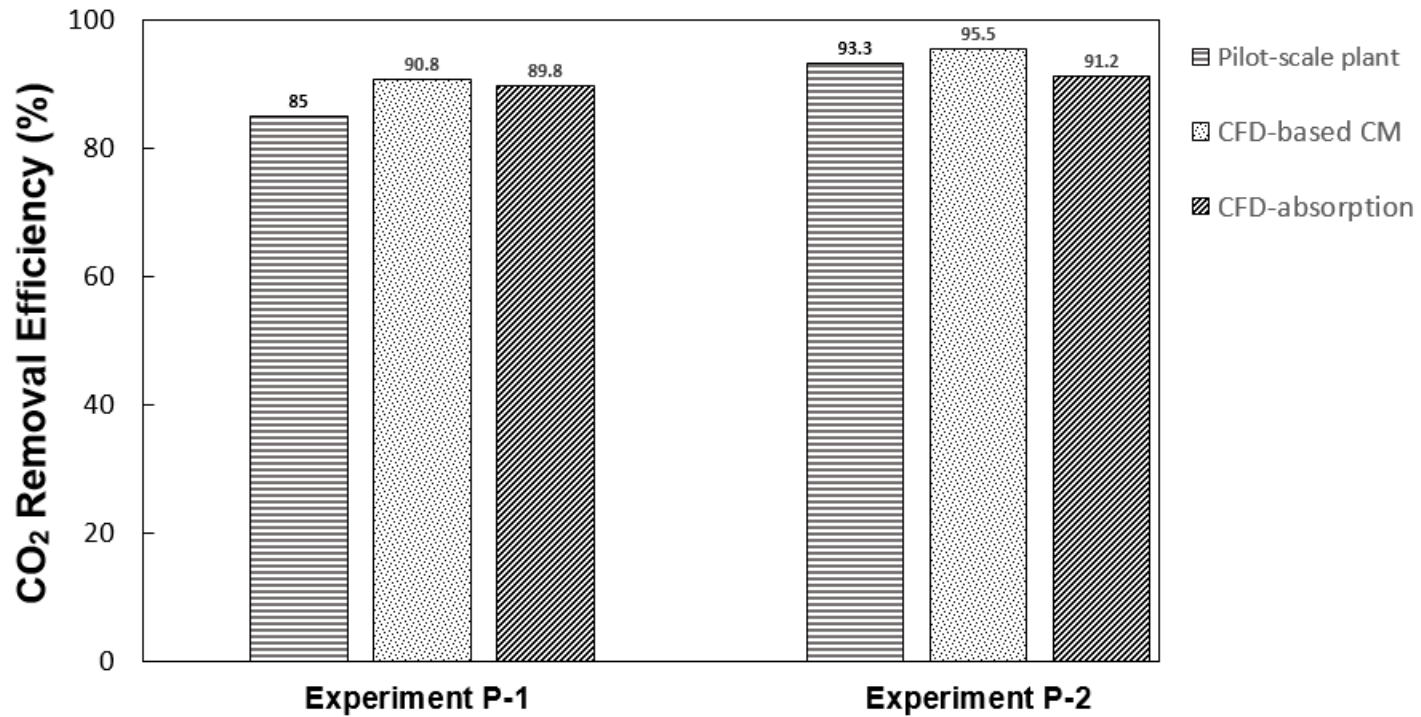


**Figure 3-11. Comparisons of the CO<sub>2</sub> removal efficiencies derived from experiments, CFD-based compartmental model, and CFD-absorption model in the pilot-scale process.**

### **3.4.3 CFD-based compartmental model for the industrial-scale reactor.**

The CFD-based compartmental model with the full kinetics was applied to the industrial-scale reactor. To decide the sufficient number of zones in the industrial-scale reactor, the spatial distribution of CO<sub>2</sub> holdup was first compared at steady-state as for the pilot-scale reactor. Figure 3-12 shows that there is no more significant difference in the CO<sub>2</sub> holdup profile from 179 zones. The dynamic behaviors were also compared. The results are shown in Figure 3-13. It is confirmed that 179-zone model shows no difference with 291-zone model as well as the plant data. Thus, it is possible to conclude that the addition of extra zones more than 179 is not necessary but just increases the computational time. The configuration of 179-zone model is shown in Figure 3-14.

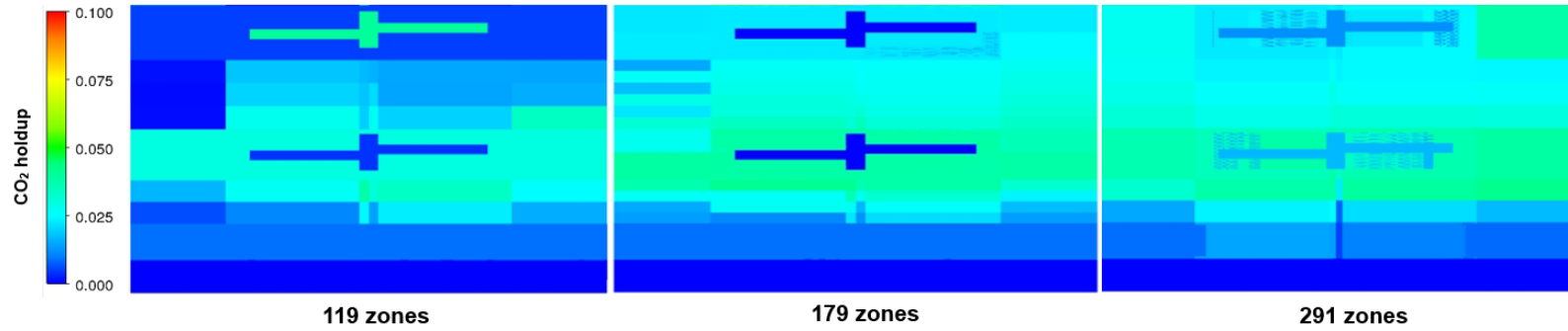


**Figure 3-12. CO<sub>2</sub> holdup profiles of the CFD-based compartmental model in 119-zone (left), 179-zone (middle), and 291-zone (right) models in Experiment I-2 2nd reactor.**

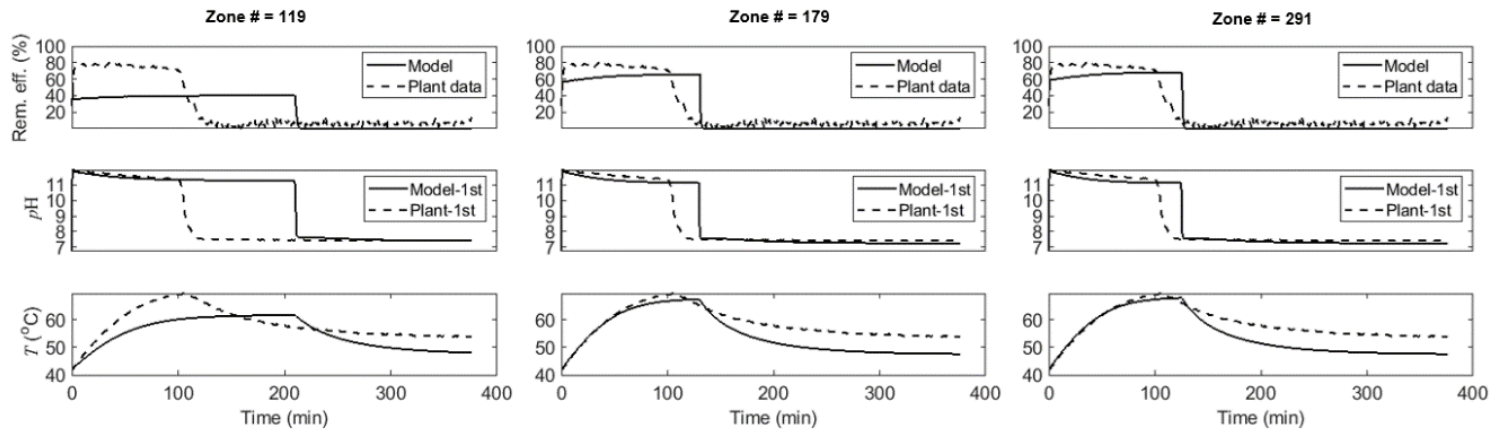


**Figure 3-13. Robustness test of zone numbers by comparison of model results with operation data in Experiment I-1.**

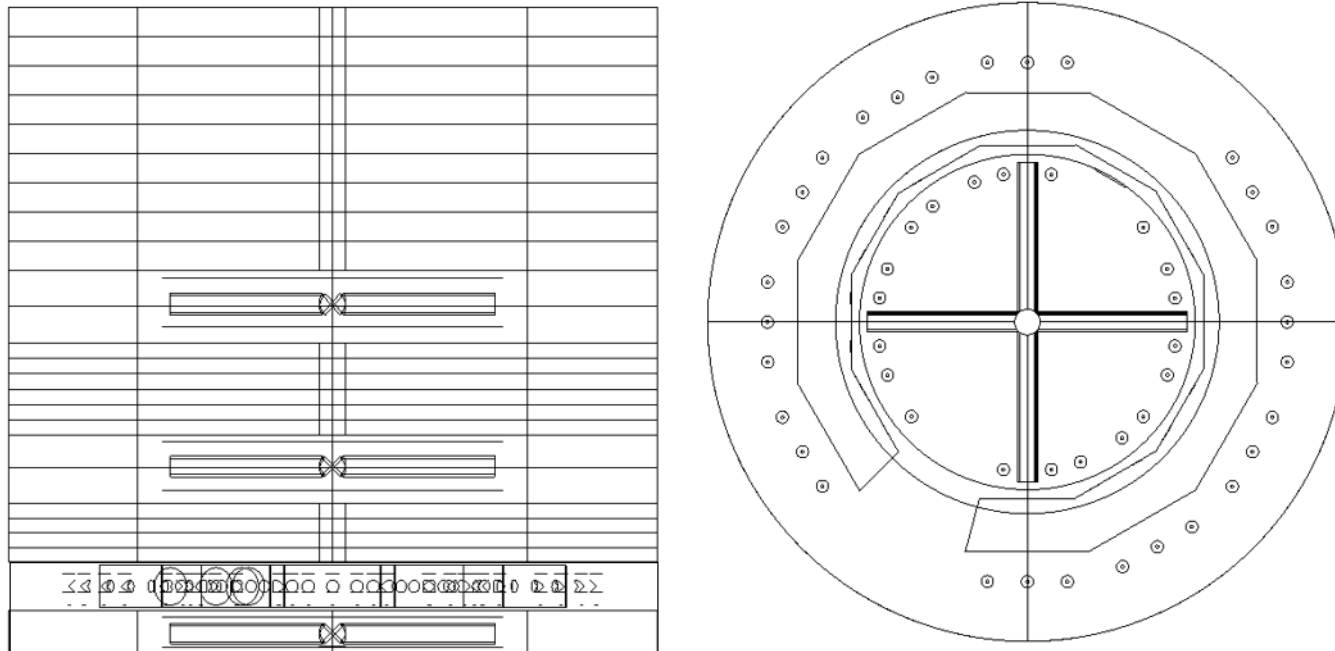


**Figure 3-14. Side and top views of the 179-zone model in the industrial-scale reactor.**

On the other hand, it is reckoned that the reason for the industrial-scale reactor being sufficiently modeled with less number of zones than the pilot-scale reactor is in its symmetrical structure. In the pilot-scale reactor, the sparger configuration is asymmetrical and the inlet pipe takes more portion of space in terms of the reactor size. Hence, the reactor must be divided more finely both in angle and radial directions. Although the 163-zone model showed reliable results in the pilot-scale reactor along the height, the 324-zone model provides more detailed result along the angle and radial directions.

Two sets of data from the test operations performed at the Incheon plant were obtained. The data include time series measurements of the overall CO<sub>2</sub> removal efficiency and *pH* and temperature values of each reactor. Figure 3-15 shows the model prediction performance from the initial states until all Ca(OH)<sub>2</sub> is consumed.

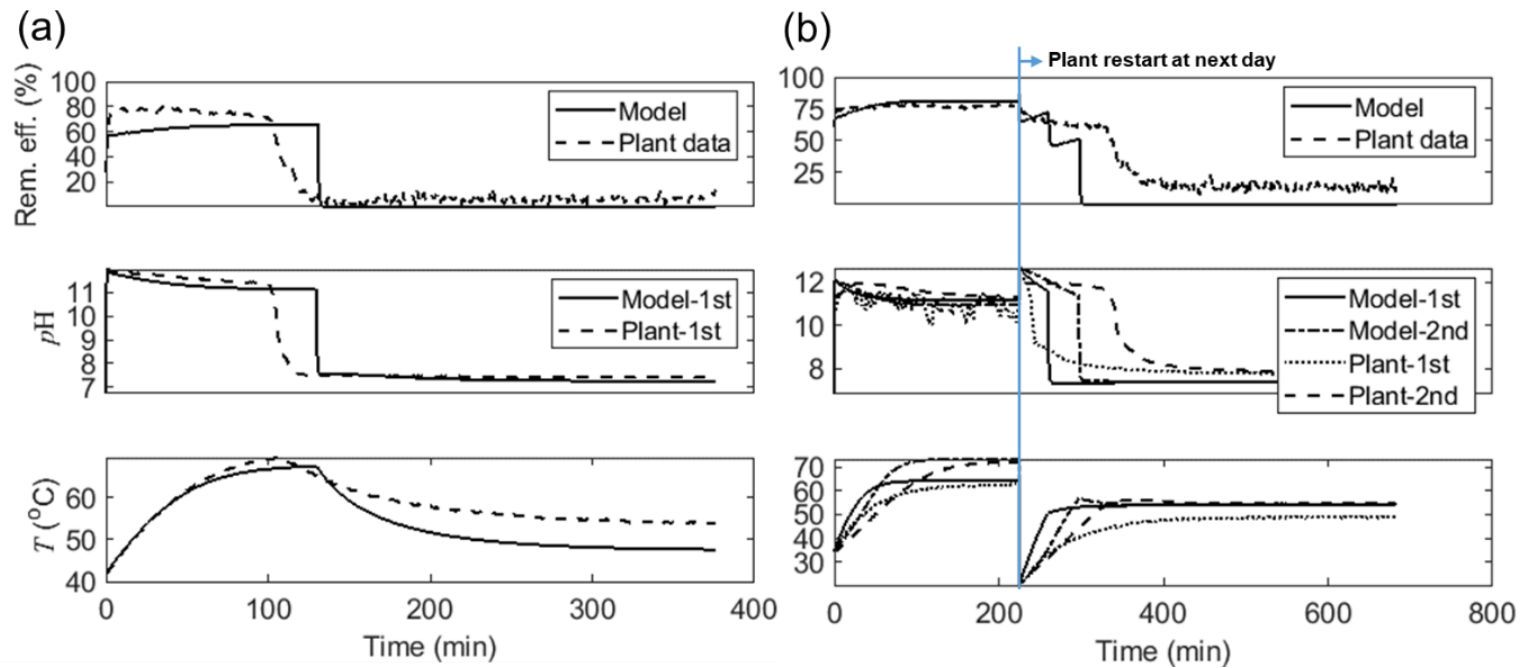


**Figure 3-15. Model results compared with operation data from (a) Experiment I-1 and (b) Experiment I-2**

One cycle of batch process started with reactors fully charged with  $\text{Ca(OH)}_2$  to keep a high level of  $p\text{H}$  until the majority of  $\text{Ca(OH)}_2$  was reacted. Because the net reaction is exothermic and the inlet gas temperature (usually around  $50\text{ }^\circ\text{C}$ ) was higher than the initial reactor temperature, the temperatures increased as reactions proceeded. When most of  $\text{Ca(OH)}_2$  disappears, the  $p\text{H}$  and removal efficiency started to decrease. In Experiment I-2, the solution volume in the 1st reactor was only two third that of the 2nd reactor, which explained the faster termination of the 1st reactor operation. However, even if the reactors had the same volume of reactants, the reactions would end earlier in the 1st reactor because the concentration of  $\text{CO}_2$  in the inlet stream was significantly higher and so was the driving force and rate of the interphase mass transfer. The temperatures did not increase linearly but saturate at some point because the higher the temperature, the more the water evaporated; consequently, more heat was lost as latent heat. Before the reactions ended, the thermodynamic equilibrium was reached when the enthalpy of the inlet stream became equivalent to the sum of enthalpies of the outlet stream, heat of reaction, and latent heat from water evaporation. The temperatures started to decrease when the reactions were complete but saturated

after a while again.

Some mismatches between the model and the real process behaviors existed; however, most of these mismatches can be explained. First, there was difference in the times when the CO<sub>2</sub> removal efficiency and pH sharply declined, particularly in Experiment I-1. Because the decline started when the base source, Ca(OH)<sub>2</sub>, was completely consumed, initial amounts of Ca(OH)<sub>2</sub> in each reactor determined the starting time point of the decrease. In the model, the amount of Ca(OH)<sub>2</sub> was calculated based on the measured height and concentration of the solution. Therefore, the errors in their measurement caused a discrepancy in the disappearing moment of Ca(OH)<sub>2</sub>. Second, the model did not behave as smooth around inflection points as the real plant. The removal efficiency curves of the plant data showed gradually decreasing behaviors whereas the modeled curves had sharp breaking points. In Figure 3-15, two steps, which broke at the time of disappearing all Ca(OH)<sub>2</sub> in each reactor, were observed. It is thought that one reason of our model showing sharp inflection points is that the population balance equations for the solid particles were not included. It is also likely that the real process may involve different reaction mechanisms when not much Ca(OH)<sub>2</sub>

is left and the dissolution rate drops, whereas the model consisted of following the same mechanism and kinetics. Indeed, it is reported that  $\text{CaCO}_3$  can precipitate on the  $\text{Ca(OH)}_2$  surface [64];  $\text{CaCO}_3$  forms the shell of particles and hinders the dissolution of  $\text{Ca(OH)}_2$ . However,  $\text{CO}_2$  can diffuse through the shell and react with  $\text{Ca(OH)}_2$  in the core part. This theory also explains the phenomenon in which a low level of the removal efficiency is still maintained after a significant drop in  $\text{pH}$ . Furthermore, the temperature changes were slightly different. It is because the complex thermodynamic behaviors of the involved materials were simplified. It was assumed that all the gas species followed the ideal gas law and did not consider interactions between them while calculating the enthalpy or density. Nonetheless, the overall tendency and maximum temperature, which is important because it significantly influences the removal efficiency, matched the plant data. In Experiments I-1 and I-2, the removal efficiency shows around 8-9 % and 5% errors based on the steady state, respectively. At the same time, the maximum temperature in Experiment I-1 shows a discrepancy of 3.1% and Experiment I-2 has 2.1% and 1.2 % errors for the 1st and 2nd reactors, respectively.

Although there was limited in predicting the termination of the

batch cycle, but the model predicted the beginning and the steady-state stages with significant accuracy. It means that the model can predict the maximum removal efficiency and temperature of the reactor from only its design and the initial operating conditions.

The changes were also monitored in the concentration of each species as well as the accumulation of the product during the operation using the model. Figure 3-16 shows that the amount of remaining  $\text{Ca(OH)}_2$  decreases, whereas the concentration of  $\text{Ca}^{2+}$  ions is still maintained at a certain level. It shows that the rate determining step of this process is not the dissolution of  $\text{Ca(OH)}_2$  but the dissolution of the  $\text{CO}_2$  gas. It is also supported by the negligible concentration of  $\text{CO}_2(\text{aq})$ ,  $\text{HCO}_3^-$ ,  $\text{CO}_3^{2-}$  ions at the same time.

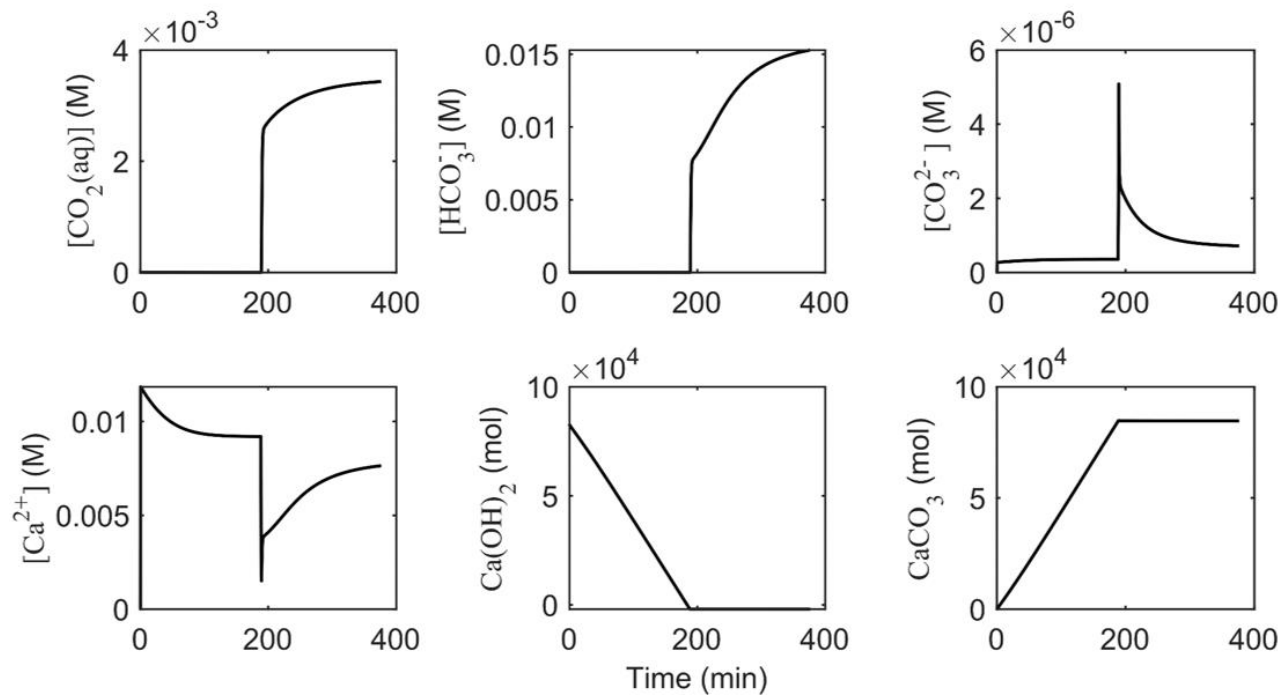


**Figure 3-16. Concentration changes of involved species during Experiment I-1.**

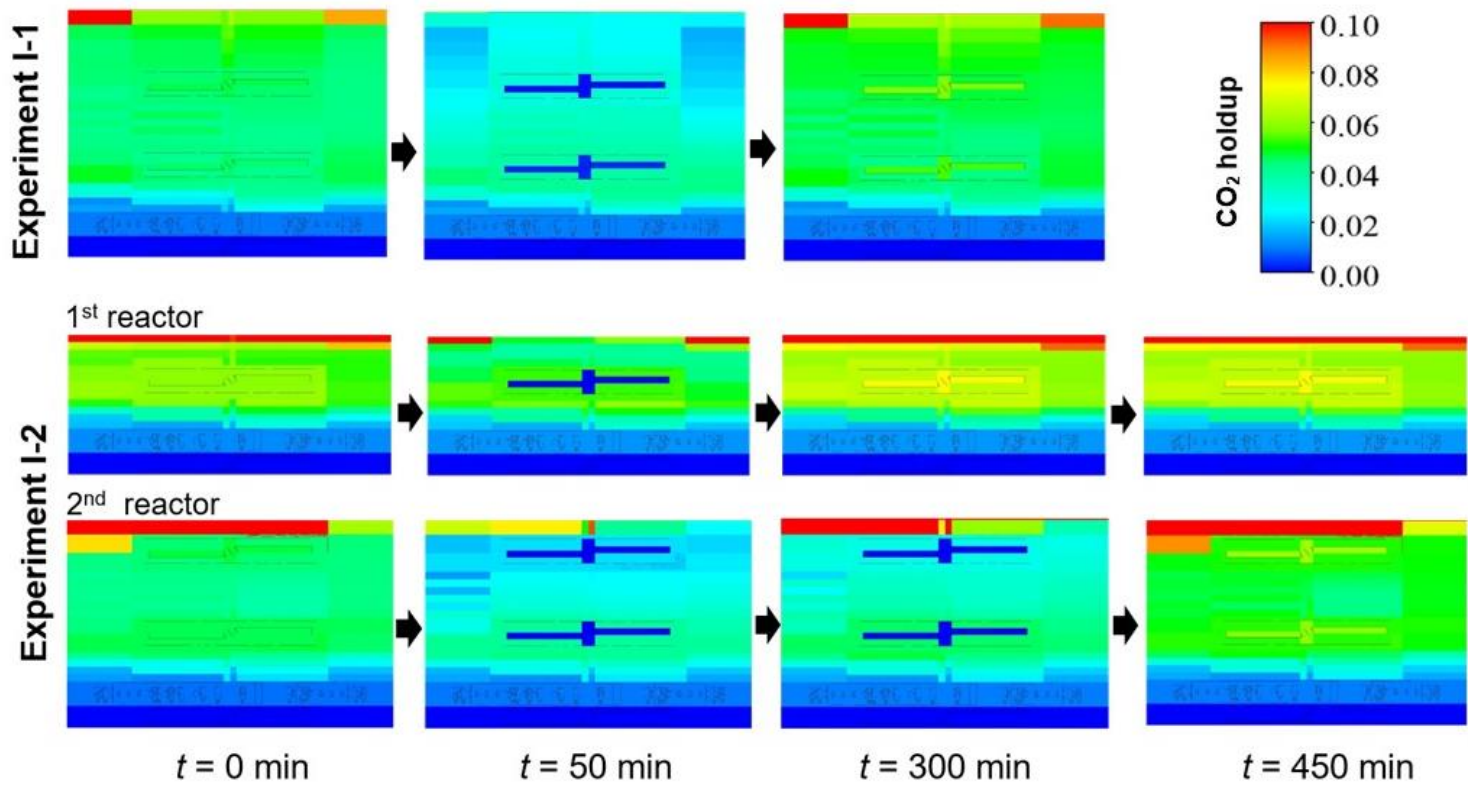


Figure 3-17. CO<sub>2</sub> holdup changes at each zone during the operation.

The concentration of CO<sub>2</sub> gas was different at each zone. Figure 3-17 shows that CO<sub>2</sub> volume fractions were generally low during the active period, in which the removal of CO<sub>2</sub> occurred. In addition, the CO<sub>2</sub> gas occupied less fraction of volume as it rose to the top, which means that CO<sub>2</sub> in the flue gas was gradually absorbed during the residence time. However, the simulation showed that the zones close to impellers did not have the CO<sub>2</sub> gas; this is because the MRF region used to simulate rotating impellers in CFD was not able to be divided into multiple zones in the compartmental model. The MRF zones have negligible inflow from the adjacent zones owing to the propelling power of impellers. However, reactions occur actively during the initial period. Therefore, the CO<sub>2</sub> holdup converges to 0 in a short time until the reactions are completed. If we could divide the MRF zones in the angular direction, the inflow from the side zone would exist at a significant level and the CO<sub>2</sub> holdup would not drop to 0.

#### **3.4.4 CFD-based compartmental model for 2.5 and 10 times larger than the industrial-scale reactor.**

The CFD-based compartmental model can help in designing reactors of different sizes and for different purposes. In this section, the model is used to predict the CO<sub>2</sub> removal efficiency of larger

reactor designs to scale-up the mineral carbonation process. Two reactor designs were proposed with different sizes to handle 2.5 (Type A) and 10 times (Type B) more flue gas than the industrial-scale one. Compared to the industrial-scale reactor, two types reactors have different internal structures to improve the performance of the proposed reactors. The configurations of the two reactors are given in Figure 3-18.

The number of zones applied to Type A and Type B reactors were 181 and 164, respectively (see Figures 3-19 & 20). The inlet volumetric flow rates were 17,500 Nm<sup>3</sup>/hr and 70,000 Nm<sup>3</sup>/hr and the initial liquid heights were 4 m and 6 m for Type A and Type B, respectively. In both reactors, the volume fraction of CO<sub>2</sub> in the inlet flue gas, the weight fraction of Ca(OH)<sub>2</sub> in the liquid reactant, and the initial temperature of the reactant were set to 15%, 20% and 20 °C, respectively. The predicted dynamic behaviors are shown in Figure 3-21.

The CO<sub>2</sub> removal efficiencies were derived only from one reactor for each type unlike the pilot- and industrial-scale plants in which two connected reactors were present and the CO<sub>2</sub> removal efficiencies were calculated from the sum of mass-transferred CO<sub>2</sub> in two reactors

in series. The CO<sub>2</sub> removal efficiencies were 85.3% for Type A and 93.9 % for Type B with single reactor. The reason for the higher CO<sub>2</sub> removal efficiencies is the initial solution height. Owing to the greater solution height, the CO<sub>2</sub> residence time increased, and this led the high removal efficiencies. Although the results must be validated afterwards, the simulations with the CFD-based compartmental model predicted that larger reactor could increase CO<sub>2</sub> removal efficiency significantly. In particular, Type B reactor did eliminate more than 400 ton of CO<sub>2</sub> every day.

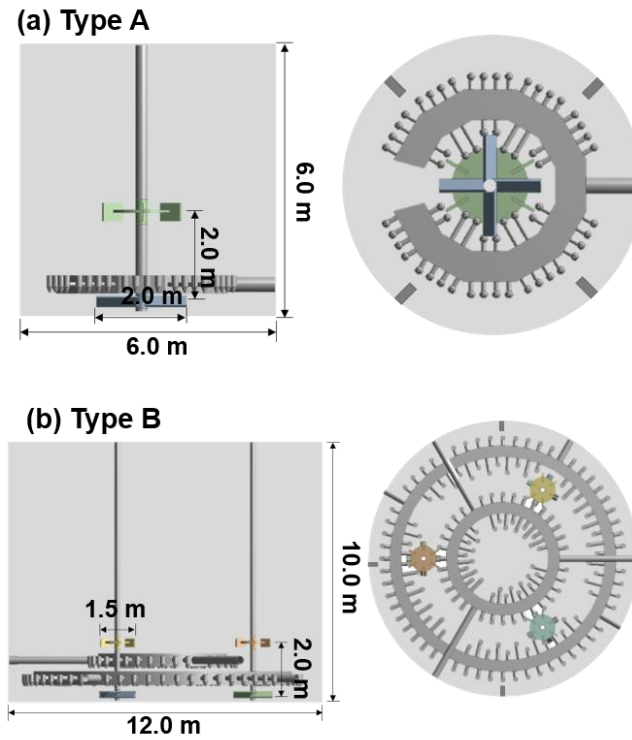


**Figure 3-18. Side and top views of Type A (gas inlet 17,500 Nm<sup>3</sup>/hr) and Type B (gas inlet 70,000 Nm<sup>3</sup>/hr) reactors.**

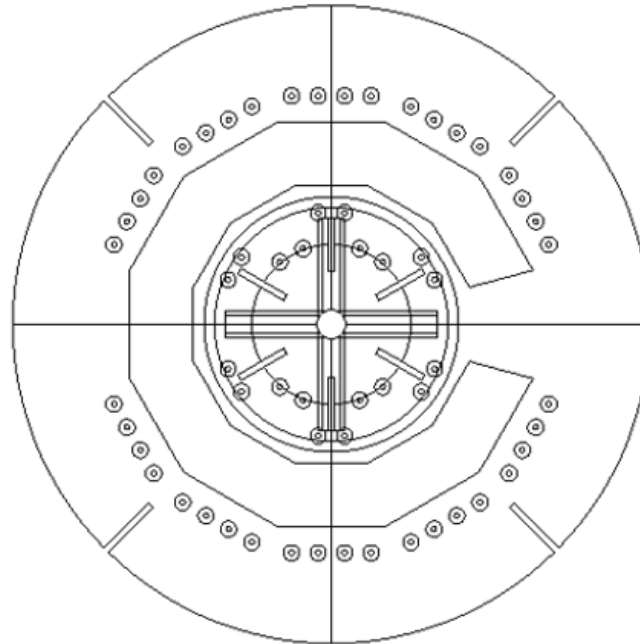
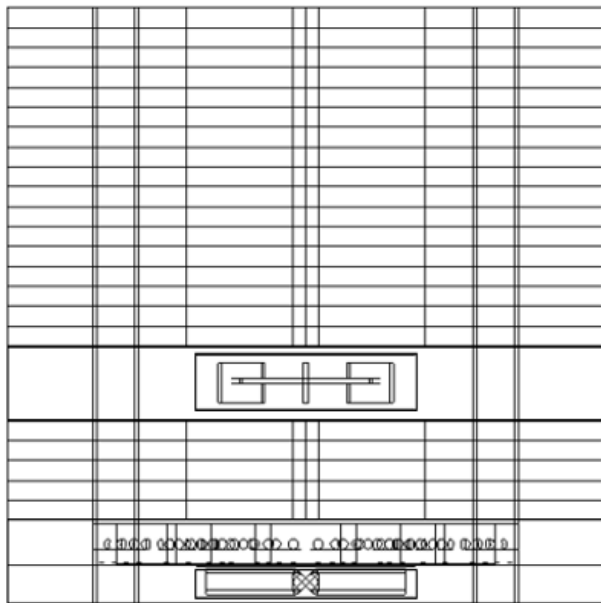


**Figure 3-19. Side and top views of the 181 compartments for Type A reactor.**

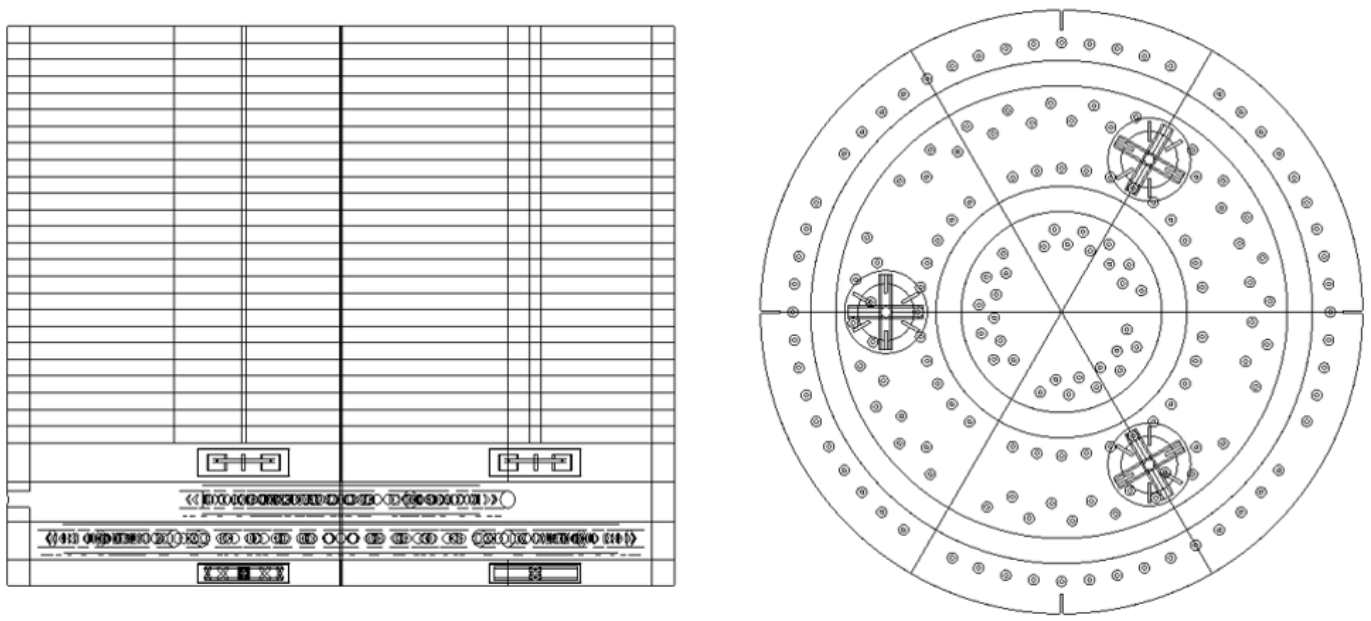


**Figure 3-20. Side and top views of the 164 compartments for Type B reactor.**

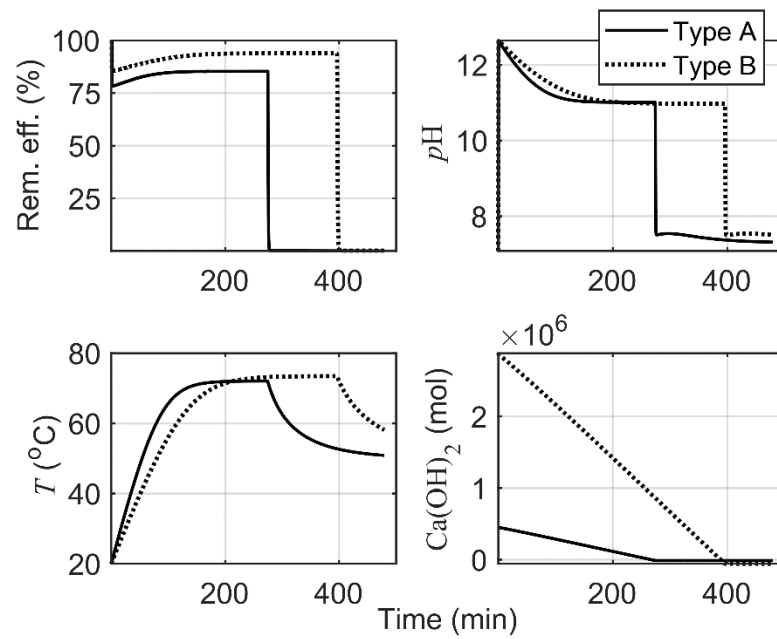


**Figure 3-21. Predicted dynamic behaviors of Type A and Type B reactors.**

## **CHAPTER 4. Long-time dynamic simulation of fluidized bed reactor using two-way coupled CFD-DQMOM approach<sup>#</sup>**

### **4.1 Objective**

In this chapter, the two-way coupled CFD-DQMOM approach is proposed and applied to FBR simulation. The two-way coupled CFD-DQMOM approach is similar to the CFD-based compartmental model but updates the flows information periodically from CFD. The approach is compared to CFD-QMOM, which simulates the flows and QMOM only in CFD, for the validation. After the validation, 6 h simulation of the FBR is conducted using the approach.

### **4.2 Modeling of gas-solid flows in fluidized bed reactor**

---

<sup>#</sup> This chapter cites the author's submitted journal article under review: M. Kim, K. Lee, Y. Bak, and J. M. Lee, "Two-way coupled CFD-DQMOM approach for long-term dynamic simulation of fluidized bed reactor," *Korean Journal of Chemical Engineering*, submitted [78].

### 4.2.1 Flow model

The Eulerian–Eulerian approach with the kinetic theory of granular flows was used as a two-phase model. The mass and momentum conservation equations are expressed as follows:

$$\frac{\partial(\alpha_k \rho_k)}{\partial t} + \nabla \cdot (\alpha_k \rho_k \mathbf{u}_k) = 0 \quad \text{Eq. 4-1}$$

$$\begin{aligned} \frac{\partial(\alpha_k \rho_k \mathbf{u}_k)}{\partial t} + \nabla \cdot (\alpha_k \rho_k \mathbf{u}_k \mathbf{u}_k) = & -\alpha_k \nabla P - \nabla P_s + \nabla \cdot \tau_k + \alpha_k \rho_k \mathbf{g} + \\ & K_{gs}(\mathbf{u}_g - \mathbf{u}_s) \end{aligned} \quad \text{Eq. 4-2}$$

where  $\alpha$ ,  $\rho$ ,  $\mathbf{u}$ , and  $P$  are volume fraction, density, velocity, and pressure, respectively, and  $k$  denotes each phase.  $K_{gs}$  is the drag coefficient between the gas and solid phase and  $P_s$  is solid pressure for considering particle interaction and there is no  $\nabla P_s$  term in the gas phase.

$$P_s = \alpha_s \rho_s \theta_s + 2\rho_s (1 + e_{ss}) \alpha_s^2 g_{0,ss} \theta_s \quad \text{Eq. 4-3}$$

where  $\theta_s$ ,  $e_{ss}$ , and  $g_{0,ss}$  are granular temperature, restitution coefficient, and radial distribution function, respectively.

$$g_{0,ss} = \left[ 1 - \left( \frac{\alpha_s}{\alpha_{s,max}} \right)^{\frac{1}{3}} \right]^{-1} \quad \text{Eq. 4-4}$$

The energy balance for the fluctuating kinetic energy is expressed as

follows:

$$\frac{3}{2} \left[ \frac{\partial}{\partial t} (\alpha_s \rho_s \theta_s) + \nabla \cdot (\alpha_s \rho_s \mathbf{u}_s \theta_s) \right] = (-P_s I + \tau_s) : \nabla \mathbf{u}_s + \nabla \cdot (k_{\theta_s} \nabla \theta_s) - \gamma_{\theta_s} + \varphi_{gs} \quad \text{Eq. 4-5}$$

The diffusion coefficient for granular energy, collisional dissipation of energy, and energy exchange between the gas and solid phases are written as follows:

$$k_{\theta_s} = \frac{15 d_s \rho_s \alpha_s \sqrt{\pi \theta_s}}{4(41-33\eta)} \left[ 1 + \frac{12}{5} \eta^2 (4 - 3\eta) \alpha_s g_{0,ss} + \frac{16}{15} (41 - 33\eta) \eta \alpha_s g_{0,ss} \right] \quad \text{Eq. 4-6}$$

$$\gamma_{\theta_s} = \frac{12(1-e_{ss}^2)g_{0,ss}}{d_s \sqrt{\pi}} \rho_s \alpha_s^2 \theta_s^{\frac{3}{2}} \quad \text{Eq. 4-7}$$

$$\varphi_{gs} = -3K_{gs} \theta_s \quad \text{Eq. 4-8}$$

where  $d_s$  and  $\eta$  are the particle diameter and  $(1+e_{ss})/2$ , respectively.

The phase stress–strain tensors  $\nabla \cdot \tau_s$  and  $\nabla \cdot \tau_g$  are expressed as

$$\tau_s = \alpha_s \mu_s (\nabla \mathbf{u}_s + \nabla \mathbf{u}_s^T) + \alpha_s \left( \lambda_s - \frac{2}{3} \mu_s \right) \nabla \cdot \mathbf{u}_s \quad \text{Eq. 4-9}$$

$$\tau_g = \alpha_g \mu_g (\nabla \mathbf{u}_g + \nabla \mathbf{u}_g^T) - \frac{2}{3} \alpha_g \mu_g \nabla \cdot \mathbf{u}_g \quad \text{Eq. 4-10}$$

where  $\mu_s$  and  $\lambda_s$  are formulated as

$$\mu_s = \mu_{s,col} + \mu_{s,kin}$$

$$= \frac{4}{5} \alpha_s^2 \rho_s d_s g_{0,ss} (1 + e_{ss}) \sqrt{\frac{\theta}{\pi}} + \frac{5\sqrt{\pi}}{48} \frac{(\rho_s d_s)}{(1+e_{ss})g_{0,ss}} \left(1 + \frac{4}{5} (1 + e_{ss}) \alpha_s\right)^2 \sqrt{\theta} \quad \text{Eq. 4-11}$$

$$\lambda_s = \frac{4}{3} \alpha_s \rho_s d_s g_{0,ss} (1 + e_{ss}) \sqrt{\frac{\theta}{\pi}} \quad \text{Eq. 4-12}$$

Among the several reported drag models for the gas–solid interphase, the following Gidaspow drag function was employed:

For  $\alpha_g \leq 0.8$ ,

$$K_{gs} = 150 \frac{\alpha_s^2 \mu_g}{\alpha_g d_s^2} + 1.75 \frac{\alpha_s \rho_g}{d_s} |\mathbf{u}_g - \mathbf{u}_s| \quad \text{Eq. 4-13}$$

For  $\alpha_g > 0.8$ ,

$$K_{gs} = \frac{3}{4} \frac{c_d(\alpha_s \rho_g)}{d_s} |\mathbf{u}_g - \mathbf{u}_s| \alpha_g^{-2.65} \quad \text{Eq. 4-14}$$

$$C_d = \begin{cases} \frac{24}{Re_s} [1 + 0.15(Re_s)^{0.687}] & , Re_s < 1000 \\ 0.44 & , Re_s > 1000 \end{cases} \quad \text{Eq. 4-15}$$

#### 4.2.2 PBM

The PBM based on the number density function (NDF) for a particle at arbitrary region can be expressed as:

$$\frac{\partial n(L; \mathbf{x}, t)}{\partial t} + \nabla \cdot [\vec{u}n(L; \mathbf{x}, t)] = B_{ag}(L; \mathbf{x}, t) - D_{ag}(L; \mathbf{x}, t) +$$

$$B_{br}(L; \mathbf{x}, t) - D_{br}(L; \mathbf{x}, t) \quad \text{Eq. 4-16}$$

where  $n(L; \mathbf{x}, t)$  is the NDF;  $L$  is the particle size;  $\mathbf{x}$  is the particle velocity vector;  $B_{ag}(L; \mathbf{x}, t)$  and  $D_{ag}(L; \mathbf{x}, t)$  are the birth and death density functions arising from particle aggregation, respectively;  $B_{br}(L; \mathbf{x}, t)$  and  $D_{br}(L; \mathbf{x}, t)$  are the birth and death density functions due to particle breakage, respectively.

#### 4.2.2.1 QMOM

The QMOM is a method to solve the PBM using moment equations and quadrature approximation. The moments of the particle size distribution (PSD) are defined as

$$m_i(\mathbf{x}, t) = \int_0^\infty n(L; \mathbf{x}, t) L^i dL \quad i = 0, 1, \dots, 2N - 1, \quad \text{Eq. 4-17}$$

where  $i$  is the specified number of moments ( $i^{\text{th}}$  moment). By applying Eq. 4-17 to Eq. 4-16, the  $i^{\text{th}}$  moment can be obtained as follows:

$$\frac{\partial m_i}{\partial t} + \nabla \cdot [\mathbf{u} m_i] = B_{ag,i}(L; \mathbf{x}, t) - D_{ag,i}(L; \mathbf{x}, t) + B_{br,i}(L; \mathbf{x}, t) - D_{br,i}(L; \mathbf{x}, t) \quad \text{Eq. 4-18}$$

$$B_{ag,i}(L; \mathbf{x}, t) = \frac{1}{2} \int_0^\infty \int_0^\infty \beta(L, \lambda) (L^3 + \lambda^3)^{\frac{i}{3}} n(\lambda; \mathbf{x}, t) n(L; \mathbf{x}, t) d\lambda dL$$

Eq. 4-19

$$D_{ag,i}(\mathbf{L}; \mathbf{x}, t) = \int_0^\infty \int_0^\infty L^i \beta(L, \lambda) n(\lambda; \mathbf{x}, t) n(L; \mathbf{x}, t) d\lambda dL \quad \text{Eq. 4-20}$$

$$B_{br,i}(\mathbf{L}; \mathbf{x}, t) = \int_0^\infty \int_0^\infty L^i a(\lambda) b(L|\lambda) n(\lambda; \mathbf{x}, t) d\lambda dL \quad \text{Eq. 4-21}$$

$$D_{br,i}(\mathbf{L}; \mathbf{x}, t) = \int_0^\infty L^i a(L) n(L; \mathbf{x}, t) dL, \quad \text{Eq. 4-22}$$

where  $\beta(L, \lambda)$  is the aggregation kernel of two particles with lengths  $L$  and  $\lambda$ , separately.  $a(\lambda)$  is the breakage kernel of length  $\lambda$ , and  $b(L|\lambda)$  is the probability distribution of length  $L$ 's breakage, which contains the information of fragment particles produced when particle breakage occurs. A moment can be calculated by the following quadrature approximation:

$$m_i(\mathbf{x}, t) = \int_0^\infty n(L; \mathbf{x}, t) L^i dL \approx \sum_{p=1}^N w_{s_p} L_{s_p}^i \quad i = 0, 1, \dots, 2N - 1,$$

Eq. 4-23

where  $s_p$  is the phase of particle  $p$ . Applying Eq. 4-23 to Eq. 4-18 yields the following quadrature form of moments:

$$\begin{aligned} \frac{\partial m_i}{\partial t} + \nabla \cdot [\bar{u} m_i] &= \frac{1}{2} \sum_p^N w_{s_p} \sum_q^N w_{s_q} (L_{s_p}^3 + L_{s_q}^3)^{\frac{i}{3}} \beta(L_{s_p}, L_{s_q}) \\ &- \sum_p^N L_{s_p}^i w_{s_p} \sum_q^N w_{s_q} \beta(L_{s_p}, L_{s_q}) + \sum_p^N a_{s_p} \bar{b}_{s_p}^i w_{s_p} - \\ &\sum_p^N L_{s_p}^i w_{s_p} a(L_{s_p}) \end{aligned} \quad \text{Eq. 4-24}$$

The following aggregation and breakage functions were used, which are widely used in the polymerization process [65, 66]:

$$\beta(L_{sp}, L_{sq}) = c_{\text{aggre}}(L_{sp}^2 + L_{sq}^2) / (L_{sp} L_{sq})^4 \quad \text{Eq. 4-25}$$

$$a(L_{sp}) = c_{\text{break}} L_{sp}^2 \quad \text{Eq. 4-26}$$

where  $c_{\text{aggre}}$  and  $c_{\text{break}}$  are the aggregation and breakage kernel constants, respectively. The probability distribution function is described based on a uniform breakage mechanism expressed as follows:

$$b(L_{sp} | L_{sq}) = \frac{6L_{sp}^2}{L_{sq}^3} \text{ if } 0 < L_{sp} < L_{sq} \text{ (else = 0)} \quad \text{Eq. 4-27}$$

$$\overline{b_p^i} = 2^{\frac{3-i}{3}} L_{sp}^i \quad \text{Eq. 4-28}$$

By solving Eq.4-24, tracking the moments of the PSD can be possible and subsequently,  $w_{sp}$  and  $L_{sp}$  are obtained through the product-difference algorithm [67].

The limitation of the QMOM is that each particle phase cannot be computed separately. In other words, if CFD and QMOM are combined, the drag coefficients from light to heavy particles cannot have distinct values; therefore, the same particle profile will be shown

for each particle. Solving Eq. 4-24 allows only the moments of all the particles to be tracked;  $w_{s_p}$  and  $L_{s_p}$  are derived through the moments of all the particles.

#### 4.2.2.2 DQMOM

In the DQMOM,  $n(L; \mathbf{x}, t)$  is approximated as an impulse train comprising  $N$  Dirac delta functions as follows:

$$n(L; \mathbf{x}, t) = \sum_{p=1}^N w_{s_p}(\mathbf{x}, t) \delta[L - L_{s_p}(\mathbf{x}, t)] \quad \text{Eq. 4-29}$$

Substituting Eq. 4-16 into 29 yields the following approximate PBM equation:

$$\begin{aligned} \sum_{p=1}^N \delta(L - L_{s_p}) \left[ \frac{\partial w_{s_p}}{\partial t} + \nabla \cdot (w_{s_p} \mathbf{u}_{s_p}) \right] - \sum_{p=1}^N \delta'(L - \\ L_{s_p}) \left[ w_{s_p} \left( \frac{\partial L_{s_p}}{\partial t} + \mathbf{u}_{s_p} \cdot \nabla L_{s_p} \right) \right] = B_{ag}(L; \mathbf{x}, t) - D_{ag}(L; \mathbf{x}, t) + \\ B_{br}(L; \mathbf{x}, t) - D_{br}(L; \mathbf{x}, t) = S(L, \mathbf{u}_{s_p}; \mathbf{x}, t) \end{aligned} \quad \text{Eq. 4-30}$$

where  $\delta'(L - L_{s_p})$  is the first derivative of  $\delta(L - L_{s_p})$ , and breakage and aggregation kernel are same as those of the QMOM. By substituting the transport equations for the weights and weighted abscissas, Eqs. 4-31 & 32, into Eq. 4-30, Eq. 4-33 can be derived as

follows:

$$\frac{\partial w_{s_p}}{\partial t} + \nabla \cdot (w_{s_p} u_{s_p}) = a_{s_p} \quad \text{Eq. 4-31}$$

$$\frac{\partial w_{s_p} L_{s_p}}{\partial t} + \nabla \cdot (w_{s_p} L_{s_p} u_{s_p}) = b_{s_p} \quad \text{Eq. 4-32}$$

$$\sum_{p=1}^N \delta(L - L_{s_p}) a_{s_p} - \sum_{p=1}^N \delta(L - L_{s_p}) [b_{s_p} - L_{s_p} a_{s_p}] = S(L, u_{s_p}; \mathbf{x}, t) \quad \text{Eq. 4-33}$$

Combining Eq. 4-23 and 4-33 yields

$$\sum_{p=1}^N a_{s_p} L_{s_p}^i (1 - i) + i b_{s_p} L_{s_p}^{i-1} = \bar{S}_i \quad \text{Eq. 4-34}$$

where

$$\bar{S}_i = \int_0^\infty S(L) L^i dL = B_{ag,i}(L; \mathbf{x}, t) - D_{ag,i}(L; \mathbf{x}, t) + B_{br,i}(L; \mathbf{x}, t) - D_{br,i}(L; \mathbf{x}, t) \quad \text{Eq. 4-35}$$

$a_{s_p}$  and  $b_{s_p}$  are calculated through a linear system of the first  $2N$  moments of PSD. The linear system is written in matrix form as:

$$Ax = d \quad \text{Eq. 4-36}$$

where the  $2N \times 2N$  matrix  $A$  is defined as:

$$A =$$

$$\begin{bmatrix} 1 & \dots & 1 & 0 & \dots & 0 \\ 0 & \dots & 0 & 1 & \dots & 1 \\ -L_{S_1}^2 & \dots & -L_{S_N}^2 & 2L_{S_1} & \dots & 2L_{S_N} \\ \vdots & \ddots & \vdots & \vdots & \ddots & \vdots \\ 2(1-N)L_{S_1}^{2N-1} & \dots & 2(1-N)L_{S_N}^{2N-1} & (2N-1)L_{S_1}^{2N-2} & \dots & (2N-1)L_{S_N}^{2N-2} \end{bmatrix}$$

Eq. 4-37

The  $2N$  vectors of  $x$  and  $d$  are expressed as

$$x = [a_{s_1} \dots a_{s_N} b_{s_1} \dots b_{s_N}]^T \quad \text{Eq. 4-38}$$

$$d = [\bar{S}_0 \dots \bar{S}_{2N-1}]^T \quad \text{Eq. 4-39}$$

If  $L_{s_p}$  is unique, then  $A$  will have a full rank and be invertible. In this case,  $L_{s_p}$  and  $w_{s_p}$  can be obtained easily by inverting  $A$  as follows:

$$x = A^{-1}d \quad \text{Eq. 4-40}$$

$$\begin{pmatrix} a_{s_1} \\ \vdots \\ a_{s_N} \\ b_{s_1} \\ \vdots \\ b_{s_N} \end{pmatrix} = \begin{bmatrix} 1 & \dots & 1 & 0 & \dots & 0 \\ 0 & \dots & 0 & 1 & \dots & 1 \\ -L_{S_1}^2 & \dots & -L_{S_N}^2 & 2L_{S_1} & \dots & 2L_{S_N} \\ \vdots & \ddots & \vdots & \vdots & \ddots & \vdots \\ 2(1-N)L_{S_1}^{2N-1} & \dots & 2(1-N)L_{S_N}^{2N-1} & (2N-1)L_{S_1}^{2N-2} & \dots & (2N-1)L_{S_N}^{2N-2} \end{bmatrix}^{-1} \begin{pmatrix} \bar{S}_0 \\ \vdots \\ \bar{S}_{2N-1} \end{pmatrix}$$

Eq. 4-41

The advantage of the DQMOM is that it can obtain each particle distribution separately with distinct drag coefficients. However, a

large computational load caused by simulating all the particle phases and the numerical problem associated with inverting a high-dimensional matrix require a short time step, e.g.,  $10^{-7}$  to  $10^{-9}$  s. This is reason CFD-QMOM was used instead of CFD-DQMOM for the verification of the two-way coupled CFD-DQMOM approach despite of the limitation of CFD-QMOM which cannot simulate each particle separately [68].

### 4.3 Reactor geometry and conditions

As shown in Figure 4-1, the height of the FBR was 2.7 m. The diameter was 0.3 m at the bottom of the reactor, which was increased to 0.45 m and then decreased again. This type of reactor are widely used to produce dynamic flows that can mix the particles well [69].

The particles were initially packed from the bottom to 1 m and had three particle sizes: 100 ( $s_1$ ), 300 ( $s_2$ ), and 700  $\mu\text{m}$  ( $s_3$ ). The  $s_1$ ,  $s_2$ , and  $s_3$  had initial volume fractions of 0.18, 0.3, and 0.12, respectively. The solid density was  $980 \text{ kg/m}^3$ , and a superficial air velocity of 0.3 m/s was introduced at the bottom of the FBR. The operating temperature and pressure were  $70 \text{ }^\circ\text{C}$  and 22 bar, respectively, which are general operating conditions of a linear low-density polyethylene process [69].

The aggregation and breakage kernel constants,  $c_{\text{aggre}}$  and  $c_{\text{break}}$ , were  $1e-35$  and  $5e-4$ , respectively. These values are very large (300 times larger than the general constants). Such large values were used to compare the two-way coupled CFD–DQMOM with CFD–QMOM, which requires a long time to simulate flows and QMOM simultaneously in CFD. However, a simulation time of several hours does not require a long time in the two-way coupled CFD–DQMOM. Or, because simulation time longer than several minutes is impossible in CFD-QMOM, larger kernel constants were used and then, the phenomenon of two models were compared for 60 s.



Figure 4-1. Configuration of FBR.

## 4.4 Methodology of the two-way coupled CFD-DQMOM

### 4.4.1 Extraction of flow information from CFD

To extract flows information from the CFD, first, the reactor is divided in vertical and horizontal direction. Four zones were created on each floor, and the number of floors was determined by the sensitivity analysis described in Section 4.5.1.3. After that, from the CFD-hydrodynamics model,  $\alpha_{sp}^{(i,j)}$ , volume fraction of particle  $p$  in  $i$ - $th$  floor  $j$  zone, is also obtained and used as an initial condition of DQMOM equations.

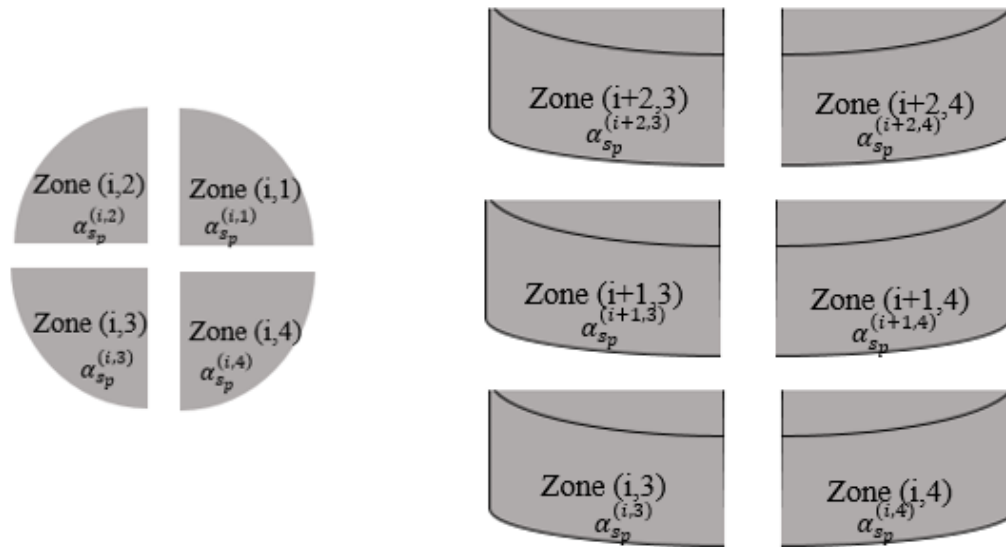


Figure 4-2. Zone configuration and particle volume fraction ( $\alpha_{sp}^{(i,j)}$ ).

#### **4.4.2 Two-way coupled CFD-DQMOM simulation**

For the two-way coupled CFD–DQMOM simulation, the CFD–hydrodynamics simulation, which calculates only flows without the PBM in CFD, proceeds until the flows are relatively stable. It was confirmed that a simulation time of approximately 15 s was sufficient to acquire nearly steady-state flows. From the simulation, the particle volume fraction of each zone and particle was obtained. Using the data above, the DQMOM equations (Eqs. 4-31–42) were solved for each zone in MATLAB, where the convection of particles between the zones in Eqs. 4-31 and 32 was assumed to be zero because the changes in the flows were negligible after 15 s. To reflect the DQMOM results and update the flows in the FBR, a CFD setup was established for the particle length and particle volume fraction of each zone. Additionally, each particle was modified and the CFD simulation was implemented again to obtain the updated flows.

A sensitivity analysis was performed to determine the time interval required to update the flow information. Based on the analysis, 10 s was selected with slight changes in the results when the time interval was further decreased (see Figure 4-4). Large aggregation and breakage kernel were used to compare the results with the CFD–

QMOM results, where the large kernels resulted in a sudden change in the flows over several seconds, requiring a short time interval. However, when the constants of the kernels were not large, a time interval of 15 min or 1 h was appropriate for updating the flow information.

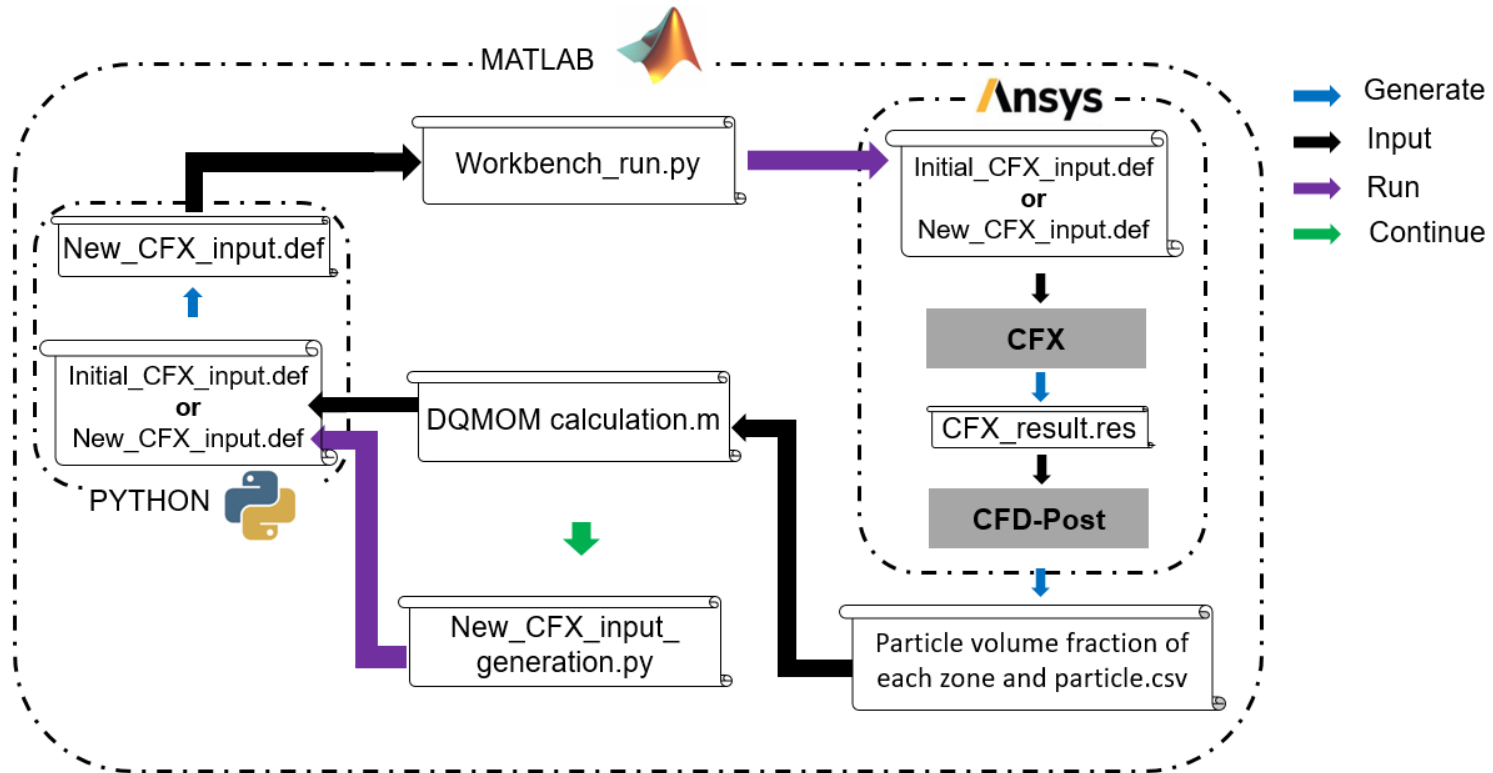


Figure 4-3. Systematic diagram for the two-way coupled CFD-DQMOM simulation

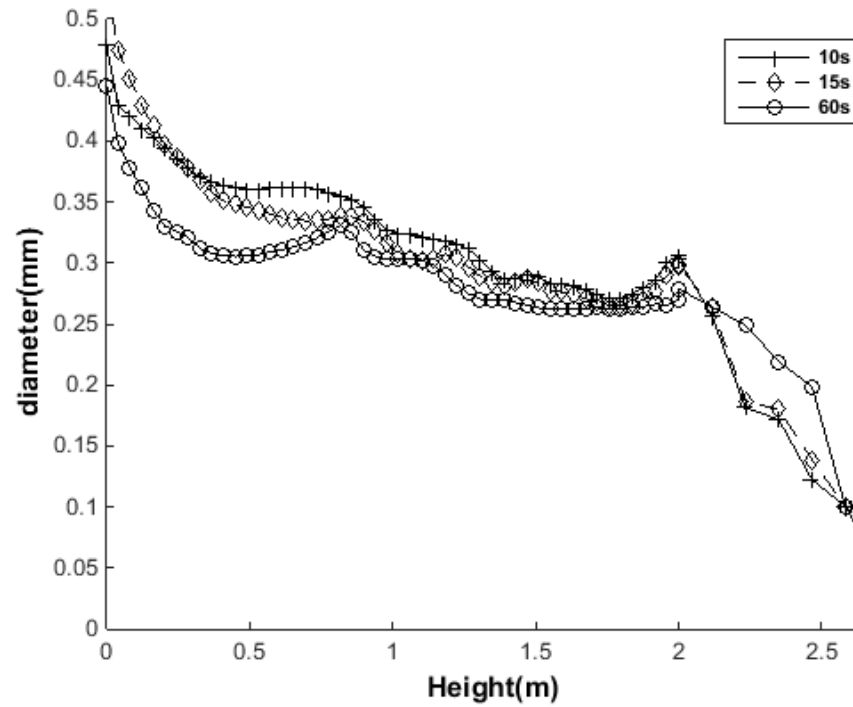


Figure 4-4.  $d_{32}$  (Sauter mean diameter) along height for the flows updating interval of 10, 15, and 60 s models.

## 4.5 Simulation setup

CFD packages of ANSYS CFX 19.5 and FLUENT 18.2 (Ansys, USA) were used for CFD simulations. The reactor geometry and meshes were generated using the DesignModular and AnsysMeshing modules, respectively, and simulations were performed on an Intel Xeon E5-2690 (24 cores) with 128 GB RAM. The number of nodes of 307,776 was determined by the mesh robustness test, in which the number of nodes was increased until a further increase in the number of nodes exerted no effect on the results in the CFD–hydrodynamics model (See Figure 4-5). A standard  $k$ – $\epsilon$  model was used as a turbulence model. For the inlet condition, a uniform inlet condition was specified at the bottom of the reactor. The outlet condition was set as the gauge static pressure of 0 Pa. At the walls, no-slip conditions were applied for both the gas and solid phases.

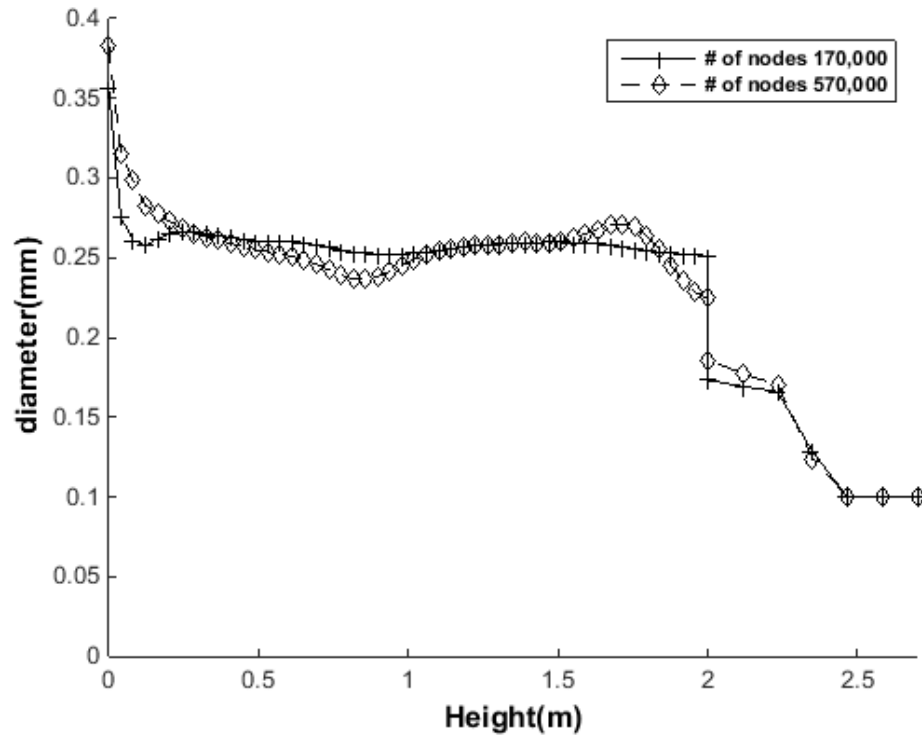


Figure 4-5.  $d_{32}$  along height for the number of nodes of 170,000 and 570,000 models.

## **4.5.1 Two-way coupled CFD-DQMOM setup**

### **4.5.1.1 CFD-hydrodynamics simulation**

An upwind was selected for the advection scheme, and the first-order backward Euler was used for the transient scheme. The convergence loops were within 1–20, and the convergence criterion of  $10^{-4}$  with a time step of 0.002–0.005 s was set. The particle volume fraction and the lengths of each zone and each particle calculated from the DQMOM in MATLAB were set as the initial conditions for the next step using a user-defined function.

### **4.5.1.2 DQMOM simulation in MATLAB**

To solve the DQMOM equations, particle length normalization was first performed; 1, 3, and 7 were used instead of 100, 300, and 700  $\mu\text{m}$  as length of particles for the stability [70]. The timestep was set to 0.001 s, it is confirmed that a decreasing timestep could not affect the DQMOM calculation. The DQMOM calculation was continued using Eqs. 4-31 – 4-42, and the final solutions of the DQMOM, the particle volume fraction, and the lengths of each zone and each particle were applied as the initial conditions for the next CFD–hydrodynamics model.

### **4.5.1.3 Zoning Method**

The sensitivity analysis was used to determine the appropriate number of floors in the FBR. The number of floors were varied from 21 (84-zone) to 87 (348-zone) and from the sensitivity analysis, it was confirmed that 57 floors (228-zone) were appropriate showing the increasing number of floors can change little results (See Figure 4-6). In Figure 4-7, a side views of 84, 228, and 348-zone models are given.

### **4.5.2 CFD-QMOM simulation setup**

The CFD-QMOM simulation was performed using FLUENT's built-in QMOM module. Furthermore, FLUENT's built-in DQMOM module was available; however, it requires an excessive amount of computational resources, e.g., a time step of  $10^{-7}$  s, rendering it infeasible to simulate for 60 s, and some stability issues have been reported. Moreover, the author encountered a stability issue when using FLUENT's own DQMOM code [71]. In the QMOM simulation, minimum and maximum size of particle were set to 0.08 mm and 2 mm, respectively. The volumetric shape factor ( $k_v$ ) was set to  $\pi/6$  and the total number of moments was six. A phase-coupled SIMPLE scheme was set, and the first-order upwind scheme was used. The

convergence loops were within 1–40, and a fixed time step of 0.001 s was set.

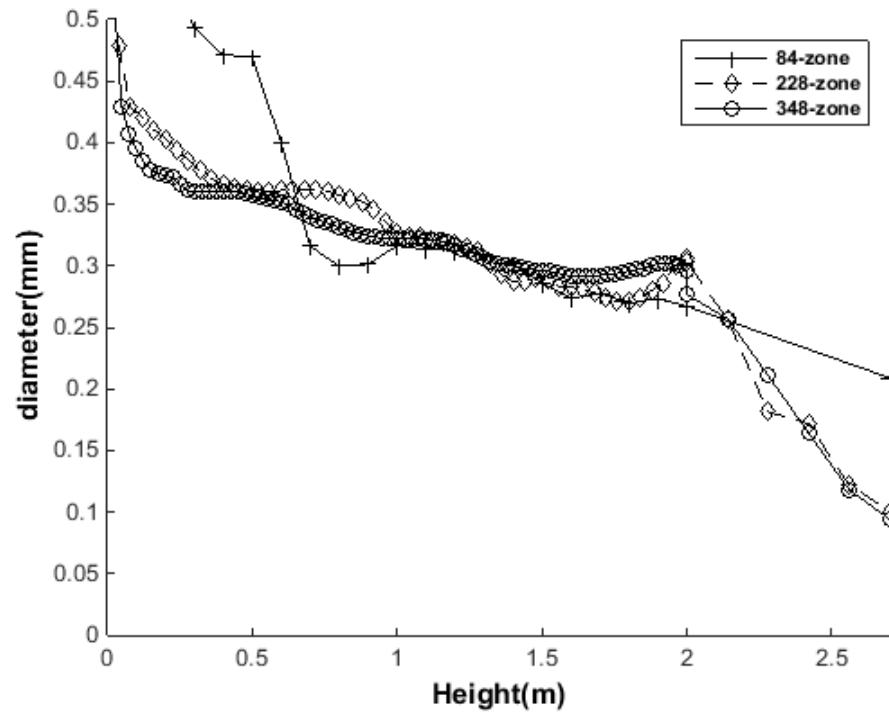
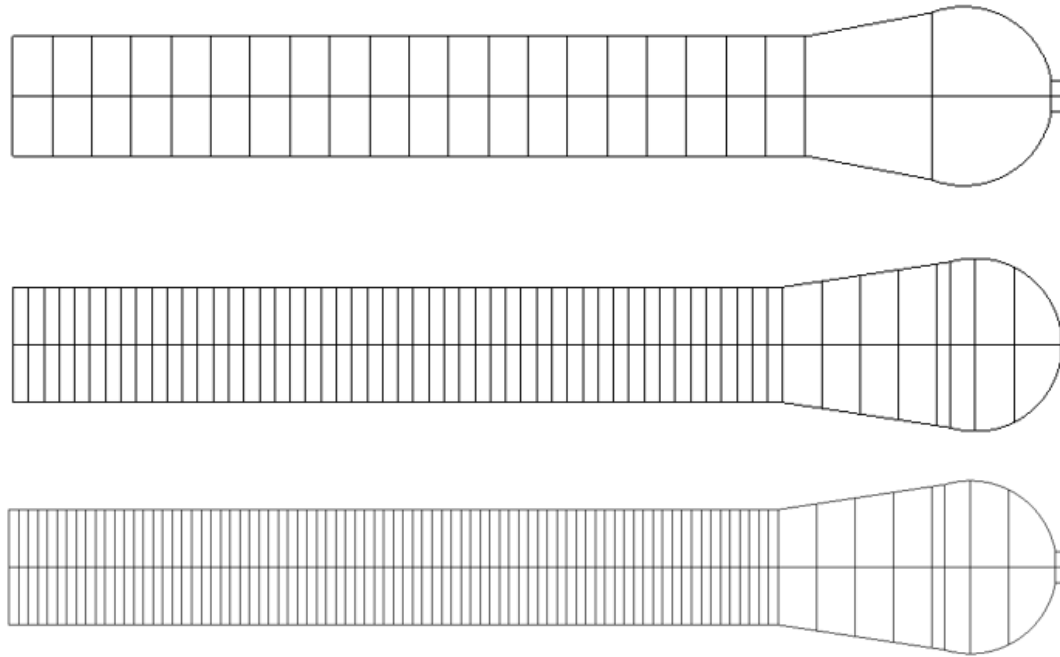


Figure 4-6.  $d_{32}$  along height for the 84, 228, and 348-zone models



**Figure 4-7. Side view of 84, 228, and 348-zone model.**

## **4.6 Results and discussion**

In section 4.6.1 and 4.6.2, to verify the proposed approach, the two-way coupled CFD-DQMOM and CFD-QMOM results were compared for 60 s with large aggregation and breakage constants. In section 4.6.3, using normal aggregation and breakage constants, a simulation was performed for 6 h using the two-way coupled CFD-DQMOM approach.

### **4.6.1 Two-way coupled CFD-DQMOM results**

For the 60 s FBR simulation, a CFD simulation without DQMOM calculation was first performed. In the first CFD-hydrodynamics calculation, each particle had a constant particle size and the flows were primarily affected by the drag force calculated from the constant particle size. Because the particle aggregation effect was not considered in the CFD hydrodynamics, the particles could rise higher in the FBR. Hence, using the Gidaspow drag model without any correction for the drag effect caused the solid bed height to be larger; several drag models including the energy minimization multi-scale drag model, which introduces the drag force correction factor to account for particle aggregation and breakage, have been studied for

the validation of solid bed height [72-74]. After the CFD–hydrodynamics calculation, the particle volume fractions of each zone and particle size processed in MATLAB for the DQMOM calculation. In the latter, the particle volume fraction and length were obtained and sent to the CFD–hydrodynamics model again to update the flow information. As shown in Figure 4-8, the flows of the second CFD–hydrodynamics model differed from those of the first one. The main difference was the light particle ( $s_1$ ), which was clustered and whose diameter was larger than the original particle size. Consequently, at the top part of the FBR, the clustering effect was reflected through the DQMOM calculation and the solid bed height was reduced. As shown in Figures 4-8 and 9, the final flows differed significantly from the initial flow. The representative diameter of  $s_1$  particles increased from 0.1 mm to 0.12–0.17 mm, and most of the  $s_1$  particles grew to the size of  $s_2$  particles, with a low  $s_1$  particle volume fraction left at the final flows. Meanwhile, the representative diameter of  $s_3$  particles decreased from 0.7 to 0.45–0.65 mm and some of the  $s_2$  particles grew to the size of the  $s_3$  particles, causing an increase in the total volume fraction of the  $s_3$  particles. The  $s_2$  particles showed a similar volume fraction profile, as shown in Figure 4-9; however, the  $d_{32}$  distribution

along the height indicated a decreasing  $d_{32}$  along the height (see Figure 4-10), which could not be modeled in the CFD–hydrodynamics model with a constant particle size in all parts of the FBR.

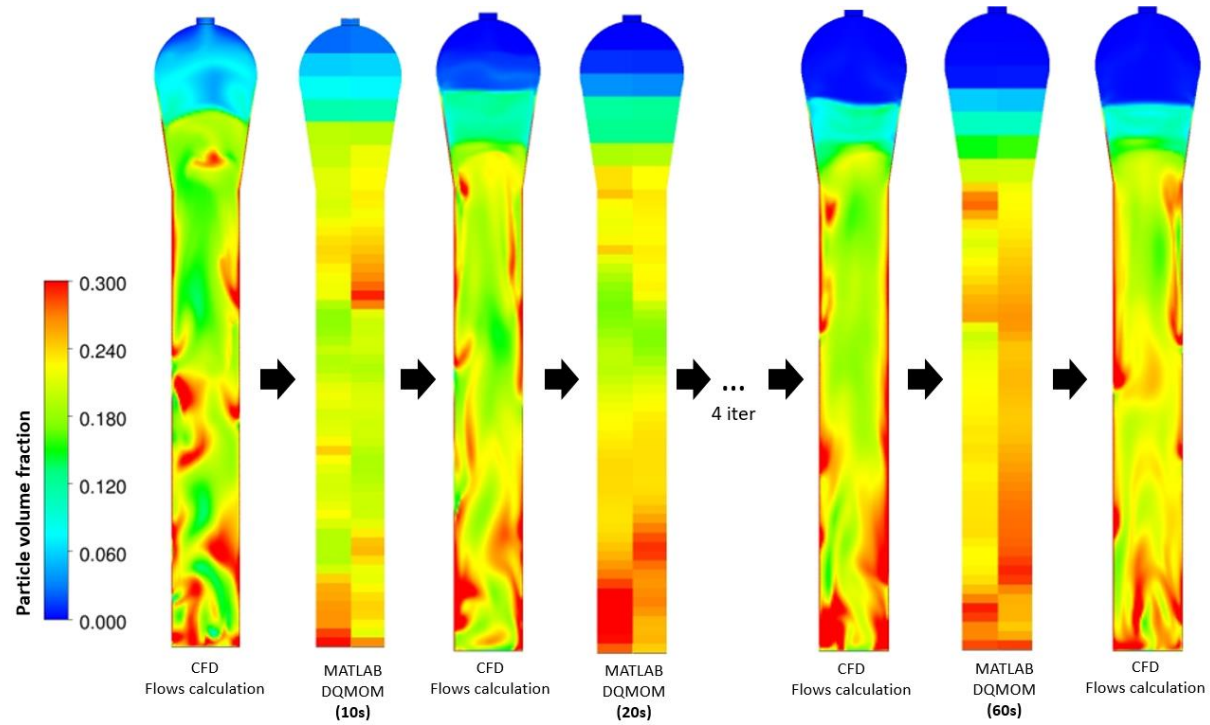


**Figure 4-8. Particle volume fraction profiles for 60 s in the two-way coupled CFD-DQMOM model.**

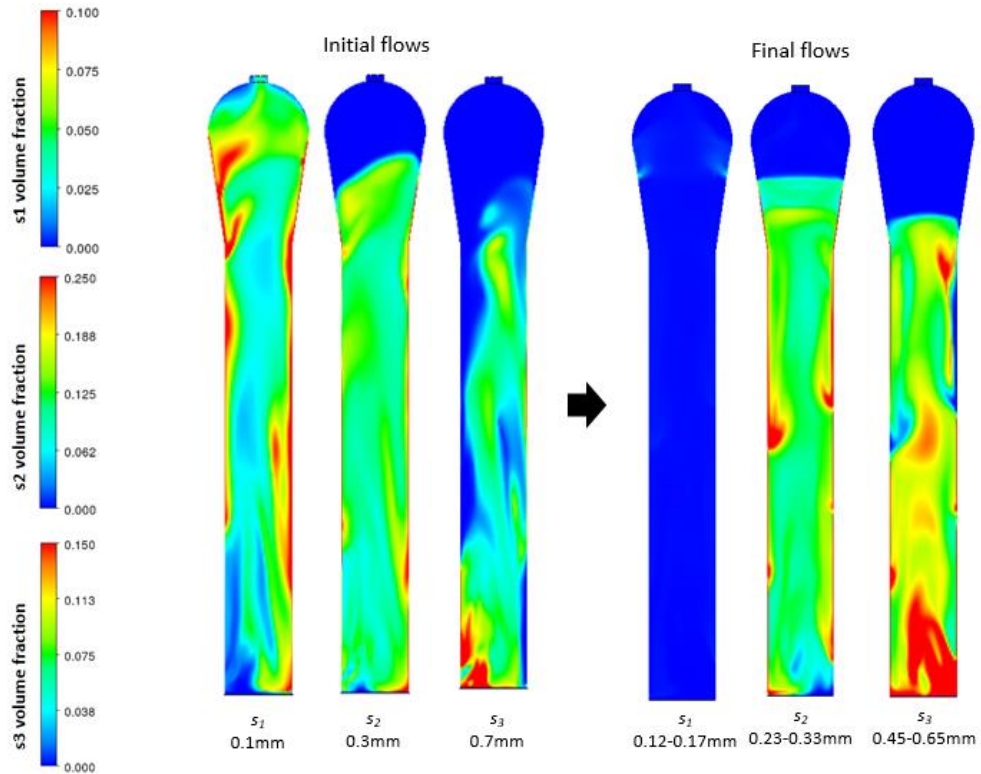


**Figure 4-9. In initial and final-state, particle volume fraction profiles for each particle.**

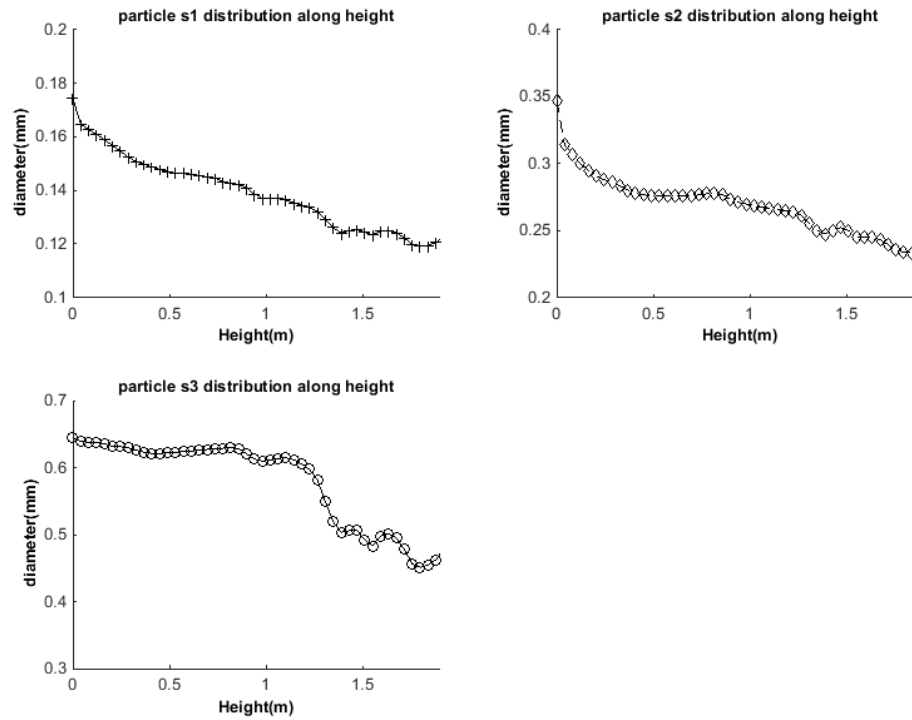


**Figure 4-10.  $d_{32}$  along height for  $s_1$ ,  $s_2$ , and  $s_3$  particles.**

The particle size distributions at each floor are shown in Figure 4-11. At the bottom part (0–0.2 m), the  $s_3$  particles dominated from the initial to the final state. This is a predicted result that a heavy particle exists at the bottom. As the height of the FBR increased, the ratio of particle  $s_2$  increased, whereas that of  $s_3$  decreased, and the sum of all the particle volume fractions decreased. In the final state, particle  $s_1$  rarely appeared, and the volume fraction of particles  $s_2$  and  $s_3$  increased compared with the initial state. The representative diameter of  $s_3$  decreased and the diameter of  $s_1$  increased in all parts. The representative diameter of  $s_2$  increased at the bottom part (0–0.2 m) but decreased in the other parts.

These results confirmed that the CFD–hydrodynamics model, a traditional CFD model, cannot yield reliable results owing to challenges in considering particle interactions. Previous studies have reported that the conventional CFD model cannot be validated without any special tuning for the drag function [75-77]. The two-way coupled CFD–DQMOM model can visualize realistic flows, including several particle interactions.

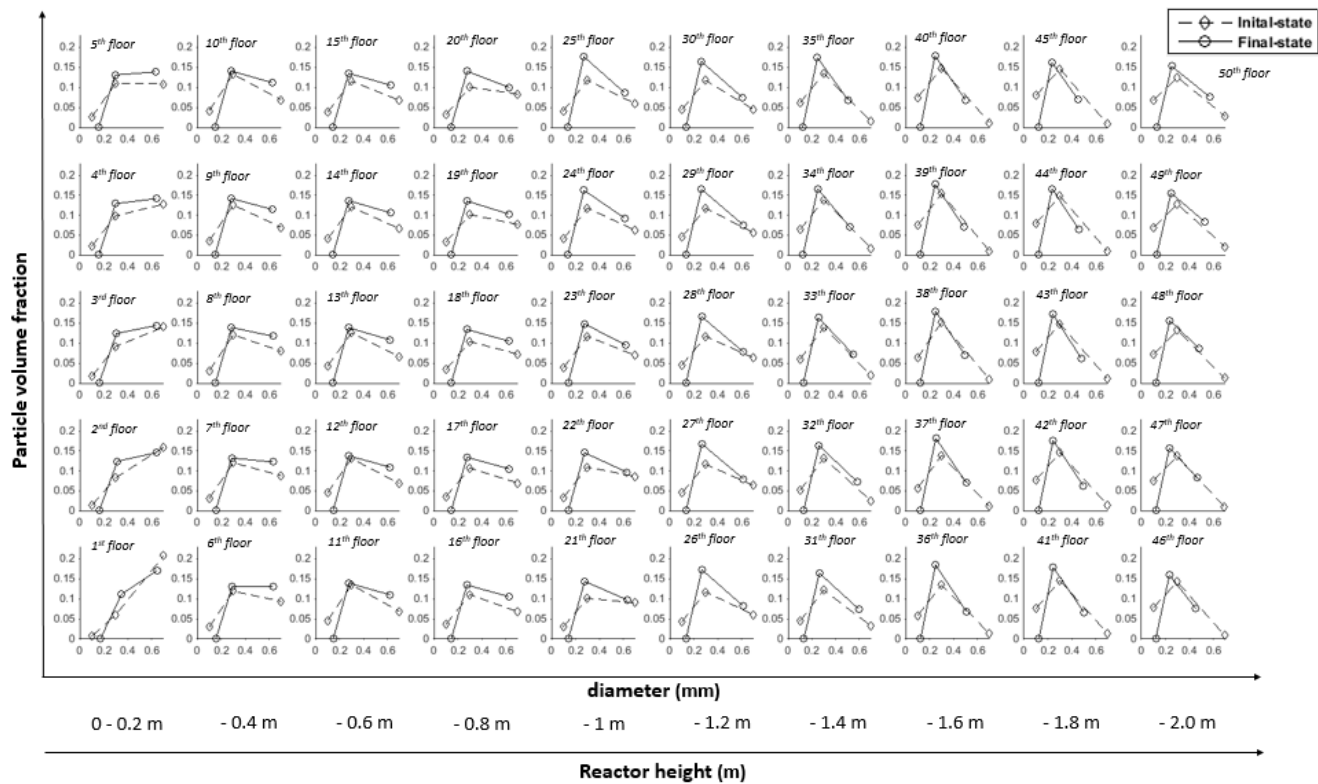


Figure 4-11. Particle size distribution from 1st to 50th floor in initial and final-state.

#### 4.6.2 CFD-QMOM results

To verify the two-way coupled CFD–DQMOM approach, CFD–QMOM calculation was performed for 60 s through FLUENT’s QMOM implementation code. Table 4-1 shows the mean diameter and ratios of each particle at 60 s. All the particles’ mean diameters of the CFD–QMOM model converged to those of the two-way coupled CFD–DQMOM model with little error; only the mean diameter of particle  $s_1$  indicated an error of approximately 10%. Meanwhile, the ratio of particle  $s_1$  decreased significantly, whereas that of  $s_2$  increased in the two models. The ratio of particle  $s_3$  increased in the two-way coupled CFD–DQMOM model but decreased in the CFD–QMOM model. All the errors in the particle ratio and  $s_1$  mean diameter were caused by the limitations of the CFD–QMOM model. This was because the Eulerian–Eulerian approach of the CFD–QMOM model only considered the gas and solid phases without a distinct particle phase, i.e., a two-phase model. As shown in Figure 4-12 (right), in the CFD–QMOM model, the particle volume fraction profiles of all the particles were the same except for the absolute value. Consequently, a light particle could not float higher and a heavier particle could not settle down. Because the  $s_1$  particles could not float

higher, they appeared throughout the reactor and had a larger  $s_1$  volume fraction than the two-way coupled CFD-DQMOM model. In addition, because the  $s_3$  particles could not settle down, they had a much smaller volume fraction than the two-way coupled CFD-DQMOM model. As shown in Figures 4-11 and 12, at the bottom part, the  $s_3$  particle volume fraction was approximately 0.15 in the two-way coupled CFD-DQMOM model, whereas the value was approximately 0.04 in the CFD-QMOM model. In addition, the solid bed height was 0.3 m higher in the CFD-QMOM model than the two-way coupled CFD-DQMOM model.

By comparing the two models, a general trend can be predicted for the final mean diameter of each particle; however, the solid volume fraction profile of the two-way coupled CFD-DQMOM model cannot be validated. It is concluded that the two-way coupled CFD-DQMOM model yields more realistic results and requires a shorter time to simulate the reactor. In conclusion, although the two-way coupled CFD-DQMOM model is not fully validated, the proposed scheme can simulate realistic trends and results with a much lower computational cost than the CFD-QMOM model.

**Table 4-1. Final result of each particle mean diameter and ratio for the CFD-hydrodynamic, two-way coupled CFD-DQMOM, and CFD-QMOM models**

<b>Model</b>	<b>CFD-hydrodynamics</b>	<b>Two-way coupled CFD-DQMOM</b>	<b>CFD-QMOM</b>
<i>s</i> <sub>1</sub> mean diameter (mm)	0.1	0.140	0.154
<i>s</i> <sub>2</sub> mean diameter (mm)	0.3	0.265	0.260
<i>s</i> <sub>3</sub> mean diameter (mm)	0.7	0.590	0.588
<i>s</i> <sub>1</sub> particle ratio	0.3	0.0004	0.0577
<i>s</i> <sub>2</sub> particle ratio	0.5	0.6425	0.7571
<i>s</i> <sub>3</sub> particle ratio	0.2	0.3571	0.1852

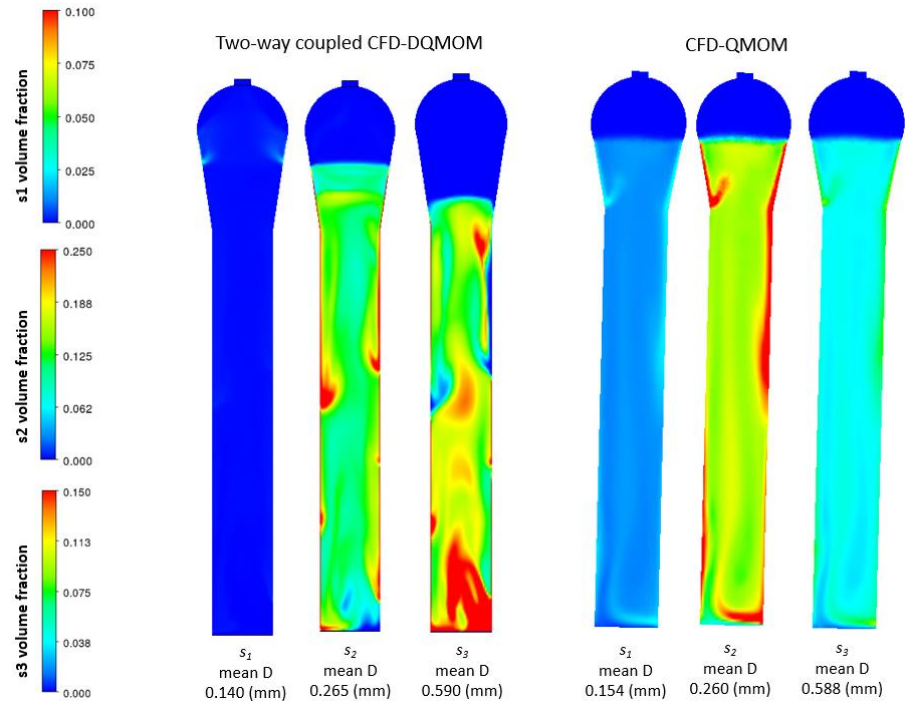


**Figure 4-12. Particle volume fraction profiles of each particle for the two-way coupled CFD-DQMOM model (left) and CFD-QMOM model (right).**

### 4.6.3 Two-way coupled CFD-DQMOM simulation for 6h

This section describes the capability of the proposed approach in performing long-term simulations. To illustrate, a 6 h simulation was performed using normal kernel constants; the aggregation and breakage kernel constants were  $3.33\text{e-}38$  and  $1.67\text{e-}6$ , respectively. The time interval for the flow update was set to 0.5 h. In other words, the flows derived from the CFD–hydrodynamics model were used for the DQMOM calculation in MATLAB for 0.5 h; subsequently the new CFD–hydrodynamics simulation was performed for updating the flows. Because the kernel constants were 300 times smaller, the flows did not change significantly for 0.5 h. Figure 4-4 shows that an updating interval of 10 s was appropriate for 300X larger constants. With linear scaling, an interval shorter than 3000 s was appropriate for 300X smaller constants. Finally, through 12 updates, a 6 h simulation was completed successfully without any computational problems. As shown in Figure 4-13, the solid bed height decreased over time, and Figure 4-14 shows changes in the particle size distribution in each floor, which is similar to the results in Section 4.6.1. Hence, it is concluded that the proposed model can provide the long-term dynamic behaviors of FBRs in a reasonable time.

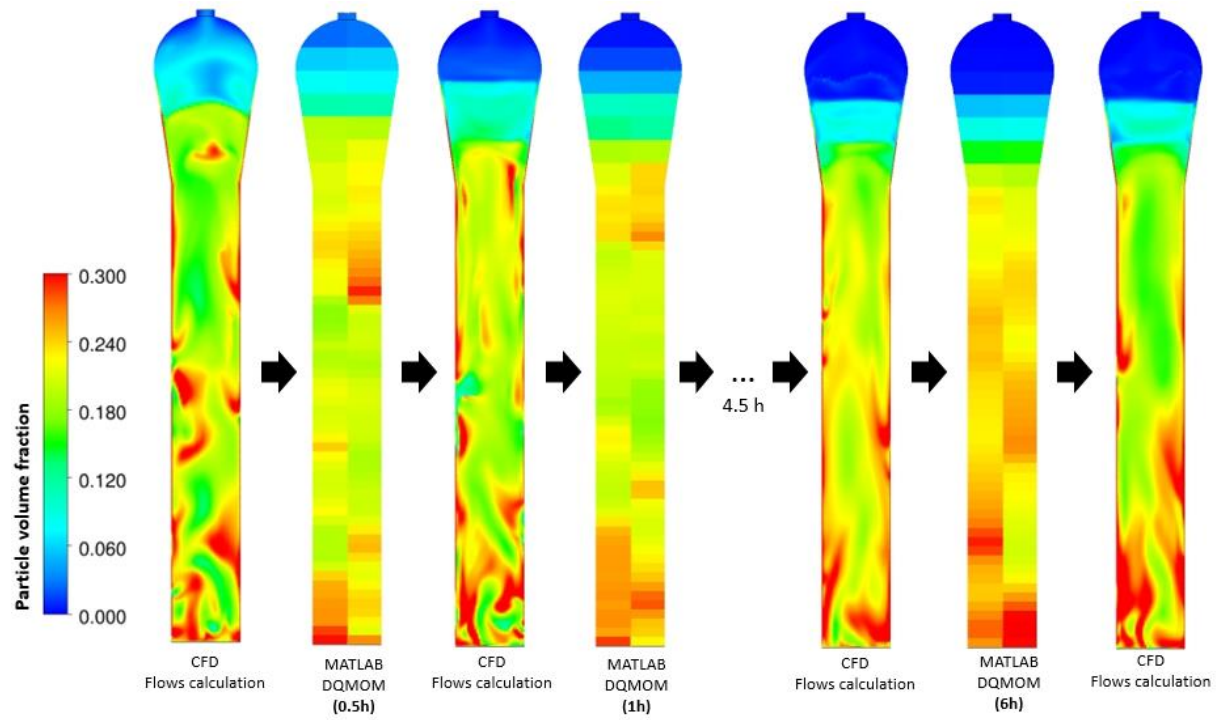


**Figure 4-13. Particle volume fraction profiles for 6 h in the two-way coupled CFD-DQMOM model.**

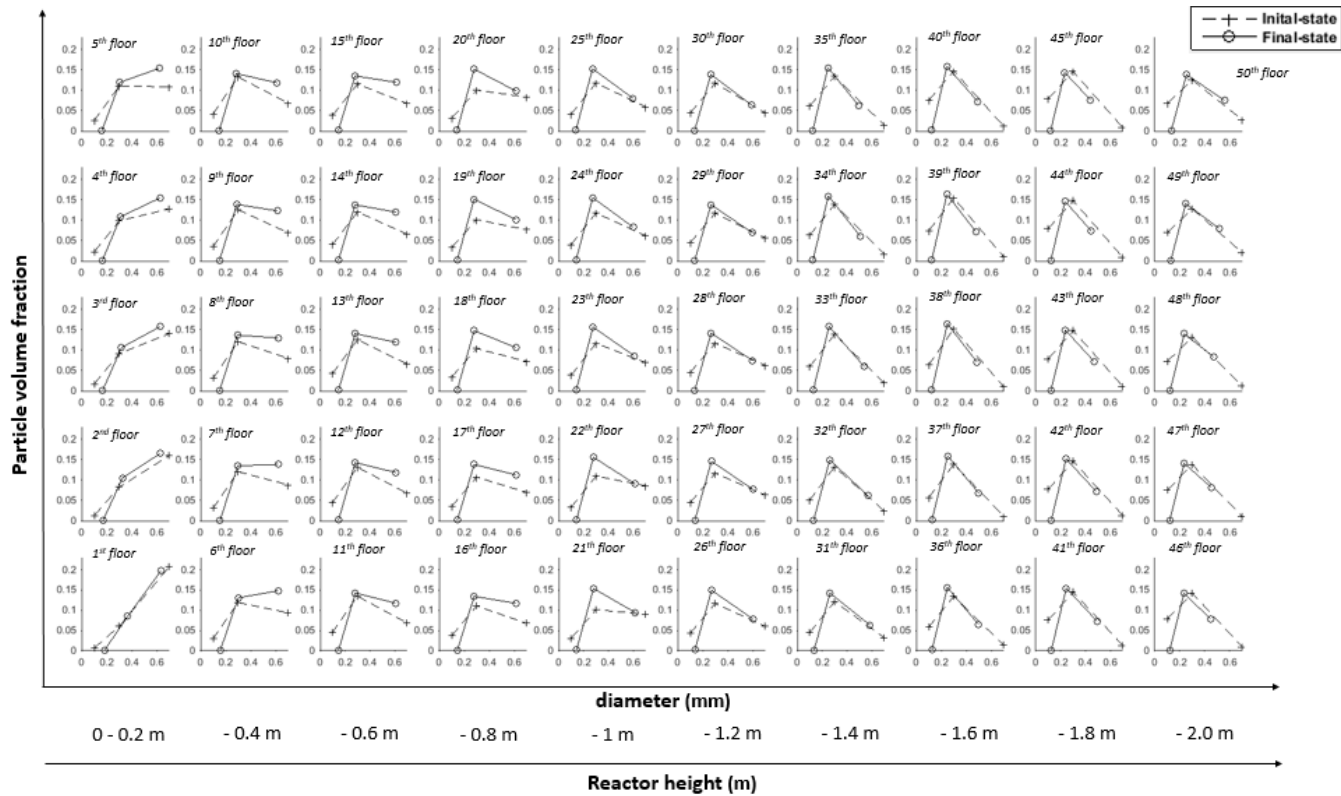


Figure 4-14. Particle size distribution from 1st to 50th floor in initial and final-state for 6 h simulation.

## **CHAPTER 5. Concluding Remarks**

### **5.1 Conclusion**

Various methodologies have been proposed to simulate industrial-scale multiphase reactors for a long time using CFD.

When multiphase reactors are simulated in CFD, it is important to predict the interactions between disperse phase with high accuracy. PBM is being used to simulate these physical phenomena, but because of the limitation that the computation load is exorbitant in PBM, most studies are limited to simulating a laboratory-scale reactor for a few seconds. Therefore, in CHAPTERS 2 & 3, the interaction between disperse phase was considered through lumped correlation, and the computation time could be drastically reduced. Subsequently, the CFD-based compartmental model was used to simulate the industrial-scale reactor for a long time. The CFD-based compartmental model was very useful for simulating the reactor for a long time because only flow calculations were performed in millions of meshes and the rest of the chemical reactions were performed in hundreds of zones.

However, there were limitations in the lumped correlation model and CFD-based compartmental model used in CHAPTERS 2 & 3. First, in the case of lumped correlation, in order to be used in other systems, there must be a lumped correlation to represent the interaction between disperse phase. The lumped correlation used in this thesis can be used to gas-liquid system and cannot be applied to gas-solid system. Second, since the CFD-based compartmental model receives flow information only once and performs simulation for a long time using the information, it is inappropriate when the flow changes as the reactor operates. Therefore, in order to solve these two limitations, this thesis proposed a two-way coupled CFD-DQMOM approach. Interactions between disperse phase can be simulated by calculating DQMOM in compartmental model. In addition, by periodically sending DQMOM results to CFD to extract and use new flow information, it is possible to simulate the reactor for a long time while taking into account flow changes over time.

Using the CFD-based compartmental model and the two-way coupled CFD-DQMOM approach developed in this thesis, industrial-scale multiphase reactors such as crystallization, slurries, and fermentation can be simulated for a long time while considering

chemical reactions and particle the interactions between disperse phase. Furthermore, additional chemical reactions or physical phenomena can be included with only a small supplement of computational load because reaction kinetics and physical phenomena are calculated in hundreds of zones instead of millions of meshes. However, when the chemical reaction or physical phenomena are rapid, the time interval for updating the flow information should be reduced, which may be prohibitive to computational loads for long-term simulations.

## **5.2 Future work**

### **5.2.1 Turbulence effect caused by physicochemical phenomena.**

Various physicochemical phenomena such as particle breakage, aggregation, and mass transfer exist inside the multiphase chemical reactor. Although these phenomena produce large and small turbulence, this thesis assumed that there is no turbulence effect for an economical CFD model; various variables such as mass transfer coefficient and interfacial area can be affected by turbulence. Therefore, it is of interest to develop a methodology that can consider turbulence effect; for example, turbulence effect may be considered

by automatic compartmentalization method using a turbulence variable, though it has not been reported that the automatic compartmentalization method can show more accurate results than manual method.

### **5.2.2 Number of bins that can be flexibly changed in DQMOM**

In DQMOM calculation, quadrature weight and particle size are obtained by calculating the inverse matrix of Eq. 4-37. When determining the number of bins, if the number of bins is greater than 3, the probability of having the singularity condition increases and it makes the number of bins set to 3 or less generally. The singularity condition means that the particle sizes are dependent. Therefore, if the number of bins can be flexibly reduced when the specific zone has singularity condition by reconstructing matrix, the number of bins can be flexibly larger or smaller. For the accuracy and flexible DQMOM calculation, it is of interest to find a methodology for reconstructing matrix with singularity condition.

### **5.2.3 Integration of kinetics and PBM**

CHAPTERS 2 & 3 deal with kinetics and CHAPTER 4 deal with PBM. Therefore, it is of interest to simulate a reactor combining both

kinetics and PBM using a two-way coupled CFD-PBM-kinetics model.

## Bibliography

- [1] W. Strasser and A. Wonders, "Commercial scale slurry bubble column reactor optimization," *WIT Transactions on Engineering Sciences*, vol. 59, pp. 275-287, 2008.
- [2] S. Park, J. Na, M. Kim, J. An, C. Lee, and C. Han, "CO<sub>2</sub> Mineral Carbonation Reactor Analysis using Computational Fluid Dynamics: Internal Reactor Design Study for the Efficient Mixing of Solid Reactants in the Solution," *Korean Chemical Engineering Research*, vol. 54, pp. 612-620, 2016.
- [3] S. Zimmermann and F. Taghipour, "CFD modeling of the hydrodynamics and reaction kinetics of FCC fluidized-bed reactors," *Industrial & Engineering Chemistry Research*, vol. 44, pp. 9818-9827, 2005.
- [4] S. Park, J. Na, M. Kim, and J. M. Lee, "Multi-objective Bayesian optimization of chemical reactor design using computational fluid dynamics," *Computers & Chemical Engineering*, vol. 119, pp. 25-37, 2018.
- [5] R. Fan, D. L. Marchisio, and R. O. Fox, "Application of the direct quadrature method of moments to polydisperse gas–solid fluidized beds," *Powder Technology*, vol. 139, pp. 7-20, 2004.
- [6] S.-S. Liu and W.-D. Xiao, "Numerical simulations of particle growth in a silicon-CVD fluidized bed reactor via a CFD–PBM coupled model," *Chemical Engineering Science*, vol. 111, pp. 112-125, 2014.
- [7] Y. Yao, Y.-J. He, Z.-H. Luo, and L. Shi, "3D CFD-PBM modeling of the gas–solid flow field in a polydisperse polymerization FBR: The effect of drag model," *Advanced Powder Technology*, vol. 25, pp. 1474-1482, 2014.
- [8] Y. Yao, J.-W. Su, and Z.-H. Luo, "CFD-PBM modeling polydisperse polymerization FBRs with simultaneous particle growth and aggregation: the effect of the method of moments," *Powder Technology*, vol. 272, pp. 142-152, 2015.
- [9] V. Alopaeus, M. Laakkonen, and J. Aittamaa, "Solution of population balances with breakage and agglomeration by high-order moment-conserving method of classes," *Chemical Engineering Science*, vol. 61, pp. 6732-6752, 2006.

- [10] D. L. Marchisio, A. A. Barresi, and M. Garbero, "Nucleation, growth, and agglomeration in barium sulfate turbulent precipitation," *AIChE Journal*, vol. 48, pp. 2039-2050, 2002.
- [11] Y. Che, Z. Tian, Z. Liu, R. Zhang, Y. Gao, E. Zou, *et al.*, "A CFD-PBM model considering ethylene polymerization for the flow behaviors and particle size distribution of polyethylene in a pilot-plant fluidized bed reactor," *Powder Technology*, vol. 286, pp. 107-123, 2015.
- [12] J. Akroyd, A. J. Smith, L. R. McGlashan, and M. Kraft, "Numerical investigation of DQMoM-IEM as a turbulent reaction closure," *Chemical Engineering Science*, vol. 65, pp. 1915-1924, 2010.
- [13] Z. Li, J. Kessel, G. Grünewald, and M. Kind, "Coupled CFD-PBE simulation of nucleation in fluidized bed spray granulation," *Drying Technology*, vol. 31, pp. 1888-1896, 2013.
- [14] N. Yang and Q. Xiao, "A mesoscale approach for population balance modeling of bubble size distribution in bubble column reactors," *Chemical Engineering Science*, vol. 170, pp. 241-250, 2017.
- [15] S. Bordel, R. Mato, and S. Villaverde, "Modeling of the evolution with length of bubble size distributions in bubble columns," *Chemical Engineering Science*, vol. 61, pp. 3663-3673, 2006.
- [16] P. Chen, J. Sanyal, and M. Dudukovic, "CFD modeling of bubble columns flows: implementation of population balance," *Chemical Engineering Science*, vol. 59, pp. 5201-5207, 2004.
- [17] C. Kotoulas and C. Kiparissides, "A generalized population balance model for the prediction of particle size distribution in suspension polymerization reactors," *Chemical Engineering Science*, vol. 61, pp. 332-346, 2006.
- [18] T. Wang, J. Wang, and Y. Jin, "A CFD-PBM coupled model for gas-liquid flows," *AIChE Journal*, vol. 52, pp. 125-140, 2006.
- [19] M. Bhole, J. Joshi, and D. Ramkrishna, "CFD simulation of bubble columns incorporating population balance modeling," *Chemical Engineering Science*, vol. 63, pp. 2267-2282, 2008.
- [20] S. Tavelli, R. Rota, and M. Derudi, "A critical comparison between CFD and zone models for the consequence analysis of fires in congested environments," *Chemical Engineering Transactions*, vol. 36, 2014.
- [21] A. Delafosse, M.-L. Collignon, S. Calvo, F. Delvigne, M. Crine, P. Thonart, *et al.*, "CFD-based compartment model for description of mixing in bioreactors," *Chemical Engineering Science*, vol. 106, pp. 76-85, 2014.

- [22] P. Vrabel, R. Van der Lans, Y. Cui, and K. C. A. Luyben, "Compartment model approach: Mixing in large scale aerated reactors with multiple impellers," *Chemical Engineering Research and Design*, vol. 77, pp. 291-302, 1999.
- [23] P. Vrabel, R. G. van der Lans, F. N. van der Schot, K. C. A. Luyben, B. Xu, and S. - O. Enfors, "CMA: integration of fluid dynamics and microbial kinetics in modelling of large-scale fermentations," *Chemical Engineering Journal*, vol. 84, pp. 463-474, 2001.
- [24] J. Zahradník, R. Mann, M. Fialova, D. Vlaev, S. Vlaev, V. Lossev, *et al.*, "A networks-of-zones analysis of mixing and mass transfer in three industrial bioreactors," *Chemical Engineering Science*, vol. 56, pp. 485-492, 2001.
- [25] U. Boltersdorf, G. Deerberg, and S. Schlüter, "Computational study of the effects of process parameters on the product distribution for mixing sensitive reactions and on distribution of gas in stirred tank reactors," *Recent Research Developments in Chemical Engineering*, pp. 15-43, 2000.
- [26] A. Nørregaard, C. Bach, U. Krühne, U. Borgbjerg, and K. V. Gernaey, "Hypothesis-driven compartment model for stirred bioreactors utilizing computational fluid dynamics and multiple pH sensors," *Chemical Engineering Journal*, vol. 356, pp. 161-169, 2019.
- [27] S. Yang, S. Kiang, P. Farzan, and M. Ierapetritou, "Optimization of Reaction Selectivity Using CFD-Based Compartmental Modeling and Surrogate-Based Optimization," *Processes*, vol. 7, p. 9, 2019.
- [28] F. Bezzo, S. Macchietto, and C. Pantelides, "General hybrid multizonal/CFD approach for bioreactor modeling," *AIChE Journal*, vol. 49, pp. 2133-2148, 2003.
- [29] M. Gresch, R. Brügger, A. Meyer, and W. Gujer, "Compartmental models for continuous flow reactors derived from CFD simulations," *Environmental Science & Technology*, vol. 43, pp. 2381-2387, 2009.
- [30] W. Zhao, A. Buffo, V. Alopaeus, B. Han, and M. Louhi-Kultanen, "Application of the compartmental model to the gas-liquid precipitation of CO<sub>2</sub>-Ca(OH)<sub>2</sub> aqueous system in a stirred tank," *AIChE Journal*, vol. 63, pp. 378-386, 2017.
- [31] W. J. Huijgen, G. J. Ruijg, R. N. Comans, and G.-J. Witkamp, "Energy consumption and net CO<sub>2</sub> sequestration of aqueous mineral carbonation," *Industrial & Engineering Chemistry Research*, vol. 45, pp. 9184-9194, 2006.
- [32] S. J. Gerdemann, W. K. O'Connor, D. C. Dahlin, L. R. Penner, and H. Rush, "Ex situ aqueous mineral carbonation," *Environmental Science & Technology*, vol. 41, pp. 2587-2593, 2007.
- [33] E. H. Oelkers, S. R. Gislason, and J. Matter, "Mineral carbonation of CO<sub>2</sub>," *Elements*, vol. 4, pp. 333-337, 2008.

- [34] H.-P. Xie, L.-Z. Xie, Y.-F. Wang, J.-H. Zhu, B. Liang, and Y. Ju, "CCU: A more feasible and economic strategy than CCS for reducing CO<sub>2</sub> emissions," *Journal of Sichuan University: Engineering Science Edition*, vol. 44, pp. 1-5, 2012.
- [35] M. Kim, J. Na, S. Park, J.-H. Park, and C. Han, "Modeling and validation of a pilot-scale aqueous mineral carbonation reactor for carbon capture using computational fluid dynamics," *Chemical Engineering Science*, vol. 177, pp. 301-312, 2018.
- [36] C. Kiparissides, "Challenges in particulate polymerization reactor modeling and optimization: A population balance perspective," *Journal of Process Control*, vol. 16, pp. 205-224, 2006.
- [37] W. C. Yan, Z. H. Luo, Y. H. Lu, and X. D. Chen, "A CFD-PBM-PMLM integrated model for the gas–solid flow fields in fluidized bed polymerization reactors," *AIChE Journal*, vol. 58, pp. 1717-1732, 2012.
- [38] A. Randolph, *Theory of Particulate Processes: Analysis and Techniques of Continuous Crystallization*, Elsevier, 2012.
- [39] T. Hibiki and M. Ishii, "Interfacial area concentration of bubbly flow systems," *Chemical Engineering Science*, vol. 57, pp. 3967-3977, 2002.
- [40] A. Lozhechnikova, "Determination of slurry's viscosity using case based reasoning approach," M.S. dissertation, Department of Chemical and Process Engineering, Lappeenranta University of Technology, 2011.
- [41] C. Estrela, C. R. d. A. Estrela, L. F. Guimarães, R. S. Silva, and J. D. Pécora, "Surface tension of calcium hydroxide associated with different substances," *Journal of Applied Oral Science*, vol. 13, pp. 152-156, 2005.
- [42] K. Koide, S. Morooka, K. Ueyama, A. Matsuura, F. Yamashita, S. Iwamoto, *et al.*, "Behavior of bubbles in large scale bubble column," *Journal of Chemical Engineering of Japan*, vol. 12, pp. 98-104, 1979.
- [43] K. Akita and F. Yoshida, "Bubble size, interfacial area, and liquid-phase mass transfer coefficient in bubble columns," *Industrial & Engineering Chemistry Process Design and Development*, vol. 13, pp. 84-91, 1974.
- [44] D. Ying, E. Givens, and R. Weimer, "Gas holdup in gas-liquid and gas-liquid-solid flow reactors," *Industrial & Engineering Chemistry Process Design and Development*, vol. 19, pp. 635-638, 1980.
- [45] V. Juvekar and M. Sharma, "Absorption of CO<sub>2</sub> in a suspension of lime," *Chemical Engineering Science*, vol. 28, pp. 825-837, 1973.
- [46] N. G. Deen, T. Solberg, and B. H. Hjertager, "Large eddy simulation of the gas–liquid flow in a square cross-sectioned bubble column," *Chemical Engineering Science*, vol. 56, pp. 6341-6349, 2001.

- [47] D. Zhang, N. Deen, and J. Kuipers, "Numerical modeling of hydrodynamics, mass transfer and chemical reaction in bubble Columns," in *6th International Conference on Multiphase Flow*, ICMF 2007, 2007.
- [48] G. Kocamustafaogullari and M. Ishii, "Foundation of the interfacial area transport equation and its closure relations," *International Journal of Heat and Mass Transfer*, vol. 38, pp. 481-493, 1995.
- [49] Q. Wu, S. Kim, M. Ishii, and S. Beus, "One-group interfacial area transport in vertical bubbly flow," *International Journal of Heat and Mass Transfer*, vol. 41, pp. 1103-1112, 1998.
- [50] T. Hibiki and M. Ishii, "One-group interfacial area transport of bubbly flows in vertical round tubes," *International Journal of Heat and Mass Transfer*, vol. 43, pp. 2711-2726, 2000.
- [51] H. Brauer, "Particle/fluid transport processes," *Progress Chemical Engineering*, vol. 19, pp. 61-99, 1981.
- [52] G. Ratcliff and J. Holdcroft, "Diffusivities of gases in aqueous electrolyte solutions," *Transactions of the Institution of Chemical Engineers*, vol. 41, pp. 315-319, 1963.
- [53] G. F. Versteeg and W. Van Swaalj, "Solubility and diffusivity of acid gases (carbon dioxide, nitrous oxide) in aqueous alkanolamine solutions," *Journal of Chemical and Engineering Data*, vol. 33, pp. 29-34, 1988.
- [54] S. Weisenberger and A. Schumpe, "Estimation of gas solubilities in salt solutions at temperatures from 273 K to 363 K," *AIChE Journal*, vol. 42, pp. 298-300, 1996.
- [55] K. R. Westerterp, W. Van Swaaij, and A. Beenackers, *Chemical Reactor Design and Operation*, Wiley, 1987.
- [56] R. Pohorecki and W. Moniuk, "Kinetics of reaction between carbon dioxide and hydroxyl ions in aqueous electrolyte solutions," *Chemical Engineering Science*, vol. 43, pp. 1677-1684, 1988.
- [57] H. Hikita, S. Asai, K. Tanigawa, K. Segawa, and M. Kitao, "Gas hold-up in bubble columns," *The Chemical Engineering Journal*, vol. 20, pp. 59-67, 1980.
- [58] H. Kataoka, H. Takeuchi, K. Nakao, H. Yagi, T. Tadaki, T. Otake, *et al.*, "Mass transfer in a large bubble column," *Journal of Chemical Engineering of Japan*, vol. 12, pp. 105-110, 1979.
- [59] K. Akita and F. Yoshida, "Gas holdup and volumetric mass transfer coefficient in bubble columns. Effects of liquid properties," *Industrial & Engineering Chemistry Process Design and Development*, vol. 12, pp. 76-80, 1973.

- [60] E. Sada, H. Kumazawa, and C. Lee, "Chemical absorption in a bubble column loading concentrated slurry," *Chemical Engineering Science*, vol. 38, pp. 2047-2051, 1983.
- [61] M. Kim, S. Park, D. Lee, S. Lim, M. Park, and J. M. Lee, "Modeling long-time behaviors of industrial multiphase reactors for CO<sub>2</sub> capture using CFD-based compartmental model," *Chemical Engineering Journal*, p. 125034, 2020.
- [62] K. Koide, A. Takazawa, M. Komura, and H. Matsunaga, "Gas holdup and volumetric liquid-phase mass transfer coefficient in solid-suspended bubble columns," *Journal of Chemical Engineering of Japan*, vol. 17, pp. 459-466, 1984.
- [63] F. Bezzo and S. Macchietto, "A general methodology for hybrid multizonal/CFD models: Part II. Automatic zoning," *Computers & Chemical Engineering*, vol. 28, pp. 513-525, 2004.
- [64] A. Delafosse, F. Delvigne, M.-L. Collignon, M. Crine, P. Thonart, and D. Toye, "Development of a compartment model based on CFD simulations for description of mixing in bioreactors," *Biotechnology, Agronomy, Society, and Environment*, vol. 14, pp. 517-522, 2010.
- [65] H. Hatzantonis, A. Goulas, and C. Kiparissides, "A comprehensive model for the prediction of particle-size distribution in catalyzed olefin polymerization fluidized-bed reactors," *Chemical Engineering Science*, vol. 53, pp. 3251-3267, 1998.
- [66] D. L. Marchisio, R. D. Vigil, and R. O. Fox, "Implementation of the quadrature method of moments in CFD codes for aggregation-breakage problems," *Chemical Engineering Science*, vol. 58, pp. 3337-3351, 2003.
- [67] R. G. Gordon, "Error bounds in equilibrium statistical mechanics," *Journal of Mathematical Physics*, vol. 9, pp. 655-663, 1968.
- [68] L. Metzger and M. Kind, "The influence of mixing on fast precipitation processes—A coupled 3D CFD-PBE approach using the direct quadrature method of moments (DQMOM)," *Chemical Engineering Science*, vol. 169, pp. 284-298, 2017.
- [69] A. Shamiri, M. A. Hussain, F. S. Mjalli, and N. Mostoufi, "Kinetic modeling of propylene homopolymerization in a gas-phase fluidized-bed reactor," *Chemical Engineering Journal*, vol. 161, pp. 240-249, 2010.
- [70] R. Fan, "Computational fluid dynamics simulation of fluidized bed polymerization reactors," Ph.D. dissertation, Department of Chemical Engineering, Iowa State University, 2006.
- [71] T. J. Niemi, "Particle size distribution in CFD simulation of gas-particle flows," M.S. dissertation, School of Science, Aalto University, 2012.

- [72] C. Chen, Q. Dai, and H. Qi, "Improvement of EMMS drag model for heterogeneous gas–solid flows based on cluster modeling," *Chemical Engineering Science*, vol. 141, pp. 8-16, 2016.
- [73] H. Qi, F. Li, B. Xi, and C. You, "Modeling of drag with the Eulerian approach and EMMS theory for heterogeneous dense gas–solid two-phase flow," *Chemical Engineering Science*, vol. 62, pp. 1670-1681, 2007.
- [74] Q. Zhou and J. Wang, "CFD study of mixing and segregation in CFB risers: extension of EMMS drag model to binary gas–solid flow," *Chemical Engineering Science*, vol. 122, pp. 637-651, 2015.
- [75] F. Vejahati, N. Mahinpey, N. Ellis, and M. B. Nikoo, "CFD simulation of gas–solid bubbling fluidized bed: a new method for adjusting drag law," *The Canadian Journal of Chemical Engineering*, vol. 87, pp. 19-30, 2009.
- [76] E. Esmaili and N. Mahinpey, "Adjustment of drag coefficient correlations in three dimensional CFD simulation of gas–solid bubbling fluidized bed," *Advances in Engineering Software*, vol. 42, pp. 375-386, 2011.
- [77] E. Ghadirian and H. Arastoopour, "CFD simulation of a fluidized bed using the EMMS approach for the gas-solid drag force," *Powder Technology*, vol. 288, pp. 35-44, 2016.
- [78] M. Kim, K. Lee, Y. Bak, and J. M. Lee, "Two-way coupled CFD-DQMOM approach for long-term dynamic simulation of fluidized bed reactor," *Korean Journal of Chemical Engineering*, submitted.

## Nomenclature

### Abbreviations

CCUS: carbon capture, utilization, and storage

CFD: computational fluid dynamics

FBR: fluidized bed reactor

PBM: population balance model

E-E: Eulerian-Eulerian

NDF: number density function

MRF: multiple reference frame

PBM: population balance model

QMOM: quadrature method of moments

DQMOM: direct quadrature method of moments

CFD-hydrodynamics model: simulate only the hydrodynamics without reactions

CFD-absorption model: simulate not only hydrodynamics but also CO<sub>2</sub> absorption to the solution

CFD-QMOM: simulate flows and PBM altogether in FLUENT's own implementation code

### CHAPTER 2 & 3

a: interfacial area, m<sup>2</sup>/m<sup>3</sup>

D: column diameter, m

d<sub>b</sub>: bubble diameter, m

g: gravitational acceleration,  $\text{m/s}^2$   
k: turbulent kinetic energy,  $\text{m}^2/\text{s}^2$   
n: bubble number density  
R: ideal gas constant  
t: time, s  
T: Temperature, K  
**u**: velocity vector, m/s  
 $U_g$ : superficial gas velocity, m/s  
 $v_p$ : average bubble velocity weighted by the bubble number, m/s  
 $v_i$ : interfacial velocity, m/s  
z: axial position along the flow direction (z-direction)

### **Greek letters**

$\epsilon$ : energy dissipation,  $\text{m}^2/\text{s}^3$   
 $\alpha$ : phase volume fraction  
 $\mu$ : molecular dynamic viscosity, Pa s  
 $\mu_t$ : turbulence dynamic viscosity, Pa s  
 $\nu_m$ : solution kinematic viscosity,  $\text{m}^2/\text{s}$   
 $\rho$ : density,  $\text{kg/m}^3$   
 $\sigma$ : surface tension, N/m  
 $\phi$ : solid weight fraction in solution  
 $c_w$ : solid concentration by weight percent.  
 $\psi$ : factor depending on the shape of the bubbles

### **Subscripts and superscripts**

g: gas

l: liquid  
s: solid  
m: mixture of liquid and solid

#### **CHAPTER 4**

$d_s$ : particle size, m  
 $d_{32}$ : Sauter mean diameter, mm  
g: gravitational acceleration,  $m/s^2$   
 $K_{gs}$ : gas/solid drag coefficient  
L: particle size as internal coordinate, m  
m: moments  
n: bubble number density  
P: pressure,  $N/m^2$   
 $s_p$ : phase p among particle  
t: time, s  
 $\mathbf{u}$ : velocity vector, m/s  
w: quadrature weight

#### **Greek letters**

$\alpha$ : phase volume fraction  
 $\delta$ : Dirac delta function  
 $\mu$ : molecular dynamic viscosity, Pa s  
 $\lambda_s$ : solid bulk viscosity, Pa s  
 $\rho$ : density,  $kg/m^3$   
 $\theta_s$ : granular temperature,  $m^2/s^2$

$k_{\theta_s}$ : granular energy

$\gamma_{\theta_s}$ : collisional dissipation of energy

$\varphi_{gs}$ : energy exchange between the gas and solid

$e_{ss}$ : restitution coefficient

$g_{0,ss}$ : radial distribution function

$\tau$ : stress-strain tensor, Pa

### **Subscripts and superscripts**

g: gas

s: solid

i: specified number of moments

## Abstract in Korean (국문초록)

복잡한 유동을 갖는 다상 반응기에 대한 연구를 진행하기 위해, 전산유체역학 (CFD) 이 널리 이용되고 있다. 그러나, CFD의 경우 전산량이 매우 크기 때문에 대부분의 연구가 실험실 규모의 반응기를 초단위로 모사하는데 그치고 있다. 따라서 본 연구에서는 이러한 CFD을 이용한 다상 반응기 연구의 한계를 극복하고자 산업용 규모 다상 반응기를 장시간 모사하기 위한 방법론들을 개발하였다.

첫번째로, 산업용 규모 다상 반응기를 모사하기 위해 CFD를 널리 이용되는 상관관계식과 결합하는 방법론을 개발하였다. 기체-액체 반응기에서 기체가 서로 뭉치거나 쪼개지거나 하는 물리적인 현상을 모사하기 위해 입자수지식 (population balance equation) 을 CFD에 도입할 경우 전산시간이 매우 길어지고 커널상수 값들이 명확하지 않아 모사하기 어렵다. 따라서, CFD를 널리 이용되는 상관관계식과 결합을 하여 적은 전산량으로 물리적 현상을 고려하였고, CFD 모델과 실험결과와의 비교를 통해 이 방법론에 대한 검증을

완료하였다.

두번째로, 산업용 규모 다상 반응기를 초단위가 아닌 시간단위로 장시간 모사하기 위한 방법론을 개발하였다. 수 백 만개의 격자에서는 15-30초 정도의 유동만을 계산하고, 앞서 구해진 유동 정보를 이용하여 수 백 개의 구역에서 시간 단위의 반응을 계산하는 전산유체역학 기반 구획 모델 (CFD-based compartmental model)을 이용하였다. 최종적으로 산업용 규모 다상 반응기에 대한 전산유체역학 기반 구획 모델을 이용하여 10시간 이상 모사를 진행하였고, 실험결과와의 비교를 통해 검증을 완료하였다.

마지막으로, 전산유체역학 기반 구획 모델의 한계를 극복하기 위한 CFD-DQMOM 양방향 결합 접근법 (two-way coupled CFD-DQMOM approach) 을 개발하였다. CFD로부터 얻어진 초기 유동정보만을 이용하여 장시간 모사를 진행하는 전산유체역학 기반 구획 모델의 경우 반응이나 여러가지 물리적 현상에 의해 유동이 크게 변하는 경우에는 이용할 수 없다. 따라서 이러한 전산유체역학 기반 구획 모델의 한계를 극복하고자 주기적으로 유동 정보를 갱신해주는 CFD-

DQMOM 양방향 결합 접근법을 개발하였고, 이를 시간에 따라 유동이 변하는 유동층 반응기에 적용하였다. 이 접근법을 이용한 경우 CFD만을 이용할 경우 얻을 수 없는 장시간에 걸친 입자분포도 변화를 얻을 수 있었다.

**주요어** : 산업용 반응기; 전산유체역학; 장시간 모사; 입자수지식; CFD 기반 구획 모델; CFD-DQMOM 양방향 결합 접근법

**학번** : 2015-21044

## APPENDIX:CFD-based compartmental model code

### Code for finding neighbor zone in PYTHON

```
import re

import numpy as np

#open region file

ccl_file_location = "20180625_10ton_4m"

f=open("C:/Users/win/Desktop/CM_textfile/"+c
cl_file_location+'.ccl','r')

lines=f.readlines()

f.close()

#read the line which involve the information
of surface and body

body_line=lines[22]

surface_line=lines[17]
```

```

#Make body array from ccl file information

body_line1=body_line.split(",")

for i in range(len(body_line1)):

    body_line1[i]=body_line1[i][1:]

a=body_line1[0].index("B")

body_line1[0]=body_line1[0][a:]

body_line1[-1]=body_line1[-1][0:5]

for i in range(len(body_line1)):

    body_line1[i]=body_line1[i][1:]

#Make surface array from ccl file information

surface_line1=surface_line.split(", ")

```

```

#for i in range(len(surface_line1)):

#    surface_line1[i]=surface_line1[i][1:]

b=surface_line1[0].index("F")

surface_line1[0]=surface_line1[0][b:]

surface_line1[-1]=surface_line1[-1][0:-1]

#Split F123.456 to F123 & 456

split_surface=[];

for i in range(len(surface_line1)):

split_surface.append(surface_line1[i].split(".

"))

#Make array for just F123

front_surface_name=[]

rear_surface_name=[]

for i in range(len(surface_line1)):

```

```

front_surface_name.append(split_surface[i][0])

rear_surface_name.append(split_surface[i][1])

#Find the interface which have two surface
surface=[];

surface_body_index=[];

etc_surface=[];

for i in range(len(surface_line1)):

ii=front_surface_name.count(front_surface_name
[i])

    if ii==2:

        surface.append(surface_line1[i])

surface_body_index.append(split_surface[i][1])

    else:

        etc_surface.append(surface_line1[i])

```

```

#new Split F123.456 to F123 & 456

new_split_surface=[];

for i in range(len(surface)):

new_split_surface.append(surface[i].split("."))

#Make new array for just F123

new_front_surface_name=[]

new_rear_surface_name=[]

for i in range(len(surface)):

new_front_surface_name.append(new_split_surfac
e[i][0])

new_rear_surface_name.append(new_split_surface
[i][1])

```

```

#Make a surface matrix which consist of
interface

total_interface=int(len(surface_body_index)/
2)

surface_combin=[];

for i in range(total_interface):

ii=[surface_body_index[2*i],surface_body_index
[2*i+1]];

        surface_combin.append(ii)

#Reconstruct the surface name

new_surface_name=[];

for i in range(len(surface_combin)):

new_surface_name.append("F"+surface_combin[i][
0]+". "+surface_combin[i][1])

```

```
f=open('C:/Users/win/Desktop/CM_textfile/'+c
cl_file_location+'/front_surface_data.txt','w')

f.writelines('\n'.join(new_front_surface_nam
e))

f.close()
```

```
f=open('C:/Users/win/Desktop/CM_textfile/'+c
cl_file_location+'/front_surface_data.txt','r')

all_surface=f.read()

f.close()
```

```
f=open('C:/Users/win/Desktop/CM_textfile/'+c
cl_file_location+'/rear_surface_data.txt','w')

f.writelines('\n'.join(new_rear_surface_name
))

f.close()
```

```
f=open('C:/Users/win/Desktop/CM_textfile/'+c
cl_file_location+'/rear_surface_data.txt','r')

all_surface=f.read()

f.close()
```

```
f=open('C:/Users/win/Desktop/CM_textfile/'+c
cl_file_location+'/body_data.txt','w')

f.writelines('\n'.join(body_line1))

f.close()
```

```
f=open('C:/Users/win/Desktop/CM_textfile/'+c
cl_file_location+'/body_data.txt','r')

all_surface=f.read()

f.close()
```

```
f=open('C:/Users/win/Desktop/CM_textfile/'+c
cl_file_location+'/etc_surface_data.txt','w')

f.writelines('\n'.join(etc_surface))

f.close()
```

```
f=open('C:/Users/win/Desktop/CM_textfile/'+c
cl_file_location+'/etc_surface_data.txt','r')

all_surface=f.read()

f.close()
```

## **Code for extracting flow information from ANSYS-CFD-**

### **Post**

```
!my $pathname

="C:/Users/win/Desktop/CM_textfile/40ton_751zone/";
```

```
!my $wheretosave = "
40ton_75lzone_3.2m_1streacor_0.01s";

!chdir $pathname;

!mkdir "$wheretosave";

!chdir $pathname.$wheretosave;

!mkdir "Gas2_vf";

##C:/Users/win/Desktop/Table/

!my $file_rear_surface_path=
$pathname."rear_surface_data.txt";

!my
$file_front_surface_path=$pathname."front_surface_d
ata.txt";

!my
$file_etc_surface_path=$pathname."etc_surface_data.
txt";
```

```
!open(my $fh, '<:encoding(UTF-8)',  
$file_etc_surface_path);  
  
!my @etc_surface;  
  
!while (my $row = <$fh>) {  
  
! chomp $row;  
  
! push @etc_surface,$row;  
  
!};  
  
!open(my $fh, '<:encoding(UTF-8)',  
$file_rear_surface_path);  
  
!my @rear_surface;  
  
!while (my $row = <$fh>) {  
  
! chomp $row;  
  
! push @rear_surface,$row;  
  
!}  
  
!close($f);
```

```

!open(my $fh, '<:encoding(UTF-8)',
$file_front_surface_path);

!my @front_surface;

!while (my $row = <$fh>) {

! chomp $row;

! push @front_surface,$row;

!}

!my @origin_interface=[];

!my @interface=[];

!my @flowrate;

!foreach my $i (0..$#front_surface){

! if ($i %
2==0){$origin_interface[$i]=$front_surface[$i].".".
$rear_surface[$i],

!

$interface[$i]="F".$rear_surface[$i].".$rear_surf
ace[$i+1],"\n"}

```

```

!
else{$origin_interface[$i]=$front_surface[$i].".$rear_surface[$i],

!
$interface[$i]="F".$rear_surface[$i].".$rear_surface[$i-1],"\n"}

!});

!my $file_body_path=$pathname."body_data.txt";

!open(my $fh, '<:encoding(UTF-8)',
$file_body_path);

!my @body;

!while (my $row = <$fh>) {

! chomp $row;

! push @body,$row;

!});

!my @surface_name;

!foreach my $i (0..$#body) {

```

```

! foreach my $j (0..$#body) {

!$surface_name[$i][$j]=
"F".$body[$i].".$body[$j],"\n";}

!};

!use List::Util qw(first);

!my $total=0;

!my @idx;

!foreach $i (0..$#body) {

! foreach my $j (0..$#body) {

!if($surface_name[$i][$j]~~@interface){$idx[$i][$
j] = first { $interface[$_] eq
$surface_name[$i][$j] }
0..$#interface,$total=$total+1;}

!}

!};

!my @flowrate_table;

!foreach $i (0..$#body) {

```

```

! foreach my $j (0..$#body){

! if($surface_name[$i][$j]~~@interface){

! $flowrate_table[$i][$j]='sum(Gas2.Mass
Flow)@'. $origin_interface[$idx[$i][$j]] ,print
$flowrate_table[$i][$j],"\n";

!} else {$flowrate_table[$i][$j]='none'

!}

!}

!};

!my
$file_origin_unique_surface_path=$pathname."origin_
unique_surface.txt";

!my
$file_num_occur_path=$pathname."num_occur.txt";

!my
$file_no_unique_body_index_path=$pathname."no_uniqu
e_body_index.txt";

```

```

!open(my $fh, '<:encoding(UTF-8)',
$file_origin_unique_surface_path);

!my @origin_unique_surface;

!while (my $row = <$fh>) {

! chomp $row;

! push @origin_unique_surface,$row;

!};

!open(my $fh, '<:encoding(UTF-8)',
$file_num_occur_path);

!my @num_occur;

!while (my $row = <$fh>) {

! chomp $row;

! push @num_occur,$row;

!};

!open(my $fh, '<:encoding(UTF-8)',
$file_no_unique_body_index_path);

!my @no_unique_body_index;

!while (my $row = <$fh>) {

! chomp $row;

! push @no_unique_body_index,$row;

```

```

!});

!my $accum_occur=0;

!foreach $i (0..$#num_occur+1){
!
$flowrate_table[$no_unique_body_index[2*$i]][$no_un
ique_body_index[2*$i+1]]="",
!
$flowrate_table[$no_unique_body_index[2*$i+1]][$no_
unique_body_index[2*$i]]="";
! foreach $j (0..$num_occur[$i]-1){
! if
($j==0){$flowrate_table[$no_unique_body_index[2*$i]
] [$no_unique_body_index[2*$i+1]]='sum(Gas2.Mass
Flow)@'. $origin_unique_surface[2*$accum_occur+2*$j]
,
!
$flowrate_table[$no_unique_body_index[2*$i+1]][$no_
unique_body_index[2*$i]]='sum(Gas2.Mass

```

```

Flow)@'.$origin_unique_surface[2*$accum_occur+2*$j+
1];

!} else {

!

$flowrate_table[$no_unique_body_index[2*$i]][$no_un
ique_body_index[2*$i+1]]=$flowrate_table[$no_unique
_body_index[2*$i]][$no_unique_body_index[2*$i+1]].'
+'.'sum(Gas2.Mass
Flow)@'.$origin_unique_surface[2*$accum_occur+2*$j]
,

!

$flowrate_table[$no_unique_body_index[2*$i+1]][$no_
unique_body_index[2*$i]]=$flowrate_table[$no_unique
_body_index[2*$i+1]][$no_unique_body_index[2*$i]].'
+'.'sum(Gas2.Mass
Flow)@'.$origin_unique_surface[2*$accum_occur+2*$j+
1];

! }

! } $accum_occur=$accum_occur+$num_occur[$i],
print
$flowrate_table[$no_unique_body_index[2*$i+1]][$no_

```

```

unique_body_index[2*$i]], "\n", print
$flowrate_table[$no_unique_body_index[2*$i]][$no_un
ique_body_index[2*$i+1]], "\n";
    !});

!my @etc_mf ;

!foreach my $i (0..$#etc_surface){

!$etc_mf[$i]='sum(Gas2.Mass
Flow)@'.$etc_surface[$i];

!});

!my @etc_sign ;

!foreach my $i (0..$#etc_surface){

!$etc_sign[$i]='massFlow()@'.$etc_surface[$i];

!});

!my @volume ;

```

```

!my @Gasholdup;

!my @Gas_vu;

!my @Gas_vv;

!my @Gas_vw;

!my @water_vu;

!my @water_vv;

!my @water_vw;

!foreach $i (0..$#body) {

!$volume[$i]='volume()@'.'B'.$body[$i],

!$Gasholdup[$i]='volumeAve(Gas.vf)@B'.$body[$i],

!$Gas2holdup[$i]='volumeAve(Gas2.vf)@B'.$body[$i]

,

!$Gas_vu[$i]='volumeAve(Gas2.Velocity
u)@B'.$body[$i],

!$Gas_vv[$i]='volumeAve(Gas2.Velocity
v)@B'.$body[$i],

```

```

!$Gas_vw[$i]='volumeAve(Gas2.Velocity
w)@B'.$body[$i],

!$water_vu[$i]='volumeAve(water.Velocity
u)@B'.$body[$i],

!$water_vv[$i]='volumeAve(water.Velocity
v)@B'.$body[$i],

!$water_vw[$i]='volumeAve(water.Velocity
w)@B'.$body[$i];

!}

!foreach my $i (0..$#body){

TABLE: Table 2

Table Exists = True

TABLE CELLS:

A.$i = "=$volume[$i]", False, False, False, Left,
True, 0, Font Name, 1|1, %10.5e, False, fffffff,
00000000, True

```

B.\$i = "=\$Gasholdup[\$i]", False, False, False,  
Left, True, 0, Font Name, 1|1, %10.5e, False,  
ffffff, 00000000, True

C.\$i = "=\$Gas2holdup[\$i]", False, False, False,  
Left, True, 0, Font Name, 1|1, %10.5e, False,  
ffffff, 00000000, True

D.\$i = "=\$Gas\_vu[\$i]", False, False, False, Left,  
True, 0, Font Name, 1|1, %10.5e, False, ffffff,  
00000000, True

E.\$i = "=\$Gas\_vv[\$i]", False, False, False, Left,  
True, 0, Font Name, 1|1, %10.5e, False, ffffff,  
00000000, True

F.\$i = "=\$Gas\_vw[\$i]", False, False, False, Left,  
True, 0, Font Name, 1|1, %10.5e, False, ffffff,  
00000000, True

G.\$i = "=\$water\_vu[\$i]", False, False, False,  
Left, True, 0, Font Name, 1|1, %10.5e, False,  
ffffff, 00000000, True

```
H.$i = "=$water_vv[$i]", False, False, False,  
Left, True, 0, Font Name, 1|1, %10.5e, False,  
ffffff, 00000000, True
```

```
I.$i = "=$water_vw[$i]", False, False, False,  
Left, True, 0, Font Name, 1|1, %10.5e, False,  
ffffff, 00000000, True
```

```
END
```

```
END
```

```
!});
```

```
!my $num=$#body +1;
```

```
!my $tablename ="Table.".$num;
```

```
TABLE:Table 2
```

```
Export Table Only = True
```

```
Table Export HTML Title =
```

```
Table Export HTML Caption Position = Bottom
```

```
Table Export HTML Caption =
```

```
Table Export HTML Border Width = 1
```

```

Table Export HTML Cell Padding = 5

Table Export HTML Cell Spacing = 1

Table Export Lines = All

Table Export Trailing Separators = True

Table Export Separator = Tab

END

>table

save=C:/Users/win/Desktop/Table/$wheretosave/$table
name.csv, name=Table 2

> delete /TABLE:Table 2

! foreach my $i (0..$#body){

!my $coun =0;

! foreach my $j (0..$#body){

!if ($flowrate_table[$i][$j]ne'none'){

!my $newj=$j+1;

```

TABLE: Table 1

Table Exists = True

TABLE CELLS:

A.1= "=0", False, False, False, Left, True, 0,  
Font Name, 1|1, %10.5e, False, fffffff, 00000000,  
True

A.\$newj = "=\$flowrate\_table[\$i][\$j]", False,  
False, False, Left, True, 0, Font Name,  
1|1, %10.5e, False, fffffff, 00000000, True

END

END

!});

!});

!my \$count = \$#body;

!foreach my \$h (0..\$#etc\_surface){

!my @aaa=split/\./,\$etc\_surface[\$h];

!if(\$aaa[1] eq \$body[\$i]){

! \$count +=2; ## because \$#body is 611 not 612,  
so in order to express (the number of body +1) we  
should + 2

TABLE: Table 1

Table Exists = True

TABLE CELLS:

A.\$count = "=if(\$etc\_sign[\$h]==0[kg s^-1],0[kg  
s^-1],\$etc\_mf[\$h])", False, False, False, Left,  
True, 0, Font Name, 1|1, %10.5e, False, fffffff,  
00000000, True

END

END

!});

!});

!my \$tablename ="Table";

TABLE:Table 1

Export Table Only = True

```
Table Export HTML Title =

Table Export HTML Caption Position = Bottom

Table Export HTML Caption =

Table Export HTML Border Width = 1

Table Export HTML Cell Padding = 5

Table Export HTML Cell Spacing = 1

Table Export Lines = All

Table Export Trailing Separators = True

Table Export Separator = Tab

END

>table
save=C:/Users/win/Desktop/Table/$wheretosave/$table
name.$i.csv, name=Table 1

> delete /TABLE:Table 1

!};
```